

An assessment of global and regional sea level for years 1993-2007 in a suite of interannual CORE-II simulations

Stephen M. Griffies^{1,*}, Jianjun Yin^b, Paul J. Durack^c, Paul Goddard^b, Susan C. Bates^d, Erik Behrens^e, Mats Bentsen^f, Daohua Bi^g, Arne Biastoch^e, Claus W. Böning^e, Alexandra Bozec^h, Eric Chassignet^h, Gokhan Danabasoglu^d, Sergey Danilovⁱ, Catia Domingues^j, Helge Drange^k, Riccardo Farneti^l, Elodie Fernandez^m, Richard J. Greatbatch^e, David M. Hollandⁿ, Mehmet Ilıcak^f, William G. Large^d, Katja Lorzbacher^g, Jianhua Lu^h, Simon J. Marsland^g, Akhilesh Mishra^h, A. J. George Nurser^o, David Salas y Méliá^p, Jaime B. Palter^d, Bonita L. Samuels^a, Jens Schröterⁱ, Franziska U. Schwarzkopf^e, Dmitry Sidorenkoⁱ, Anne Marie Treguier^r, Yu-heng Tseng^d, Hiroyuki Tsujino^s, Petteri Uotila^g, Sophie Valcke^m, Aurore Voldoire^p, Qiang Wangⁱ, Michael Winton^a, Xuebin Zhang^t

^aNOAA Geophysical Fluid Dynamics Laboratory, Princeton, USA

^bDepartment of Geosciences, University of Arizona, Tucson USA

^cProgram for Climate Model Diagnosis and Intercomparison, Lawrence Livermore National Laboratory, USA

^dNational Center for Atmospheric Research, Boulder USA

^eGEOMAR Helmholtz Centre for Ocean Research Kiel, Kiel, Germany

^fUni Climate, Uni Research Ltd., Bergen, Norway

^gCentre for Australian Weather and Climate Research, a partnership between CSIRO and the Bureau of Meteorology, Commonwealth Scientific and Industrial Research Organisation (CSIRO), Melbourne, Australia

^hCenter for Ocean-Atmospheric Prediction Studies (COAPS), Florida State University, Tallahassee, FL, USA

ⁱAlfred Wegener Institute (AWI) for Polar and Marine Research, Bremerhaven, Germany

^jAntarctic Climate and Ecosystems Cooperative Research Centre, University of Tasmania, Hobart, AUS

^kUniversity of Bergen, Bergen, Norway

^lInternational Centre for Theoretical Physics (ICTP), Trieste, Italy

^mCentre Européen de Recherche et de Formation Avancé en Calcul Scientifique (CERFACS), URA 1875, CNRS/INSU, Toulouse, France

ⁿNew York University, New York 10012, USA

^oNational Oceanography Centre Southampton (NOCS), Southampton, UK

^pCentre National de Recherches Météorologiques (CNRM), Toulouse, France

^qMcGill University, Montreal, Canada

^rLaboratoire de Physique des Océans, UMR 6523, CNRS-Ifremer-IRD-UBO, Plouzane, France

^sMeteorological Research Institute (MRI), Japan Meteorological Agency, Tsukuba, Japan

^tCentre for Australian Weather and Climate Research, a partnership between CSIRO and the Bureau of Meteorology, Commonwealth Scientific and Industrial Research Organisation (CSIRO), Hobart, Australia

Abstract

We provide an assessment of sea level simulated in a suite of global ocean-sea ice models using the interannual CORE atmospheric state to determine surface ocean boundary buoyancy and momentum fluxes. These CORE-II simulations are compared amongst themselves as well as to observation-based estimates. We focus on the final 15 years of the simulations (1993-2007), as this is a period where the CORE-II atmospheric state is well sampled, and it allows us to compare sea level related fields to both satellite and *in situ* analyses. The ensemble mean of the CORE-II simulations broadly agree with various global and regional observation-based

analyses during this period, though with the global mean thermosteric sea level rise biased low relative to observation-based analyses. The simulations reveal a positive trend in dynamic sea level in the west Pacific and negative trend in the east, with this trend arising from wind shifts and regional changes in upper 700 m ocean heat content. The models also exhibit a thermosteric sea level rise in the subpolar North Atlantic associated with a transition around 1995/1996 of the North Atlantic Oscillation to its negative phase, and the advection of warm subtropical waters into the subpolar gyre. Sea level trends are predominantly associated with steric trends, with thermosteric effects generally far larger than halosteric effects, except in the Arctic and North Atlantic. There is a general anti-correlation between thermosteric and halosteric effects for much of the World Ocean, associated with density compensated changes.

1. Introduction

There are growing observation-based measures of large-scale patterns of sea level variations with the advent of the Argo floats (since the early 2000s) and satellite altimeters (since 1993). Such measures provide a valuable means to evaluate aspects of global model simulations, such as the global ocean-sea ice simulations run as part of the interannual Coordinated Ocean-sea ice Reference Experiments (Griffies et al., 2009b; Danabasoglu et al., 2014). In this paper, we present an assessment of such CORE-II simulations from 13 model configurations, with a focus on their ability to capture observation-based trends in ocean heat content as well as steric, thermosteric and halosteric sea level.

Our assessment focuses on the final 15 year period (1993-2007) of the CORE-II simulations to enable direct comparison of the simulations to both *in situ* and satellite based analyses. During this relatively short period, sea level variations have a large component due to natural variability (Zhang and Church, 2012; Meyssignac et al., 2012). This situation is compatible with the CORE-II simulations, as they are primarily designed for studies of interannual variability (Doney et al., 2007; Large and Yeager, 2012). Focusing our assessment on these years also ensures that the Large and Yeager (2009) atmospheric state, used as part of the CORE-II air-sea flux calculations, contains interannual satellite-based radiation, which is available only after 1983.

The practical basis for our study is a suite of global ocean-sea ice models forced with 60 years of the interannual CORE-II atmospheric state from Large and Yeager (2009), with this atmosphere state repeated five times for a total of 300 years. Details of the protocol can be found in Griffies et al. (2009b), which focused on the use of a repeating annual cycle; i.e., the Normal Year Forcing of the CORE-I project. Further details specific to the interannual CORE-II protocol are provided in the Atlantic study by Danabasoglu et al. (2014), with that study also providing many details of the models forming the suite of CORE-II simulations analyzed here.

*Corresponding author

Email address: Stephen.Griffies@noaa.gov (Stephen M. Griffies)

25 *1.1. Questions asked in this paper*

26 Sea level change due to human-induced climate change has the potential to affect coastal
27 regions over the remainder of the 21st century and for centuries thereafter. From among the
28 many physical processes impacting sea level, it is the evolution of land ice sheets on Greenland
29 and Antarctica that offers the greatest degree of uncertainty and broadest potential for significant
30 impact. For example, the growth and decay of ice sheets have caused sea level change on the
31 order of 100 m over the recent 450 thousand years with fluctuations of about 100 thousand years
32 (Lambeck et al., 2002; Rohling et al., 2009). We ignore here such sea level changes associated
33 with melting land ice (except to the extent that such water fluxes are contained in the CORE-
34 II river runoff data based on Dai et al. (2009)). There are complementary global ocean-sea ice
35 studies that consider the ocean's response to melt events, such as those from Gerdes et al. (2006),
36 Stammer (2008), Weijer et al. (2012) and Lorbacher et al. (2012).

37 Ocean warming causes ocean volume to increase due to a decrease in density. As estimated
38 by Church et al. (2011) and Gregory et al. (2013), such changes in global mean thermosteric
39 sea level determine about one-third to one-half of the observed global mean sea level rise during
40 the late 20th and early 21st centuries, with changes in ocean mass contributing the remainder.
41 Although limited largely to examinations of natural variability over the relatively short period
42 of 1993-2007, our assessment is of some use to determine the suitability of global ocean-sea
43 ice models for capturing longer term observed trends largely due to anthropogenic effects, such
44 as those considered in Levitus et al. (2005), Boyer et al. (2005), Domingues et al. (2008), Ishii
45 and Kimoto (2009), Hosoda et al. (2009), Durack and Wijffels (2010), Church et al. (2011),
46 Gleckler et al. (2012), and Levitus et al. (2012). In particular, we can assess the ability of
47 forced global ocean-sea ice models to represent observed changes in patterns of ocean heat
48 content and thermosteric sea level change (Lombard et al., 2009; Kuhlbrodt and Gregory, 2012).
49 Furthermore, we note the importance of ocean warming on ice shelf melt (e.g., Yin et al., 2011),
50 with this connection providing yet another reason that an assessment of how models simulate
51 observed warming provides a useful measure of their skill for making projections.

52 The following two questions regarding the global mean sea level trends and associated spa-
53 tial patterns frame our assessment of the CORE-II simulations.

- 54 • GLOBAL MEAN THERMOSTERIC SEA LEVEL: Do CORE-II global ocean-sea ice simulations re-
55 produce the observed global mean sea level variations associated with thermosteric ef-
56 fects estimated from the observation-based analyses? To address this question, we focus
57 on ocean temperature and heat content trends, and how these trends are associated with
58 changes in thermosteric sea level.

- 59 • PATTERNS OF DYNAMIC SEA LEVEL: Do CORE-II ocean-sea ice simulations reproduce observa-
60 tion-based changes to dynamic sea level patterns? To address this question, we partition dy-
61 namic sea level trends into their halosteric and thermosteric patterns, as well as bottom
62 pressure contributions.

63 Answers to these questions are not simple, nor do we presume our contribution leads to unequiv-
64 ocal results. Nonetheless, we aim to provide physical and mathematical insight in the process
65 of assessing the physical integrity of the CORE-II simulations. An underlying hypothesis of

66 CORE is that global ocean-sea ice models coupled with the same prescribed atmospheric state
67 produce similar simulations (Griffies et al., 2009b; Danabasoglu et al., 2014). We consider this
68 hypothesis in the context of our sea level analysis. We hope that our presentation assists in the
69 ongoing scientific quest to understand observed sea level changes, and to characterize some of
70 its causes as realized in global ocean-sea ice models.

71 *1.2. Style and structure of this paper*

72 We aim to physically motivate and mathematically detail a suite of methods for sea level
73 studies, providing sufficient information to both understand and reproduce our analyses. In this
74 way, we hope that this paper serves both as a benchmark for how the present suite of CORE-II
75 simulations performs in the representation of sea level, and provides a reference from which the
76 reader may understand this, and other, studies of simulated sea level even after the models used
77 here become obsolete.

78 The remainder of this paper consists of the following sections. We initiate the main text in
79 Section 2 by considering aspects of the sea level question as framed by the CORE-II simula-
80 tions with global ocean-sea ice models. In particular, we refine the questions posed in Section
81 1.1 by exposing some of the limitations inherent in the CORE-II experimental design and the
82 atmospheric state used to drive the models. Our analysis of the global mean sea level from the
83 CORE-II simulations is then presented in Section 3. It is here that we focus on the first question
84 posed above concerning how well the CORE-II simulations represent the global thermosteric
85 rise in sea level as compared to observation-based estimates. We follow in Section 4 with a
86 discussion of the ocean heating trends over the years 1993-2007, with comparison to estimated
87 observation-based trends. In Section 5 we then present the regional patterns of sea level (second
88 question raised above), partitioning sea level trends into thermosteric, halosteric, and bottom
89 pressure trends. We complete the main text with a summary and discussion in Section 6.

90 We provide a selection of support material in the appendices. Some of this material is rudi-
91 mentary, yet it is central to the theoretical and practical foundation of this paper. Appendix A
92 focuses on the global mean sea level question as posed in ocean-sea ice climate models, which
93 can be addressed through kinematic considerations. Appendix B presents dynamical notions of
94 use to interpret patterns of sea level, in particular the partitioning of sea level tendencies into
95 thermosteric, halosteric, and bottom pressure tendencies. Appendix C examines the ability of
96 ocean models to conserve heat throughout the ocean fluid.

97 *1.3. Scope of our analysis*

98 This paper contains a wealth of information in its many multi-paneled figures. However,
99 we do not fully discuss each detail in the figures, as doing so requires a tremendous amount of
100 discussion making a long paper even longer. We suggest that many readers may find it sufficient
101 to focus on the CORE-II ensemble means that are provided for most of the figures, with our
102 discussion often focusing on the ensemble mean.

103 Furthermore, our presentation is descriptive in nature, as framed within the physically based
104 analysis methodology detailed in the appendices. There is, however, little insight offered for the
105 underlying physical mechanisms that explain model-model or model-observational differences.
106 For example, we do not try to associate a particular model behaviour with the choice of physical

107 parameterization. Such work is beyond our scope, with the present analysis intent on helping to
108 identify areas where process-based studies may be warranted to isolate mechanisms accounting
109 for differences.

110 Some readers may be disappointed with our reticence to penetrate deeper into such mech-
111 anisms. We too are disappointed. However, we are limited in how much we can answer such
112 questions based on available diagnostic output from the simulations. Nonetheless, this excuse,
113 which is in fact ubiquitous in such comparison papers utilizing CORE or CMIP (Coupled Model
114 Intercomparison Project) simulations, is unsatisfying. The logistics of coordinating a compari-
115 son become increasingly complex when aiming to compare detailed diagnostics, such as budget
116 terms, in a consistent manner. Yet more should be done to mechanistically unravel model-model
117 differences. We provide further comment in Section 6.6 regarding this point. We argue there that
118 progress on this issue is possible, with one means requiring a physical process-based analysis of
119 the heat, salt, and buoyancy budgets.

120 **2. Sea level in CORE-II simulations**

121 We frame here the sea level question for the CORE-II simulations. Of interest are salient
122 ocean model fundamentals and limitations, and aspects of the CORE-II experimental design.

123 *2.1. CORE-II simulations compared to CMIP*

124 Many sea level simulations are based on global coupled climate or earth system models,
125 such as those participating in the Coupled Model Intercomparison Project (CMIP) (Meehl et al.,
126 2007; Taylor et al., 2012). We take a different approach here by considering a suite of global
127 ocean-sea ice model configurations following the CORE-II protocol. Both CMIP and CORE-II
128 allow one to study the role of natural and anthropogenic forcing on decadal time scales, as well
129 as to consider elements of ocean and climate system predictability.

130 The interannually forced CORE-II simulations considered in this paper offer the potential
131 for a mechanistic characterization of observed ocean changes over the years 1948-2007. Dan-
132 abasoglu et al. (2014) provides an example for the North Atlantic, with further studies ongoing
133 in the community. Nonetheless, it is important to note that this potential is rarely realised unam-
134 biguously, as there are practical limitations associated with an incomplete observational record;
135 uncertainties in the prescribed atmospheric state used as part of the flux calculations, especially
136 for years prior the use of satellite radiation starting mid-1983; relative shortness of the atmo-
137 spheric state that prompts its recycling; and the inevitable biases and limitations in numerical
138 models. One further limitation concerns the CORE-II experimental design related to surface
139 boundary fluxes. Namely, CORE-II eliminates an interactive atmospheric component. Doing so
140 introduces uncertainties associated with missing or corrupted air-sea feedbacks and ambiguities
141 concerning the surface salinity boundary condition. These issues are reviewed in Griffies et al.
142 (2009b).

143 We here compare the CMIP and CORE approaches.

- 144 • **PRESCRIBED FORCING:** In the historical component of CMIP simulations, global climate
145 models are forced with solar radiation and estimates of historical atmospheric compo-
146 sition/emissions/volcanoes. Air-sea fluxes are computed based on the evolving ocean,

147 atmosphere, and sea ice states. For CORE-II, air-sea fluxes are computed based on a
148 common bulk formula and common prescribed atmospheric state, with the prescribed at-
149 mospheric state estimated from reanalysis and observation-based products as compiled by
150 Large and Yeager (2009). Only the ocean and sea ice are prognostic in CORE-II simu-
151 lations. Hence, air-sea flux differences for CORE-II models arise from differences in the
152 surface ocean and sea ice states.

153 • **UNCERTAINTIES:** For CMIP, there are uncertainties in the representation of atmospheric pro-
154 cesses associated with buoyancy and momentum fluxes across the air-sea interface. Un-
155 certainty and model spread are induced by the entire climate system (the atmosphere,
156 ocean, ice, land surface, etc.). For CORE-II, there are uncertainties in how well the pre-
157 scribed atmospheric state represents the real world. However, because the atmosphere is
158 prescribed in CORE-II, model spread is induced only by the prognostic ocean and sea ice
159 components. In principle, results from CORE-II can help interpret and attribute model
160 spread in CMIP.

161 • **DRIFT:** For CMIP, changes in sea level associated with climate change scenarios are typ-
162 ically isolated by subtracting a control simulation, thus providing a means (albeit imper-
163 fect) to remove model drift. The CORE-II simulations derive their forcing based on a
164 prescribed atmospheric state. There is no control in the sense used for CMIP. Model drift,
165 particularly associated with deep ocean temperature and salinity, is a function of how long
166 the model has been spun-up. The CORE-II protocol followed here considers five cycles of
167 60 years duration each (years 1948-2007), whereas the deep ocean takes order thousands
168 of years to equilibrate (Stouffer, 2004; Danabasoglu, 2004).

169 • **INITIAL STATES:** The centennial-scale CMIP simulations generally start with a spun-up
170 ocean state obtained by running the climate model for a time sufficient to reach quasi-
171 equilibrium, whereas the more recent CMIP5 decadal prediction experiments initialize
172 the ocean state based on observational estimates (Meehl et al., 2007; Taylor et al., 2012).
173 The CORE-II simulations are initialized from observational estimates based on poten-
174 tial temperature and salinity from the Polar Science Center Hydrographic Climatology
175 (PHC2; a blending of the Conkright et al. (2002) analysis with modifications in the Arctic
176 based on Steele et al. (2001)). Sea ice for CORE-II is generally initialized from a previous
177 simulation. Further details for the CORE-II initialization can be found in Griffies et al.
178 (2009b) and Danabasoglu et al. (2014).

179 One final point of comparison is to observe that the CMIP5 model archive contains results
180 that are written in a common format with standardized names and grid information (Griffies
181 et al., 2009a; Taylor et al., 2012). In contrast, CORE-II variable names generally differ across
182 the models, as does the grid information, and even sign conventions on the vertical direction.
183 The less strict protocol for CORE-II data submission facilitates the participation of a wider suite
184 of research groups. Unfortunately, it places a burden on the analyst who must sift through the
185 data on a model-by-model basis. We suggest that broadening the CORE project in a manner
186 reflective of CMIP must include resources to produce model output in a common format.

187 2.2. *What is “sea level” as computed by ocean models?*

188 There are many terms used in the literature for “sea level” and its variants. We define those
189 terms used in this paper, and in turn identify what is available from the CORE-II simulations.

190 2.2.1. *Sea level*

191 Sea level is the distance between the ocean bottom and the sea surface. Sea level can thus
192 change if the bottom changes due to solid earth geophysical processes, or the surface changes
193 due to modifications of ocean mass or density. There are many geophysical processes that impact
194 sea level, some involving dynamics of the liquid ocean (e.g., density and currents simulated in
195 ocean climate models), and some involving other geophysical processes such as solid earth and
196 gravitational dynamics.

197 2.2.2. *Sea surface height (SSH)*

198 The ocean-sea ice models used in this paper, as with nearly all global ocean climate models,
199 assume a fixed land-sea configuration and fixed gravitational and rotational effects. We refer to
200 the ocean surface computed by such models as the *sea surface height* (SSH) and denote it by η . In
201 principle, the SSH measures the sea surface deviation from a constant geopotential surface. Note
202 that we use the term SSH whether the model respects volume conserving Boussinesq kinematics
203 or mass conserving non-Boussinesq kinematics (see below and Section 2.5).

204 2.2.3. *Global mean sea level*

205 Global mean sea level is given by

$$\bar{\eta} = \frac{\int \eta \, dA}{\int dA}, \quad (1)$$

206 where the area integral extends over the surface of the World Ocean. Global mean sea level
207 reflects the global averaged impacts of changes to the ocean’s density structure and to its mass
208 (Appendix A2). It has been the subject of many studies, with Gregory et al. (2013) quantifying
209 how physical processes impact global mean sea level. Although no single location on the planet
210 measures global mean sea level, it remains an important field to consider in all sea level studies.

211 2.2.4. *Boussinesq fluid*

212 The Boussinesq approximation is commonly made for ocean climate models (see Table 1),
213 whereby the kinematics is approximated by those of a volume conserving fluid. The volume of
214 a Boussinesq ocean changes in the presence of precipitation, evaporation, or runoff, and remains
215 constant if the net volume of water added to the global ocean vanishes. In contrast, the mass of a
216 Boussinesq ocean generally changes even without a boundary mass flux, since density changes
217 translate into mass changes in a volume conserving fluid.

218 2.2.5. *non-Boussinesq fluid*

219 Rather than conserving volume, the ocean fluid in fact conserves mass. The kinematics of
220 a non-Boussinesq fluid respects the mass conserving nature of an ocean fluid parcel, with two

221 of the contributing CORE-II models mass conserving (see Table 1). The total mass of a non-
 222 Boussinesq ocean changes in the presence of precipitation, evaporation, or runoff, and remains
 223 constant if these fluxes have a zero net over the globe. The volume of a non-Boussinesq ocean
 224 generally changes even without a boundary volume flux, since density changes translate into
 225 volume changes in a mass conserving fluid. Consequently, the budget for total ocean volume,
 226 and hence for the global mean sea level, includes source/sink terms arising from steric effects
 227 (see Griffies and Greatbatch (2012) for much more on this point).

228 2.2.6. Steric effects

229 As seawater density changes from changes in the temperature, salinity, and pressure, so
 230 too does sea level through expansion or contraction of the ocean volume. Density induced sea
 231 level changes are referred to here as *steric effects*. We sometimes refer to the sea level changes
 232 associated with steric effects as the *steric sea level*, along with its components *thermosteric sea*
 233 *level* and *halosteric sea level*.

234 Griffies and Greatbatch (2012) in their Section 1.2 identify three distinct steric effects. We
 235 summarize here some of the salient points, which are presented in more detail in the Appendix
 236 A and B in the present paper. These points prove to be important for how we analyze sea level
 237 in the CORE simulations.

- 238 1. The *global steric* effect is given by (see equation (27) in Appendix A2)

$$\left(\frac{\partial \bar{\eta}}{\partial t}\right)^{\text{global steric}} \equiv -\frac{\mathcal{V}}{\mathcal{A}} \left(\frac{1}{\langle \rho \rangle} \frac{\partial \langle \rho \rangle}{\partial t}\right), \quad (2)$$

239 where \mathcal{V}/\mathcal{A} is the ratio of the global ocean volume to global ocean surface area; i.e., the
 240 global mean ocean depth. The global steric effect gives rise to a change in global mean
 241 sea level, $\bar{\eta}$, due to changes in global mean *in situ* density $\langle \rho \rangle$. For example, as global
 242 mean density decreases, global mean sea level rises.

- 243 2. The *local steric* effect is given by (see equation (47) in Appendix B1)

$$\left(\frac{\partial \eta}{\partial t}\right)^{\text{local steric}} = -\frac{1}{\rho_o} \int_{-H}^{\eta} \frac{\partial \rho}{\partial t} dz, \quad (3)$$

244 where the vertical integral of the local time tendency of *in situ* density extends over the
 245 full ocean column from the bottom at $z = -H(x, y)$ to surface at $z = \eta(x, y, t)$, and where ρ_o
 246 is a representative ocean density commonly used to approximate the surface density $\rho(\eta)$.
 247 The local steric effect accounts for changes in sea level arising from local time tendencies
 248 of density. We can partition sea level evolution in a hydrostatic fluid into the local steric
 249 effect plus a term arising from changes in the mass within a fluid column (Section B1). The
 250 mass term is found to be about an order of magnitude smaller in the CORE-II simulations
 251 than the local steric term (compare Figures 19 and 20).

- 252 3. The *non-Boussinesq steric* effect is given by (see equation (15) in Appendix A1)

$$\left(\frac{\partial \eta}{\partial t}\right)^{\text{non-bouss steric}} = -\int_{-H}^{\eta} \frac{1}{\rho} \frac{d\rho}{dt} dz, \quad (4)$$

253 where $d\rho/dt$ is the material or Lagrangian time derivative of *in situ* density. The non-
 254 Boussinesq steric effect is thoroughly detailed in Griffies and Greatbatch (2012), with
 255 particular focus on how physical processes (e.g., mixing, eddy transport, boundary fluxes
 256 of buoyancy, nonlinear equation of state effects) affect global mean sea level. However,
 257 the non-Boussinesq steric effect is not of direct concern in the present paper.

258 Although these three steric effects are associated with density, they generally refer to phys-
 259 ically distinct processes and thus manifest in ocean models in distinct manners. In particular,
 260 sea level in a mass conserving non-Boussinesq model is impacted by all three steric effects. In
 261 contrast, as emphasized by Greatbatch (1994), the prognostic sea level in Boussinesq fluids is
 262 not impacted by the global steric effect nor the non-Boussinesq steric effect. Additionally, due
 263 to the use of volume conserving kinematics, Boussinesq fluids alter mass, and hence bottom
 264 pressure, when density changes (Huang and Jin, 2002). To determine changes in global mean
 265 steric sea level in Boussinesq models, it is necessary to perform an *a posteriori* diagnostic cal-
 266 culation. We detail salient diagnostic methods in Appendix A3 (see also Appendix D in Griffies
 267 and Greatbatch (2012)).

268 Although the prognostic sea level in Boussinesq models is unaffected by global steric and
 269 non-Boussinesq steric effects, it is influenced by local steric effects. Hence, both Boussinesq and
 270 non-Boussinesq sea level patterns are affected by changes in ocean temperature, salinity, and
 271 pressure. For the present paper, we are concerned with global steric effects when considering
 272 global mean sea level, and local steric effects when considering patterns of sea level change.

273 2.2.7. Dynamic sea level (DSL)

274 The global spatial anomaly of SSH is referred to as the *dynamic sea level*, ζ , and is deter-
 275 mined according to

$$\zeta = \eta - \bar{\eta}. \quad (5)$$

276 DSL gradients give rise to pressure forces acting to accelerate fluid motion. SSH is identical to
 277 the DSL for the special case of a volume conserving Boussinesq model employing zero surface
 278 water fluxes (e.g., virtual salt flux models; Section 2.5). For more realistic models, such as
 279 mass conserving non-Boussinesq models, models with a mass/volume flux across the ocean
 280 surface, and/or models impacted by changes in the atmospheric loading, the SSH also includes
 281 an evolving global mean component, in which case ζ and η differ.

282 Horizontal patterns of dynamic sea level reflect nearly all of the many physical oceanog-
 283 raphic processes active in the ocean, from the bottom to the surface. We may compute such
 284 patterns using either a mass conserving non-Boussinesq ocean model, or volume conserving
 285 Boussinesq model, with negligible difference seen at the large scales of concern here (e.g.,
 286 see Figure 3 in Griffies and Greatbatch (2012)). In particular, regional impacts of local steric
 287 changes are included in both Boussinesq and non-Boussinesq models (see Appendix B).

288 2.2.8. Sea level under sea ice

289 The upper ocean surface responds to the pressure loading from sea ice, p_{ice} , in an inverse
 290 barometer manner (see Appendix C to Griffies and Greatbatch (2012)). Some models in this
 291 study (e.g., GFDL-MOM, GFDL-GOLD) depress their ocean model free surface under sea ice,
 292 whereas others do not and so in effect levitate their sea ice. We measure the effective sea level

293 defined according to the free surface plus any applied loading from ice (see equation (206) in
294 Griffies and Greatbatch (2012))

$$\eta^{\text{effective}} = \eta + \frac{P_{\text{ice}}}{g\rho_o}, \quad (6)$$

295 where g is the gravitational acceleration and $\rho_o = 1035 \text{ kg m}^{-3}$ is a representative ocean density.
296 This is the sea level relevant for climate impacts, as, for example, considered by Kopp et al.
297 (2010) and Yin et al. (2010a).

298 2.2.9. *Static equilibrium sea level*

299 In the absence of ocean currents, a resting sea level coincides with a level of constant geopo-
300 tential, which defines the static equilibrium sea level. Changes in the mass field of the earth,
301 including changes in the ocean mass, impact on the static equilibrium sea level, as do effects
302 from the earth’s rotation and solid-earth motions (e.g., Mitrovica et al., 2001; Kopp et al., 2010).
303 An interactive on-line computation of this effect on sea level has yet to be incorporated into
304 global climate models.

305 2.3. *Comments on thermosteric effects*

306 Ocean mass, heat, and salt are conserved so that their total ocean content is altered only
307 through associated boundary fluxes. In contrast, neither ocean volume nor buoyancy are con-
308 served in a mass conserving non-Boussinesq ocean. Rather, ocean volume and buoyancy are
309 altered by interior sources and sinks, even when there is no corresponding flux across the ocean
310 surface. A key reason neither are conserved relates to the nonlinear equation of state for seawater.
311 One central nonlinearity for sea level studies concerns the temperature and pressure dependence
312 of the thermal expansion coefficient

$$\alpha = -\frac{1}{\rho} \frac{\partial \rho}{\partial \Theta}, \quad (7)$$

313 where ρ is the *in situ* density and Θ is the potential or conservative temperature of seawater
314 (McDougall, 2003; IOC et al., 2010).¹ It is the thermal expansion coefficient that translates a
315 change in ocean temperature to a change in buoyancy, and thus to a change in ocean volume and
316 sea level. The thermal expansion coefficient is roughly ten times larger in the surface tropical
317 waters than surface high latitudes (Figure 1). It also reaches a minimum around 1500 m in the
318 cold abyss, but increases towards the bottom due to pressure effects (seawater is more compress-
319 ible as pressure increases). Although there are some rare regions of cold and fresh water where
320 heating increases density, in the bulk of the ocean heating reduces seawater density and so raises
321 sea level.

¹“Temperature” in this paper refers to the ocean model prognostic potential temperature or the prognostic conser-
vative temperature. The alternative *in situ* temperature is not a prognostic variable in ocean models since it does not
provide a precise measure of ocean heat (McDougall, 2003). ACCESS is the only model in this study that uses the
conservative temperature of McDougall (2003), as recommended by IOC et al. (2010). All other models use potential
temperature for their prognostic temperature field. We note that many observation-based analysis products supply *in
situ* temperature. Conversion to potential or conservative temperature is required before comparing to model output.

322 To illustrate how variations in the thermal expansion can impact on sea level changes, con-
 323 sider expression (3) for the local steric effect, and isolate the impacts from temperature tenden-
 324 cies

$$\left(\frac{\partial\eta}{\partial t}\right)^{\text{local thermosteric}} = \int_{-H}^{\eta} \alpha \left(\frac{\partial\Theta}{\partial t}\right) dz. \quad (8)$$

325 A nonzero temperature tendency arises when heat converges or diverges from a region, via either
 326 boundary heat fluxes or interior ocean heat transport. The large variations in α shown in Figure
 327 1 mean that where heat is deposited or removed determines the degree to which heating alters
 328 sea level. Furthermore, the rather large spatial gradients of α mean that transport of heat from
 329 one region to another, especially in the meridional direction, can modify sea level even without
 330 altering the total ocean heat content.

331 The horizontal map in Figure 1 indicates that tropical surface heating leads to roughly ten
 332 times larger thermosteric sea level rise than the same heating in the high latitude surface ocean
 333 (see also Lowe and Gregory, 2006). The zonal mean map indicates that heat deposited in the
 334 upper tropical ocean leads to more sea level rise than the same heat deposited to the deeper
 335 ocean. Conversely, high latitude surface heating leads to less sea level rise than deep high
 336 latitude heating. Additionally, heating generally remains in the upper tropical ocean since it
 337 is more highly stratified than the high latitude. In general, warming enhances the upper ocean
 338 stratification (e.g., Capotondi et al., 2012), and so affects how and where warming impacts sea
 339 level.

340 There is an additional complexity impacting high latitude sea level. Namely, surface warm-
 341 ing generally enhances ocean stratification and leads to reduced deep water formation in the
 342 high latitudes. As a result, heat that otherwise leaves the abyssal high latitude ocean through
 343 convective activity will remain in the abyss, thus giving rise to deep heating relative to the case
 344 where convective ventilation occurs. Sequestering warm water in the abyss in turn contributes to
 345 sea level rise, and it does so more than if the same heat was near the surface in the high latitudes.

346 The story about thermosteric sea level change is thus intimately related to the amount of heat-
 347 ing applied to the ocean, where that heating occurs, and where the heat is transported (Kuhlbrodt
 348 and Gregory, 2012; Hallberg et al., 2013). Furthermore, as the ocean warms, the efficiency by
 349 which heating raises sea level increases since the thermal expansion coefficient generally in-
 350 creases as seawater warms. That is, sea level rise through thermosteric processes accelerates as
 351 the ocean warms, with this acceleration a result of thermodynamic properties of the seawater
 352 equation of state (IOC et al., 2010).

353 2.4. Comments on halosteric effects

354 We now consider how local halosteric effects impact on sea level. For this purpose, consider
 355 expression (3) for the local steric effect, and isolate the impacts from salinity tendencies

$$\left(\frac{\partial\eta}{\partial t}\right)^{\text{local halosteric}} = - \int_{-H}^{\eta} \beta \left(\frac{\partial S}{\partial t}\right) dz, \quad (9)$$

356 where

$$\beta = \frac{1}{\rho} \frac{\partial\rho}{\partial S} \quad (10)$$

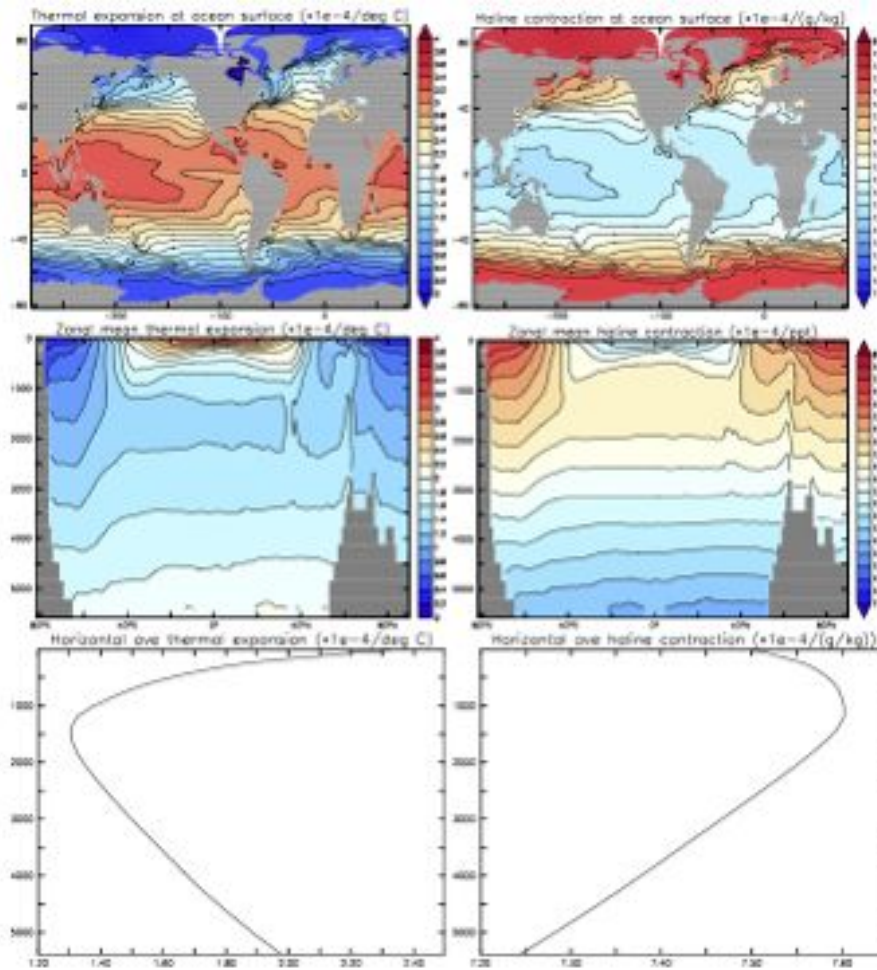


Figure 1: Left column: climatological mean thermal expansion coefficient, α (equation (7)). Right column: climatological mean haline contraction coefficient, β (equation (10)). We show values at the ocean surface, zonal average, and global horizontal mean, each multiplied by 10^4 . These results are based on a simulation using the GFDL-MOM configuration forced for 20 years using the repeating annual cycle from the Normal Year Forcing of Large and Yeager (2009) as per the protocol of Griffies et al. (2009b).

For the thermal expansion coefficient, note the larger values in the tropics (up to ten times larger than the poles); minimum around 1500 m, and increase towards the deep ocean. The global mean over the upper 1000 m is around $1.7 \times 10^{-4} \text{ } ^\circ\text{C}^{-1}$, whereas the global mean over the full ocean is roughly $1.54 \times 10^{-4} \text{ } ^\circ\text{C}^{-1}$.

The global mean haline contraction coefficient over the upper 1000 m is around $7.6 \times 10^{-4} \text{ (g/kg)}^{-1}$, whereas the global mean over the full ocean is roughly $7.5 \times 10^{-4} \text{ (g/kg)}^{-1}$. In general there is a far smaller range in values of β (only a few percent) relative to those of α (upwards of a factor of 10). The wide range of variations for α relative to the far smaller variations in β play a fundamental role in determining how surface boundary buoyancy fluxes and ocean transport/mixing impact on sea level.

357 is the haline contraction coefficient. As for ocean heating, sea level is impacted both by the
358 magnitude of the salinity tendencies, as well as spatial patterns of β . We note here two important
359 reasons why the halosteric effect is far smaller in its impacts on global mean sea level relative to
360 the thermosteric effect.

- 361 • As seen in Figure 1, the haline contraction coefficient has far less relative spatial variation
362 than corresponding variations in the thermal expansion coefficient. Values of β change on
363 the order of 5% globally, which contrasts to the factor of 10 variations seen in the thermal
364 expansion coefficient. Hence, for many purposes, it can be accurate enough to assume β
365 is constant over the globe.
- 366 • Salt is exchanged principally via the relatively small amounts associated with seasonal
367 melt and formation of sea ice. In turn, the total salt mass in the World Ocean is nearly
368 constant on climate time scales. This property holds even with trends in sea ice and the
369 measurable impact on sea level (Shepherd et al., 2010). Relatedly, the best observational
370 precision on salinity measurements is 0.002 PSS-78, which is far larger than potential
371 global mean salinity changes associated with sea ice trends. Combined with the relatively
372 small spatial variations in β , we conclude that the global halosteric effects are far smaller
373 than global thermosteric effects (see also Section A5 for more details).

374 In contrast to their global effects, halosteric contributions to regional sea level trends can
375 be significant. In particular, the North Atlantic and Arctic oceans exhibit important trends in
376 sea level associated with halosteric effects (Section 5.3). Halosteric effects are significant in
377 these regions due to the nontrivial salinity tendencies, and due to a very small thermal expansion
378 coefficient in the high latitudes that suppresses thermosteric effects. Furthermore, the absolute
379 value of the haline contraction coefficient is such that a unit change in salinity (g/kg) renders a
380 larger change in density than a unit change in temperature (degrees C).

381 2.5. Ocean model algorithmic choices directly affecting sea level simulations

382 All models used for this study assume a spherical geometry when formulating the ocean
383 equations; consider a constant gravitational acceleration; retain a static land-sea boundary; and
384 ignore impacts on sea level from the mass of the overlying atmosphere. There are further algo-
385 rithmic assumptions that directly impact on simulated sea level, with models used here choosing
386 differing approaches. In general, how an ocean model represents the sea surface height deter-
387 mines the utility of a model for studying questions about sea level.

388 2.5.1. Rigid lid approximation

389 Rigid lid Boussinesq models retain a constant ocean volume, so do not transfer water across
390 the ocean surface (Huang, 1993; Griffies et al., 2001; Yin et al., 2010b). Additionally, rigid lid
391 models do not directly compute an undulating surface height. Hence, the analyst must resort to
392 indirect methods to extract sea level information from model output, with Gregory et al. (2001)
393 providing a summary of the available methods. There is no model used in the present CORE-II
394 study that employs the rigid lid approximation, since the rigid lid method is obsolete for purposes
395 of realistic ocean climate modelling.

396 2.5.2. *Virtual tracer fluxes*

397 As meltwater from glaciers and land ice sheets mixes with the ambient seawater, it impacts
398 on the ocean baroclinic structure by modifying ocean density, with the associated modification
399 in the thickness of density layers remotely transmitted through baroclinic waves (Bryan, 1996;
400 Hsieh and Bryan, 1996; Stammer, 2008). Meltwater also initiates a much faster (roughly 100
401 times faster) barotropic ocean signal. In the matter of a few days, the barotropic signal commu-
402 nicates around the globe information about a regional change in ocean volume (Lorbacher et al.,
403 2012). Equilibration of this barotropic signal requires weeks, and equilibration of the associated
404 baroclinic signal requires decades.

405 A virtual tracer flux ocean model does not transfer water across the ocean boundary. Hence,
406 there is no direct barotropic signal in virtual tracer flux models associated with changes to ocean
407 volume (in a Boussinesq model) or mass (in a non-Boussinesq model). For example, the melt-
408 water study of Stammer (2008), which used an ocean model with virtual tracer fluxes, was only
409 able to identify baroclinic, or more precisely steric, aspects of meltwater events, whereas the
410 far more rapid barotropic signals associated with volume changes were ignored (Gower, 2010;
411 Yin et al., 2010b; Lorbacher et al., 2012). It is thus important to recognize this limitation of the
412 virtual salt flux models when assessing the regional impacts of meltwater on sea level.

413 Another limitation of virtual tracer flux models concerns the absence of a bottom pressure
414 signal in response to a meltwater flux. The addition of salt to an ocean model operationally only
415 impacts the salt equation. It does not affect the continuity equation. Hence, melting land ice,
416 implemented as a virtual salt flux as in Stammer (2008), will not modify bottom pressure in a
417 mass conserving non-Boussinesq model. It will impact bottom pressure in a volume conserving
418 Boussinesq model, but only through changes in density, with such changes a spurious result
419 of the Boussinesq approximation (see Section D.3.3 of Griffies and Greatbatch (2012)). This
420 limitation precludes virtual flux models from being used to study static equilibrium sea level
421 changes associated with ice and water mass redistributions. Studies involving mass changes are
422 of interest for investigating the impact of melting land ice, where changes in both dynamic sea
423 level and static equilibrium sea level can be comparable (Kopp et al., 2010).

424 A third limitation of virtual tracer flux models arises from the potentially different responses
425 of the overturning circulation to meltwater pulses. As shown by Yin et al. (2010b), virtual salt
426 flux models tend to exaggerate their freshening effect relative to the response seen in real water
427 flux models. As changes to the Atlantic overturning are thought to be important for regional
428 sea level changes (Yin et al., 2009; Lorbacher et al., 2010), it is useful to remove unnecessary
429 assumptions, such as virtual tracer fluxes, when considering model responses to climate change
430 associated with meltwater events.

431 Virtual tracer fluxes are typically associated with rigid lid models, though some free surface
432 ocean climate models also use virtual tracer fluxes (see Table 1). We do not consider meltwater
433 scenarios in this paper, so the limitations of virtual flux models are of no direct concern for our
434 analysis. However, the limitations are of concern for realistic coupled climate models that aim
435 to incorporate a wide suite of ocean-related processes impacting sea level (Slangen et al., 2012).
436 It is therefore critical that the analyst understand these limitations.

MODEL	OCEAN CODE	GRID SIZE	BOUSSINESQ	GEOTHERMAL $W m^{-2}$	REAL WATER	HEAT CONSERVED
ACCESS	MOM	1deg x 50	yes	0	yes	yes
AWI	FESOM	1deg x 46	yes	0	no	yes
Bergen	Bergen	1deg x 51	no	0	no	yes
CERFACS	NEMO	1deg x 42	yes	0.084	yes	yes
CNRM	NEMO	1deg x 42	yes	0.084	yes	yes
FSU	HYCOM	1deg x 32	no	0	no	no (+1W m ⁻²)
GFDL-GOLD	GOLD	1deg x 63	yes	0.06	yes	yes
GFDL-MOM	MOM	1deg x 50	yes	0.06	yes	yes
ICTP	MOM	2deg x 30	yes	0.06	yes	yes
Kiel	NEMO	0.5deg x 46	yes	0	yes	yes
MRI	MRI.COM	1deg x 50	yes	0	yes	yes
NCAR	POP	1deg x 60	yes	0	no	yes
NOCS	NEMO	1deg x 75	yes	0	yes	yes

Table 1: Summary of various properties of the ocean models used in this study, with focus here on choices that directly impact on simulated sea level. Many further details important for the CORE-II configurations chosen by the model groups are provided in the appendices to Danabasoglu et al. (2014). The first column of this table gives the model name, and the second column notes the name of the ocean model code. The next column provides the horizontal grid resolution and vertical degrees of freedom. All models have non-uniform grids in the both the horizontal and vertical, so the horizontal resolution is a nominal value that roughly corresponds to the indicated uniform grid resolution. The fourth column notes whether the model kinematics uses the volume conserving Boussinesq approximation or mass conserving non-Boussinesq formulation. The fifth column indicates the global mean of the geothermal heat flux, with most models choosing not to use geothermal heating. Note that all models that use geothermal heating apply it according to a regional pattern, with just the global ocean mean reported in this table. The sixth column notes whether the ocean model uses a real water flux for evaporation, precipitation, and rivers, or rather a virtual salt flux. The seventh column notes whether the model conserves total ocean heat, as determined by comparing the global mean temperature evolution to the ocean boundary heat fluxes (Appendix C2). FSU-HYCOM is the only model that fails to conserve heat, with an estimated heat non-conservation of +1 W m⁻².

2.5.3. Boussinesq approximation

As noted in Section 2.2, the prognostic sea surface height produced by a volume conserving Boussinesq ocean model does not account for changes in sea level due to global steric effects (Greatbatch, 1994). Furthermore, the mass of seawater in a column of Boussinesq fluid is affected by spurious sources and sinks, since changes in density in a volume conserving fluid are associated with mass changes. Hence, the Boussinesq model requires corrections in order to study impacts on the geoid and earth rotation associated with changing seawater mass distributions (Bryan, 1997; Kopp et al., 2010). Nonetheless, as noted in Section 2.2, there is a broad agreement between the large-scale patterns of dynamic sea level produced in Boussinesq and non-Boussinesq ocean climate simulations (Losch et al., 2004; Griffies and Greatbatch, 2012). Thus, in practice, ocean climate modellers need only be concerned with global corrections to the Boussinesq sea level to account for steric effects on the global mean. Salient details are given in Appendix A. All but two of the ocean models considered in this paper use a volume conserving Boussinesq formulation (Table 1).

2.5.4. Conservation of heat and salt

From the ocean climate perspective considered in this paper, the sea level question relates to how and where heat and salt are fluxed across ocean boundaries, and then transported within the ocean, with the associated buoyancy anomalies giving rise to regional and global steric sea

455 level changes. In particular, for global mean sea level, changes arise from the net heat fluxed
456 across the ocean surface. This heat flux is the relatively small residual of large fluxes arising
457 from many heating components such as shortwave, longwave, latent, and sensible. A necessary
458 condition to reliably simulate thermosteric sea level change is that the numerical model conserve
459 heat, locally and globally, preferably at the level of computational roundoff. The same level of
460 precision is needed for salt in order to properly capture halosteric sea level changes, particularly
461 those contributing to regional patterns (Durack et al., 2012; Church et al., 2013).

462 The conservative evolution of ocean heat or salt means that heat and salt both satisfy a con-
463 servation law whereby their evolution within a region is impacted only through fluxes crossing
464 region boundaries. It does not mean that the property (i.e., heat or salt) remains constant in
465 time within the region. So when examining the heat conservation properties of the CORE-II
466 ocean models in Appendix C, we examine whether the total heat within the global ocean model
467 evolves according to the heat flux crossing the ocean boundaries. If we need to invoke a signif-
468 icant internal source or sink to explain the heat budget, then we conclude that the model is not
469 conservative. These comments are relevant also for sea level studies using ocean data assim-
470 ilated models or state estimates. Methods such as those used in the state estimation of Wunsch
471 et al. (2007) ensure that the ocean tracers maintain a physically appropriate conservation equa-
472 tion (see Wunsch and Heimbach (2013) for a review). Other methods commonly associated with
473 prediction systems (see Schiller et al. (2013) for a review) employ internal sources and sinks that
474 in turn compromise their utility for sea level studies.

475 One of the models used in the present study is not conservative (Table 1). This model,
476 HYCOM, has been shown to exhibit similar non-conservation behaviour when coupled to an
477 atmospheric model for purposes of studying global climate (Megann et al., 2010). However,
478 there is a new version of HYCOM that in fact conserves heat and salt, to within computational
479 roundoff (Rainer Bleck and Shan Sun, personal communication 2013). A suitable CORE-II
480 simulation using this updated code was not available in time for inclusion in the present study.

481 2.6. Global mean SST in the CORE-II simulations

482 Figure 2 shows the time series for global mean sea surface temperature (SST) from the
483 simulations over the fifth CORE-II cycle. Time series for the models reach a cyclo-stationary
484 state, so that each of the five CORE-II cycles show nearly the same temporal behaviour of SST
485 for the respective models. It is striking how well the various models agree in their SST evolution,
486 with interannual fluctuations aligned across the models. This result follows from the large impact
487 on SST from the common CORE-II atmospheric state of Large and Yeager (2009).

488 2.6.1. Discrepancy between observed SST and CORE-II simulated SST

489 The CORE-II simulations exhibit a slight jump in SST around 1980 associated with the
490 climate regime shift (discussed in Trenberth and Hurrell (1994) and Meehl et al. (2009)), after
491 which time they transition to a higher SST and then fluctuate around this higher decadal mean
492 value until 2007. This transition is present in the 10 m air temperature based on the NCEP
493 reanalysis (Kalnay et al., 1996) used in the CORE-II atmospheric state (third panel of Figure 2).
494 The global mean SST in all CORE-II simulations is roughly $0.1 - 0.2^{\circ}\text{C}$ warmer at the end of
495 2007 than the start of 1948.

496 The transition from 2007 back to 1948 presents an unphysical periodic element to the CORE-
497 II simulations. The amplitude of the transition, in the global mean, is about $0.1 - 0.2^{\circ}\text{C}$, cor-
498 responding to the rise in SST over the 60 years of the cycle. Even if the CORE-II atmospheric
499 state of Large and Yeager (2009) was a perfect rendering of the real atmosphere, the periodicity
500 $1948 \rightarrow 2007 \rightarrow 1948 \rightarrow \text{etc.}$ introduces a lag to the ocean response to low frequency vari-
501 ability, with the lag time directly related to the time scale for the ocean to equilibrate. We thus
502 expect that the CORE-II simulations of global mean sea level will lag behind observation-based
503 sea level estimates.

504 A notable feature seen in the third panel of Figure 2 is the difference between the amount
505 that SST increases in the CORE-II simulations relative to that found in the observation-based
506 analysis of Hurrell et al. (2008). Although there is a positive correlation between interannual
507 SST fluctuations, the CORE-II ensemble mean SST is roughly $0.1 - 0.2^{\circ}\text{C}$ warmer at the end of
508 2007 than the start of 1948, whereas the Hurrell et al. (2008) SST is roughly 0.4°C warmer over
509 the same period. There is a notable absence in the CORE-II simulations of a positive SST trend
510 post-1980, even though there is a trend in the air temperature in the CORE-II forcing (Figure 2).
511 We note that the SST trends in the Hurrell et al. (2008) analysis is sensitive to the assumptions
512 made about sea ice. For the time series shown here, we do not mask regions under sea ice, which
513 accords with the approach used for the models.

514 2.6.2. SST evolution in the NCAR CORE-II simulation

515 A thorough exploration of the SST evolution is beyond our scope. Nonetheless, we expose
516 some details from the NCAR CORE-II simulation to more fully describe the behaviour during
517 the period post-1984 (where satellite information is more complete for the CORE atmospheric
518 state), and to illustrate the difficulty uncovering cause and effect. To furthermore remove ques-
519 tions about sea ice impacts on surface fluxes, we consider only the region between $40^{\circ}\text{S} - 40^{\circ}\text{N}$.

520 The air temperature in the CORE-II atmospheric state post-1984 increases in response to the
521 increase in SST used as part of the NCEP reanalysis. The air temperature rise leads to a reduction
522 in sensible cooling of the ocean in the NCAR CORE-II simulation by roughly 1 W m^{-2} (i.e.,
523 an increase in ocean heating). The air humidity also rises by about 0.2 g kg^{-1} . For a constant
524 SST and surface humidity, the rise in air humidity leads to a decrease in evaporation and thus
525 a further increase in ocean heat flux by about 2.5 W m^{-2} . The combined sensible and latent
526 change of more than 3 W m^{-2} is balanced by a decrease in the ISCCP-FD satellite downwelling
527 longwave heating by about the same amount (Large and Yeager, 2012). The net heat flux into
528 the ocean is therefore near 0 W m^{-2} , which is reflected in the approximately constant SST in the
529 NCAR CORE-II simulation after 1984 (Figure 2). This near-zero net heat flux is also consistent
530 with the five-cycle spin-up nearly achieving a steady state for the NCAR CORE-II simulation
531 (see Figure 3 discussed in Section 3.1).

532 We now consider the case of fluxes computed based on the CORE-II atmospheric state and
533 the observation-based SST of Hurrell et al. (2008). In this “observed” case, the rising SST warms
534 and moistens the atmosphere as for the NCAR CORE-II simulation. However, the resultant
535 increase in the surface air temperature is less than the rise in SST (see Figure 10 from Bates
536 et al. (2012)). Because the rising SST outpaces the increase in surface air temperature between
537 1984 and 2007, both the latent and sensible heat fluxes become more negative (i.e. cooling the

538 ocean) by -5.3 W m^{-2} and -1 W m^{-2} , respectively. The only mechanisms that could allow
539 for SST to increase in the presence of cooling air-sea fluxes is a through warming induced by
540 ocean circulation or mixing. Large and Yeager (2012) infer that a reduction in mixing across
541 the thermocline is likely responsible for the SST rise over this period; i.e., reduction in upwelled
542 cold waters. Such an effect could not continue indefinitely, in which case SST would be expected
543 to stop rising at some point, which indeed it has. This analysis suggests that the CORE-II
544 simulations do not simulate the natural variability in the upper ocean boundary layer that leads
545 to this inferred change in vertical mixing, at least over the years 1984-2007 Large and Yeager
546 (2012).

547 2.6.3. *Connection to global mean sea level*

548 If the global mean ocean temperature was directly a function of the SST, then we may expect
549 the CORE-II simulations to be biased low in regards to volume mean global ocean heating, as
550 indeed they are (Section 3). However, there are many other factors that impact on volume mean
551 ocean heat, including model drift, sea ice effects, and long-term adjustment to surface heating.
552 It is therefore not generally possible to infer that volume mean global ocean heat changes will
553 be lower than observations just because SST increases less than observations in the CORE-II
554 simulations. So although we find the CORE-II simulations to be generally biased low in their
555 volume mean ocean heat trends, a deductive story explaining this low-bias is available only after
556 far more analysis than presented in this paper. We note that any such analysis is associated with
557 far more observational uncertainty than associated with an analysis of SST evolution.

558 2.7. *Restricting our analysis to the 15 years 1993-2007*

559 The study from Doney et al. (2007) considered four cycles of 40-year simulations using an
560 earlier version of the Large and Yeager (2009) atmospheric state. They compared SST patterns to
561 the observation-based estimates from Reynolds et al. (2002), and found good agreement between
562 model and observations for the first two empirical orthogonal functions. The agreement between
563 modelled and observed patterns of variability is consistent with the close correlation between
564 interannual fluctuations in the global mean SST shown in Figure 2. However, it does not imply
565 that the lower frequency trends match, as indeed they do not.

566 The study of Large and Yeager (2012) considered many features of ocean surface fluxes that
567 impact on the SST within the context of the CORE-II atmospheric state of Large and Yeager
568 (2009), using the SST from Hurrell et al. (2008) to generate these fluxes. Differences in ocean
569 surface fluxes in the Large and Yeager (2012) study relative to the CORE-II simulations arise
570 from differences in the simulated SSTs. As with Doney et al. (2007), the papers from Large and
571 Yeager (2009) and Large and Yeager (2012) emphasize that the CORE-II atmospheric state is
572 suited mostly for studies of interannual variability, rather than longer term multi-decadal trends
573 such as that associated with anthropogenic warming. Our focus on 15 year trends pushes the
574 envelope over which the atmospheric state is of use.

575 Doney et al. (2007) and Large and Yeager (2012) identify many reasons to focus analyses
576 on the latter portion of the CORE-II simulations. A notable reason is that it is not until 1984 that
577 satellite information is used for radiation, with climatology used in earlier years. As discussed
578 in Large and Yeager (2012), there is a nontrivial “shock” to the atmospheric state (and hence to

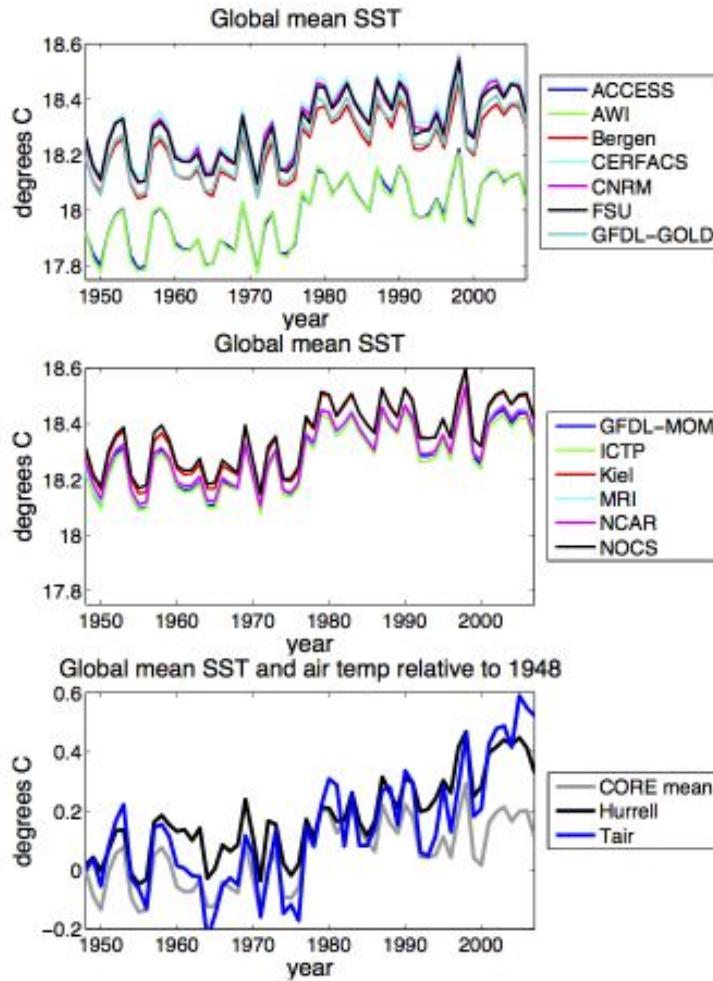


Figure 2: Time series for global area mean sea surface temperature (SST) for the fifth CORE cycle. Time series for all of the models rapidly reach a cyclo-stationary state, so that global mean SST is nearly the same for each of the five cycles. We do not know why ACCESS and AWI-FESOM show a consistently low offset from the other models. All models show a transition centred around 1975 to higher values extending to the end of the simulation, with this transition associated with the climate regime shift discussed in Trenberth and Hurrell (1994) and Meehl et al. (2009). Throughout the 60 years shown, there is a strong correlation between interannual SST fluctuations in the CORE-II simulations and the Hurrell et al. (2008) observation-based analysis (third panel). However, all models show about half the magnitude of the upward long-term SST trend relative to Hurrell et al. (2008), as revealed by the third panel that shows the CORE-II ensemble mean, air temperature used for the CORE-atmosphere, and the Hurrell et al. (2008) analysis, relative to their respective values at 1948. Whereas the CORE-II ensemble mean is roughly $0.1 - 0.2^{\circ}\text{C}$ warmer at the end of 2007 than the start of 1948, the Hurrell et al. (2008) analysis is roughly 0.4°C warmer over the same period. There is a notable absence in the CORE-II simulations of a positive SST trend after 1980, which contrasts to the air temperature and the SST analysis from Hurrell et al. (2008).

579 ocean boundary heat fluxes) associated with introducing the satellite radiation, mostly arising
580 from changes to the downward long wave radiation. There is additional motivation to focus
581 analysis on years 1993-2007, since we can make use of satellite sea level measures to directly
582 compare against the CORE-II simulations (e.g., Figures 15–17).

583 Based on these considerations, we consider the four early CORE cycles, as well as the years
584 prior to 1993 in the fifth cycle, as part of a spin-up phase. We discuss aspects of this spin-up
585 in Section 3 to expose elements of long-term model drift. Yet we focus analysis on the final
586 15 years of the fifth CORE cycle throughout the bulk of this paper, with this period the only
587 one that we directly compare to observation-based analyses. This period is relatively short,
588 meaning that a great deal of the simulated trends in sea level and ocean heat content arise from
589 natural variability (e.g., Zhang and Church, 2012) rather than longer-term anthropogenic effects.
590 Our comparison between CORE-II simulations and observation-based analyses, especially of
591 subsurface ocean properties, can be viewed as a common evaluation of two imperfect measures
592 of the recent ocean.

593 2.8. CORE-II ensemble means & comparison to observation-based analyses

594 For many results presented in this paper, we compute differences between simulations and
595 observation-based analyses. Additionally, we find it very useful to compute an ensemble mean
596 of the CORE-II simulations. For both purposes, we first map the simulation results to a common
597 spherical coordinate grid, and if necessary to a common vertical grid.² Quantitative model-
598 model and model-observation comparisons are performed with all results on the common grid.
599 The CORE-II ensemble mean is also computed on this common grid, with equal weighting to all
600 models. We make use of the CORE-II mean especially for the summary discussion in Section 6.

601 We use of the following observation-based analyses to compare against the CORE-II simu-
602 lations.

- 603 • We already encountered the HadSST3 sea surface temperature analysis in Figure 2. We
604 make use of an updated version of that described by Kennedy et al. (2011) and available
605 from the web site <http://www.metoffice.gov.uk/hadobs/hadsst3/>.
- 606 • The analysis of Levitus et al. (2012) provides estimates for the upper 700 m ocean heat
607 content and associated thermosteric sea level. This analysis is used as part of Figures 8,
608 13, 14, and 26. Note that heat content trends require the conversion of *in situ* temperature
609 to potential temperature. For this purpose, we used the World Ocean Atlas climatologi-
610 cal salinity (Antonov et al., 2010) and *in situ* temperature (Locarnini et al., 2010) (both
611 relative to 1957-1990), and the anomalous *in situ* temperature, and used these fields to
612 compute the trend in potential temperature.
- 613 • We make use of an updated version of the analysis of Domingues et al. (2008) and Church
614 et al. (2010), again for use in the upper 700 m ocean heat content and associated ther-
615 mosteric sea level found in Figures 8, 13, 14, and 26.

²We performed this remapping using tools available within the NOAA/PMEL Ferret free-software package.

616 • The Durack and Wijffels (2010) analysis extends over the upper 2000 m of the ocean. This
617 analysis is based on profiles containing both temperature and salinity. This approach has
618 the advantage that no corrections are necessary to remove instrumental biases in XBTs
619 or MBTs discussed in Wijffels et al. (2008). However, the total number of profiles used
620 by Durack and Wijffels (2010) is well under one-half of those used in the Levitus et al.
621 (2012) analyses.

622 We make use of an updated version of the Durack and Wijffels (2010) analysis of tempera-
623 ture changes, with results presented in Figure 13 for the upper 700 m heat content change,
624 and Figure 14 for the upper 2000 m zonal temperature change. We also use their analysis
625 for upper 700 m steric, thermosteric, and halosteric trends shown in Figures 25, 26, and
626 27. As part of the updated analysis, we did not filter interannual signals associated with
627 El Niño Southern Oscillation. Eliminating this filter, which is used in the original Durack
628 and Wijffels (2010) analysis, allows for the updated analysis to be directly comparable to
629 the CORE-II simulations and to the other observation-based analyses.

- In Figures 15, 16, and 17, we make use of the dynamic sea level available from the gridded satellite altimeter product from the AVISO project (Archiving, Validation, and Interpolation of Satellite Oceanographic Data) (Le Traon et al., 1998; Ducet et al., 2000). The particular version of this product was taken from NASA’s Jet Propulsion Laboratory on the web site

podaac.jpl.nasa.gov/dataset/AVISO_L4_DYN_TOPO_1DEG_1MO.

- In Section 3.5, we discuss further observation-based analysis products and some of the caveats regarding their use.

632 3. Steric impacts on global mean sea level

633 The CORE protocol (Griffies et al. (2009b) and Danabasoglu et al. (2014)) introduces a neg-
634 ligible change to the liquid ocean mass (non-Boussinesq) or volume (Boussinesq), and the salt
635 remains nearly constant (except for relatively small exchanges associated with sea ice changes).
636 For simulations with zero net water crossing the ocean surface and constant salt content, changes
637 to the simulated global mean sea level arise predominantly through the global mean of ther-
638 mosteric effects. That is, global mean sea level will change due to changes in ocean heat content
639 and redistribution of heat.

640 Not all models considered in the present study strictly adhered to the CORE protocol (see
641 full details in Danabasoglu et al. (2014)), in that their water content and/or salt content changed
642 during the simulation far more than just via exchange with sea ice. Nonetheless, for all models
643 except one (see Figure 3), we find that changes in global mean steric sea level are dominated by
644 changes in global mean ocean temperature. Halosteric effects generally become important when
645 considering patterns of sea level, either in the horizontal (Section 5) or vertical (Section 3.4).
646 We are, unfortunately, unconvinced that details of the halosteric patterns are physically robust
647 since the CORE-II simulations use surface salinity relaxation, which has no counterpart in the

648 real climate system (see Section 3 of Griffies et al., 2009b). This caveat must remain part of
649 interpreting the impacts of salinity on regional sea level in the CORE-II simulations (Section 5).

650 We gave many reasons in Section 2 to focus our assessment on years 1993-2007. Nonethe-
651 less, it is of interest to expose some of the longer term features of the simulations, and we do so
652 in this section. This presentation serves to illustrate the different drift properties of the simula-
653 tions, and allows us to ask general questions about heat and salt conservation (Appendix C2). It
654 also provides further motivation to limit our analysis to 1993-2007. Quite simply, a comparison
655 of global mean behaviour in the CORE-II over longer time scales is fraught with huge difficulties
656 and caveats.

657 3.1. Global mean ocean temperature and sea level: the five CORE-II cycles

658 Figure 3 exhibits time series of global mean ocean temperature and global steric sea level
659 from the suite of CORE-II simulations. Although aiming to initialize the models using the same
660 analysis from Steele et al. (2001), the initial global mean ocean temperature in fact slightly
661 differs for the various models. We conjecture that the differences are associated with details for
662 how the models interpolate from the Steele et al. (2001) grid to the model grid, with differences
663 in model topography also impacting the initial global mean values.

664 It is useful to contrast the drift in global mean ocean temperature shown in Figure 3 with that
665 of the relatively stable global mean SST in Figure 2. Again, SST in the CORE-II simulations is
666 largely constrained by the prescribed CORE-II atmospheric state of Large and Yeager (2009). In
667 contrast, global mean ocean temperature and sea level are a function of the global mean surface
668 fluxes, which are in turn a function of the simulated SST, ocean surface currents, and sea ice
669 cover. Each model differs in numerical formulations, physical parameterizations, and/or grid
670 resolution, each of which contributes to differences in simulation features, particularly when
671 considering multi-decadal and longer simulations. We therefore expect the models to exhibit
672 differing drifts over the course of the five CORE-II cycles.

673 For all but two models, the simulated global mean ocean temperature increases. Rising
674 global mean temperatures may be expected, since the observational record from 1961-2008
675 shows an ocean warming trend (Church et al., 2011). However, this expectation must be qual-
676 ified by noting that the ocean initial conditions from Steele et al. (2001) do not correspond to
677 those at 1960. The models that exhibit a small trend include NCAR, in which case there is a
678 negligible overall trend for the full 300 years. Those models with negligible global mean tem-
679 perature drift are in close balance with the atmospheric state, so that the global mean heat flux
680 crossing the ocean boundary is nearly zero. The GFDL-GOLD simulation is an outlier as it
681 has a negative trend throughout the five cycles. The negative temperature trend in this model is
682 largely associated with abyssal and deep cooling, much of which originates from the Southern
683 Hemisphere and spreads throughout the deep ocean (not shown).

684 Along with global volume mean ocean temperature, we also show in Figure 3 the anomalous
685 global mean sea level as determined by global steric effects. This *steric sea level* is computed
686 according to equation (29) discussed in Appendix A3. The time series is initialized at the first
687 year of the first cycle to have zero anomaly, thus allowing for a direct comparison of the relative
688 change in global steric sea level between simulations in the model suite over the course of the five
689 cycles. As expected based on the discussion in Appendix A5, the global mean sea level changes
690 associated with steric effects largely follow the behaviour in global volume mean temperature.

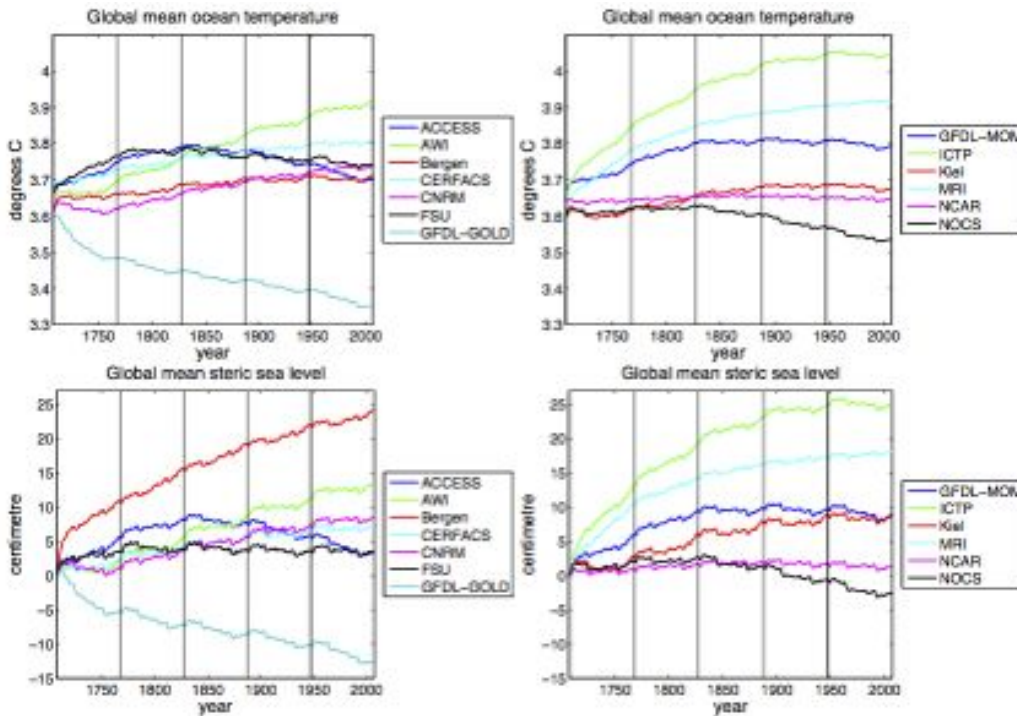


Figure 3: Time series for global volume mean annual ocean temperature and global mean annual steric sea level as computed in the interannual CORE-II simulations. Each panel illustrates drift in the various models over the five CORE-II cycles. Note the nominal start year of 1708 allows for a continuous increase in time over the 300 years of the five-times repeated cycles of the interannual CORE-II atmospheric state (years 1948-2007). The vertical lines denote the start of a new CORE-II cycle. The global mean sea level arising from global steric effects is computed according to equation (29). The diagnostic global mean steric sea level for each model is separately initialized at zero in order to emphasize trends in the respective simulations. Note the close correspondence between the global mean steric sea level and the global volume mean temperature (see Section A5). The Bergen model is an exception, in which global steric sea level rises much more than global volume mean temperature. The steric sea level rises in this model largely due to a decrease in global volume mean salinity, where the salinity decrease is associated with the lack of zero normalization of the surface restoring salt-flux.

691 3.2. Global mean salinity and sea level: details of surface salinity restoring

692 In Figure 3, we see that the Bergen simulation exhibits a global mean steric sea level that
 693 rises far more relative to the global mean temperature. This behaviour is distinct from the other
 694 models, in which the global mean steric sea level parallels global volume mean temperature. For
 695 the Bergen model, global mean steric sea level rises due to a nontrivial decrease in global mean
 696 salinity. This global mean salinity decrease arises from the absence of a global adjustment to
 697 zero the net salt crossing the ocean associated with the surface restoring salt flux.

698 Details of the salt flux adjustment, or “normalization”, are discussed in Appendix B.3 of

699 Griffies et al. (2009b) and Appendix C in Danabasoglu et al. (2014). In effect, the adjustment
700 ensures there is no net salt added to or removed from the ocean-sea ice system associated with
701 the restoring. We note that some models convert the surface salinity restoring into an implied
702 surface freshwater flux. In this case, an adjustment must be made to ensure there is no net water
703 added to or subtracted from the ocean-sea ice system as a result of the restoring. As the surface
704 restoring has no physical counterpart in the real climate system, there is nothing more or less
705 physical about choosing to use a restoring salt flux or restoring water flux.

706 Returning to the Bergen simulation, we see that without an adjustment to zero the net surface
707 salt flux, the global mean steric sea level has a significant contribution from the halosteric effect
708 due to drift in ocean salt content. In contrast, all other CORE-II models are dominated by the
709 global thermosteric effect. This result emphasizes the need for models to adjust their restoring
710 salt flux (or restoring water flux) to be zero globally in order to avoid a potentially nontrivial
711 drift in global mean sea level.

712 *3.3. The fifth CORE-II cycle and years 1993-2007*

713 Drift in deep ocean temperature plays a role in the temperature and steric sea level trends
714 seen in Figure 3. Due to the nature of the CORE-II simulations, we cannot remove drift by
715 subtracting a “control” (see Section 2.1). Instead, we focus on the fifth cycle, where in general
716 (though not universally) the global volume mean temperature drift is smaller than for earlier
717 cycles. For this purpose, we recompute the anomalous global mean sea level over just the fifth
718 cycle (i.e., impose a zero anomaly at the start of the 5th cycle), with this result shown in Figure
719 4.

720 In Figure 4, we note certain downturns in global mean steric sea level associated with vol-
721 canic eruptions in 1963/1964 (Agung); 1982 (El Chichón); and 1991 (Pinatubo), as reflected in
722 the observational estimates from Church et al. (2011). Furthermore, eight of the 13 models have
723 higher global mean sea level at year 2007 relative to 1948. This result is consistent with the
724 observational estimates from Church et al. (2011), in which global mean sea level rises due to
725 ocean warming over the years 1961-2008. However, the CORE-II simulations for this period are
726 biased on the low side relative to observations, and we return to this point in Section 3.5 when
727 discussing upper ocean thermosteric sea level. We noted some reasons for a low bias in Section
728 2.6.

729 As a final refinement to our analysis period, we present in the second panel of Figure 4 the
730 global mean steric sea level anomalies referenced to 1993 in the fifth CORE-II cycle. It is only
731 when focusing on this final 15 years of the simulation that nearly all of the models exhibit a rise
732 in global mean sea level (albeit only a slight rise in some models). We compare to observation-
733 based estimates over this time period when discussing thermosteric sea level in Section 3.5.

734 *3.4. Vertical dependence of steric, thermosteric, and halosteric sea level rise*

735 Figure 5 shows the vertical projection of steric impacts on sea level as a function of time
736 over years 1993-2007; Figure 6 shows the corresponding thermosteric component; and Figure
737 7 shows the halosteric component. These vertical-time patterns are the integrands of equations
738 (55)–(57) discussed in Appendix B1.

739 Long term temperature and salinity trends, or drift, become apparent in deeper portions of
740 the water column. Furthermore, the lack of agreement between models in the deep ocean is

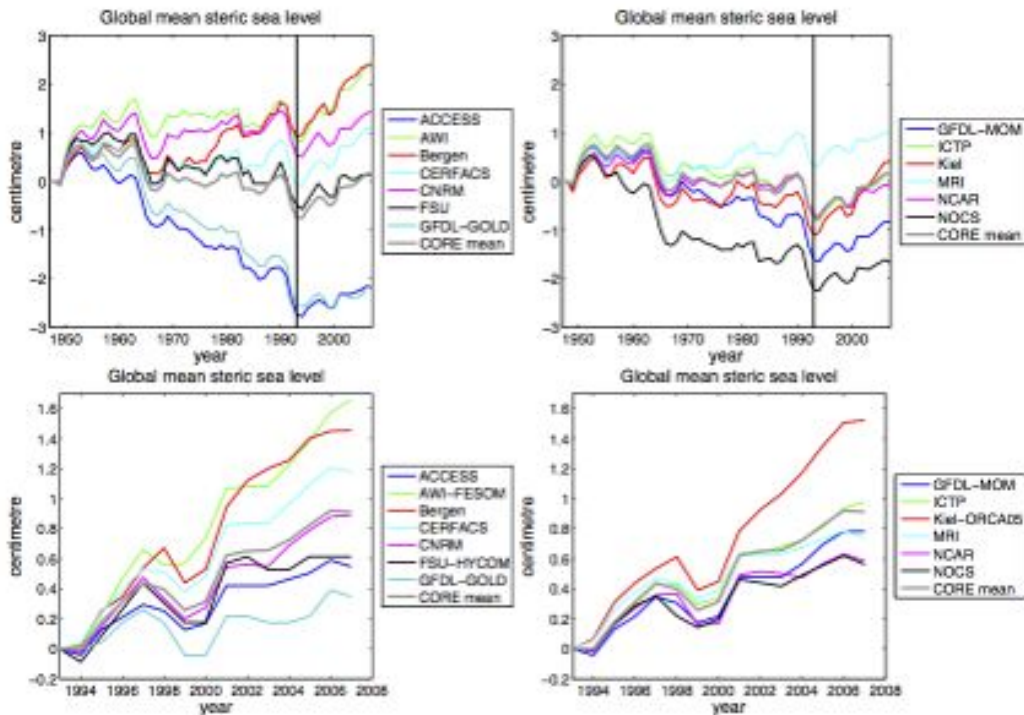


Figure 4: Time series for global mean steric sea level in the fifth cycle of the CORE-II simulations. The first row shows the global mean sea level arising from global steric effects, referenced to the start of the fifth cycle rather than the start of the first cycle (Figure 3). There are notable downturns in global mean steric sea level associated with volcanic eruptions in 1963/1964 (Agung); 1982 (El Chichón); and 1991 (Pinatubo). Note that many models show a gradual decrease in global mean sea level over the 60 year simulation, until around year 1993 (denoted by a vertical line) at which point most models then show a gradual increase. The second row focuses just on the years 1993-2007 for the fifth CORE-II cycle in order to highlight the increase over the final 15 years, with the global mean now computed relative to 1993. Note the different vertical axis for the two rows. The ensemble mean for the CORE-II simulations over 1993-2007 rises by about 0.8 cm over the 15 years, which is consistent with the observational range for thermosteric sea level of $15 \text{ yr} \times (0.6 \pm 0.2 \text{ mm yr}^{-1})$ from Church et al. (2011).

741 indicative of differing drift. We thus focus attention on the upper 700 m, given its lower degree
 742 of model drift and significantly better observational sampling (Section 3.5). Contributions to
 743 steric sea level change in the upper 700 m are predominantly associated with thermosteric effects,
 744 though most models (except Kiel-ORCA05) also show a slightly negative halosteric effect in this
 745 depth range. Due to the differing treatment of surface salinity restoring (see Danabasoglu et al.
 746 (2014) for details), we are not convinced of the physical reliability of the simulated halosteric
 747 patterns seen in Figure 7. Additionally, we found no systematic connection between surface
 748 salinity restoring strength and the behaviour seen in Figure 7. For the thermosteric patterns
 749 shown in Figure 6, there is a general agreement between the models, though with differing

750 magnitudes. Some of the models show a slight cooling trend centred around 200 m depth, with
751 the ICTP, Kiel-ORCA05, and MRI simulations the most prominent. These cooling trends act to
752 suppress thermosteric sea level rise in the upper 700 m for these three models (see Figure 8).

753 3.5. Heat content and thermosteric sea level rise

754 Comparisons to observations must be considered with the appropriate caveats. Uncertainties
755 in thermosteric sea level changes are largest for early years of the historical record (before 1970);
756 below 400 m before the frequent use of deep XBTs in the mid-1990s; below 700 m before
757 the Argo array achieved near-global ocean coverage in 2005; and in the Southern Hemisphere
758 (especially south of 30°S) before Argo (see Figure 2 in Wijffels et al. (2008) for evolution of
759 the archive of thermal observation platforms). Current Argo float technology does not allow for
760 full-depth profiling. Hence, we continue to have poor sampling below 2000 m, which means
761 we do not sample roughly 50% of the total ocean volume. Observation-based differences also
762 exist for ocean heat content in the upper 700 m even in historically well-sampled regions, such
763 as the North Atlantic (Gleckler et al., 2012). Although consistent with the rates estimated for
764 the multi-decadal periods, the thermosteric sea level rate for the Argo period (2005-present) is
765 unlikely to represent long-term changes. Over such a short period, long-term changes can be
766 easily obscured by more energetic ocean variability, such as fluctuations in the phase of the El
767 Niño Southern Oscillation (Roemmich and Gilson, 2011).

768 We consider estimates for observed thermosteric sea level anomalies for the upper 700 m of
769 ocean and within the latitude range 65°S – 65°N, as based on recent Argo data as well as histor-
770 ical bottle, CTD and XBT data, the latter with fall-rate corrections from Wijffels et al. (2008).
771 Domingues et al. (2008) determine a trend between the years 1971-2010 of $0.6 \pm 0.2 \text{ mm yr}^{-1}$,
772 with this estimate consistent with the more recent Argo data analyzed by Leuliette and Willis
773 (2011). Levitus et al. (2012) provide an estimate of $0.1 \pm 0.1 \text{ mm yr}^{-1}$ for depths between
774 700–2000 m. Purkey and Johnson (2010) then estimate a contribution of $0.1 \pm 0.1 \text{ mm yr}^{-1}$ for
775 abyssal and deep waters in the Southern Ocean. For our purposes, we take an estimated global
776 thermosteric sea level rise to be $0.8 \pm 0.4 \text{ mm yr}^{-1}$, which follows that used in Church et al.
777 (2011) and Hanna et al. (2013) for the full depth integrated global steric sea level.

778 The CORE-II simulations generally show an upper 700 m ocean warming for the 15 years
779 1993-2007 (Figure 8). Corresponding to the warming is an increasing global steric sea level rise
780 over the same period. A low end to the observational estimates of thermosteric rise in the upper
781 700 m suggests a sea level rise of $0.4 \text{ mm yr}^{-1} \times 15 \text{ yr} = 0.6 \text{ cm}$, whereas a high end yields
782 $0.8 \text{ mm yr}^{-1} \times 15 \text{ yr} = 1.2 \text{ cm}$. Wunsch et al. (2007) reported a global mean steric sea level rise
783 of roughly 0.5 mm yr^{-1} over the years 1993-2004 using a state estimation system.

784 Estimates of steric sea level from observations consider only thermosteric effects. This fo-
785 cus arises from the smaller uncertainties in temperature measurements than salinity. It is also
786 justified by the generally small contributions to global mean sea level from halosteric effects
787 (see Appendix A5 and the corresponding Figure 36). To compare the CORE-II simulations to
788 the observation-based estimates, we display in Figure 8 the global heat content and global mean
789 thermosteric contribution to simulated sea level from the depth ranges 0-700 m, and Figure 9
790 shows the global mean thermosteric sea level from the depth range 700-2000 m. The deeper
791 thermosteric changes are generally consistent with the slow rise seen in the observational es-
792 timates. For the upper ocean, the observational range is reflected by the bulk of the CORE-II

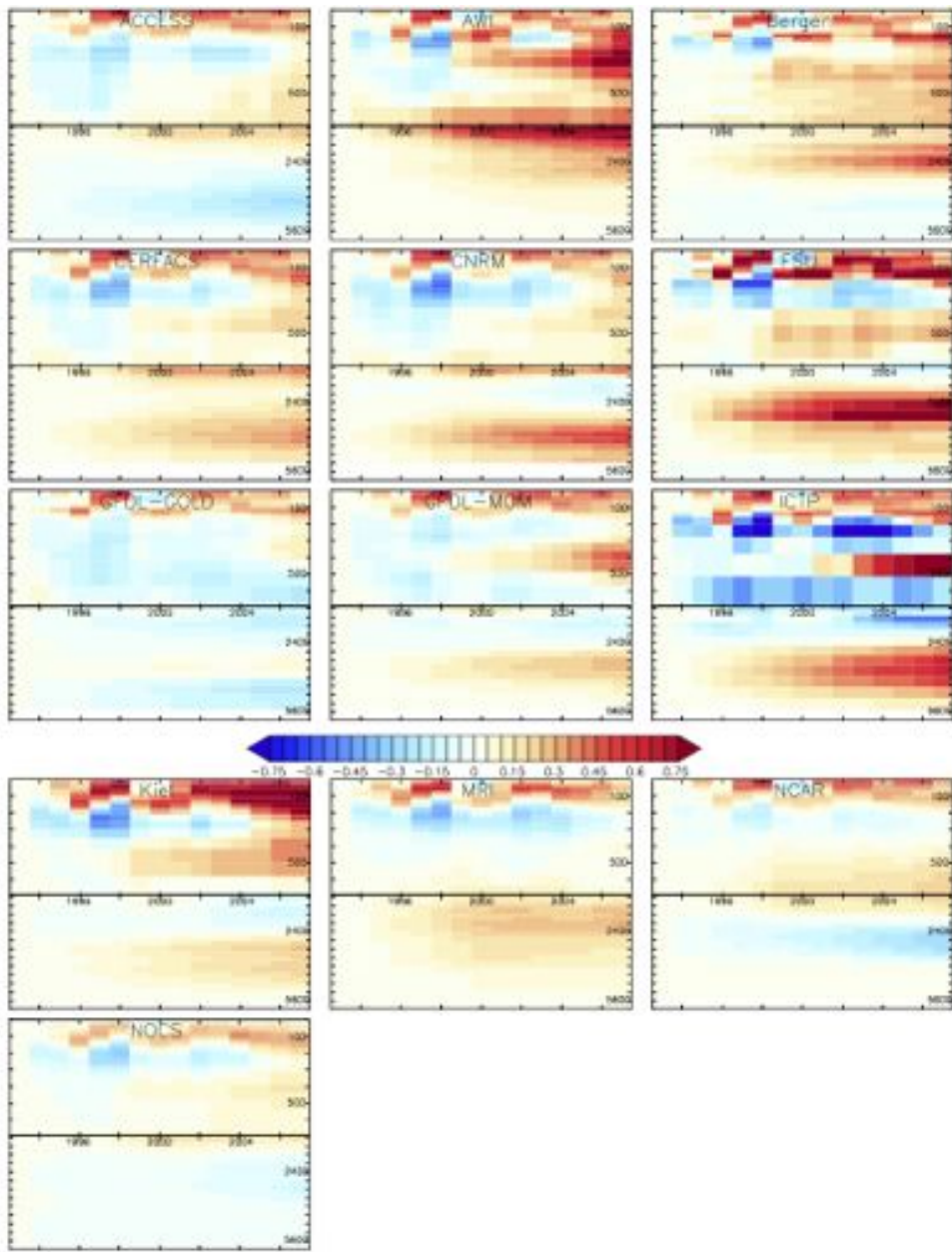


Figure 5: Time series for the horizontally integrated annual mean contributions to steric sea level as a function of depth (in metres), during the years 1993-2007 of the fifth CORE-II cycle. The units are millimetres, and the vertical sum yields the time series for the global mean steric sea level in the second panel of Figure 4. The upper 700 m is stretched relative to the deeper ocean, thus highlighting the upper ocean trends. The deep ocean portion extends from 700 m to 6000 m. Tick marks in the upper ocean are set 100 m apart, whereas those in the deeper ocean are 800 m apart. The horizontal axis has tick marks every two years from 1993-2007.

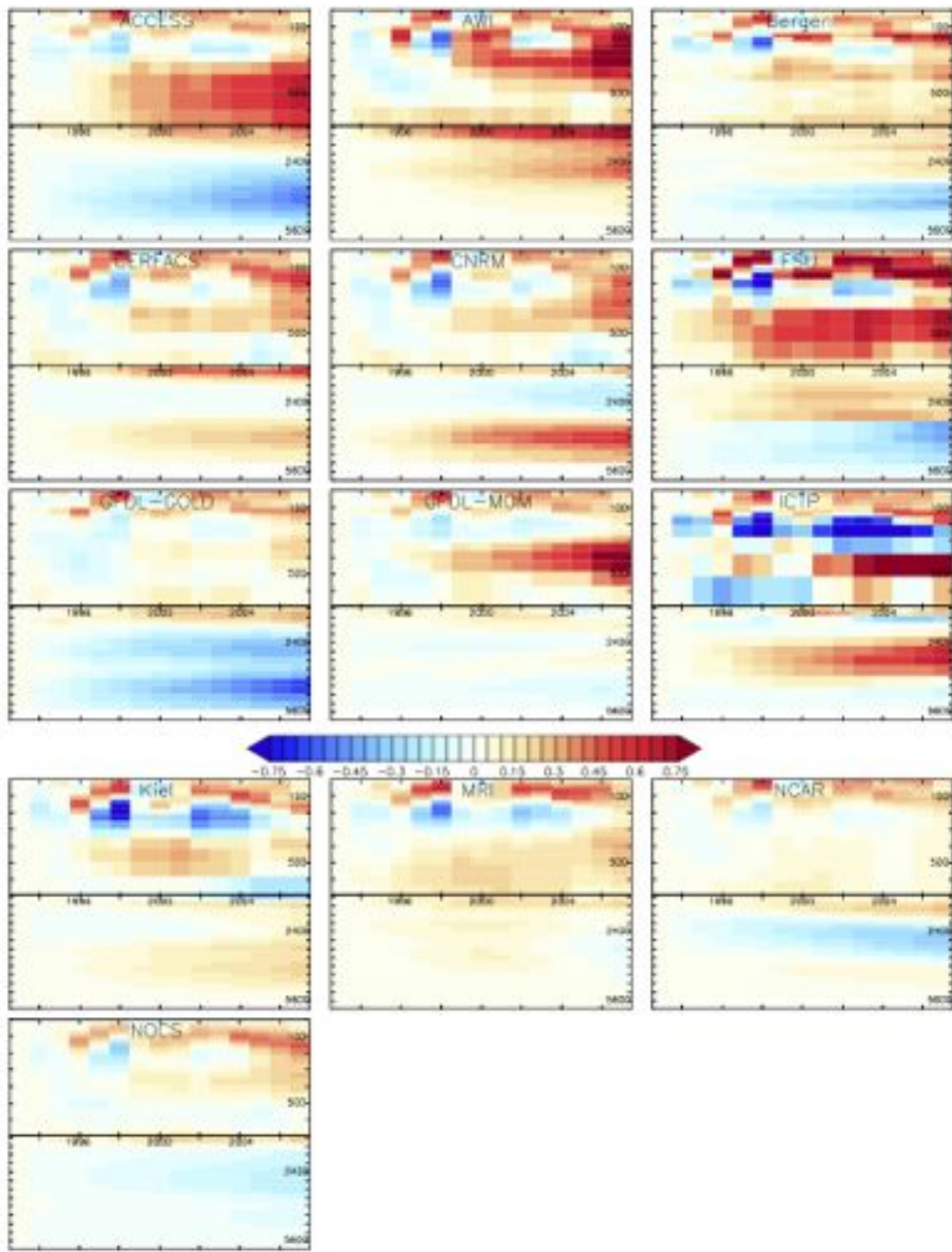


Figure 6: Time series for the horizontally integrated annual mean contributions to thermosteric sea level as a function of depth (in metres), during the years 1993-2007 of the fifth CORE-II cycle. The units are millimetres. The vertical sum yields approximately the time series for the global mean steric sea level in the second panel of Figure 4. The upper 700 m is stretched relative to the deeper ocean, thus highlighting the upper ocean trends. The horizontal axis has tick marks every two years from 1993-2007.

793 simulations for the years 1993 to 2007, though with most simulations exhibiting an upward trend
794 at the lower end of the observation-based trend of 0.6 – 1.2 cm.

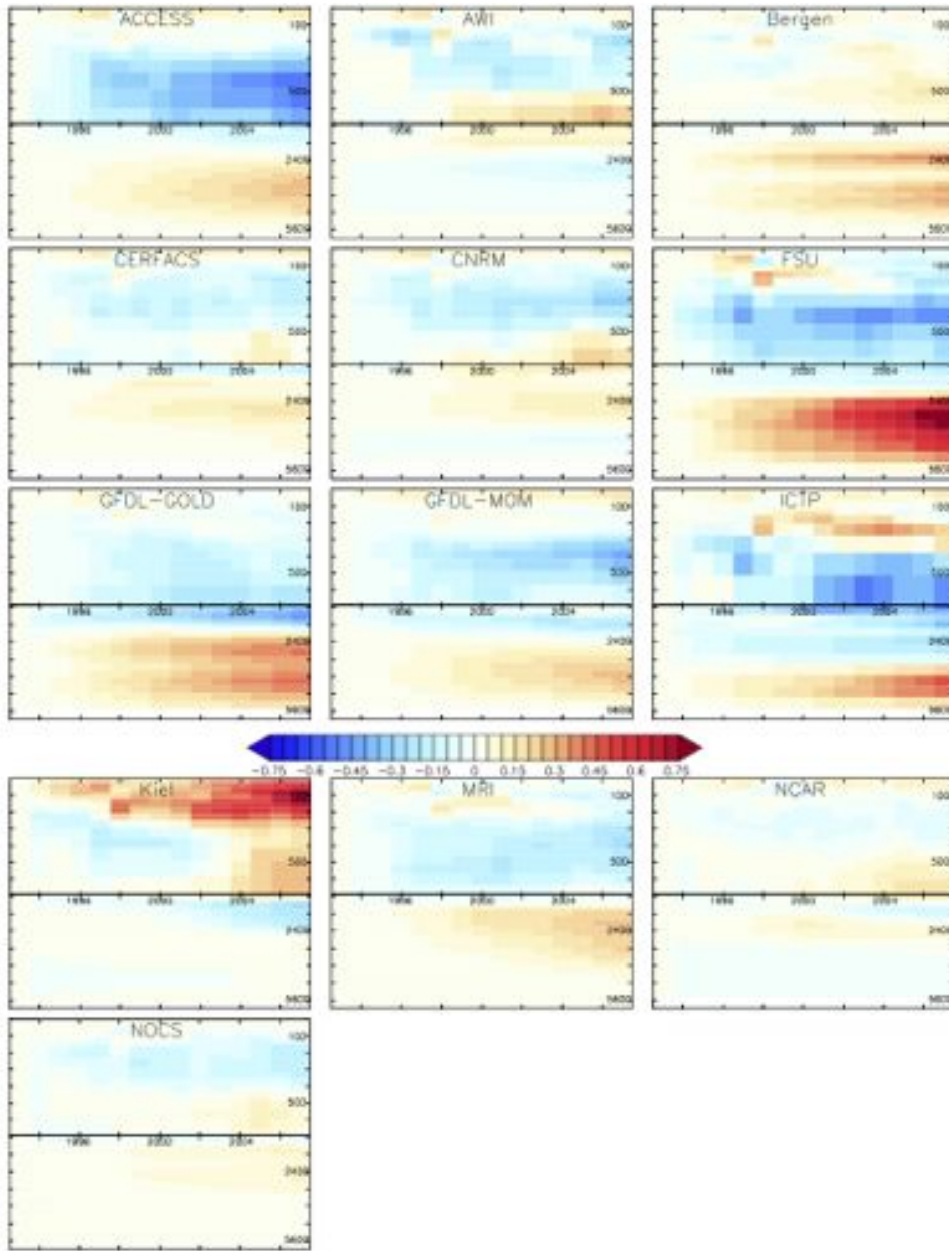


Figure 7: Time series for the horizontally integrated annual mean contributions to halosteric sea level as a function of depth (in metres), during the years 1993-2007 of the fifth CORE-II cycle. The units are in millimetres. The vertical sum is negligible compared to the vertical sum of the thermosteric contributions in Figure 6, thus indicating the dominance for global mean sea level of the thermosteric effects. However, over certain depth ranges, halosteric effects can be important for some of the models. The upper 700 m is stretched relative to the deeper ocean, thus highlighting the upper ocean trends. The horizontal axis has tick marks every two years from 1993-2007.

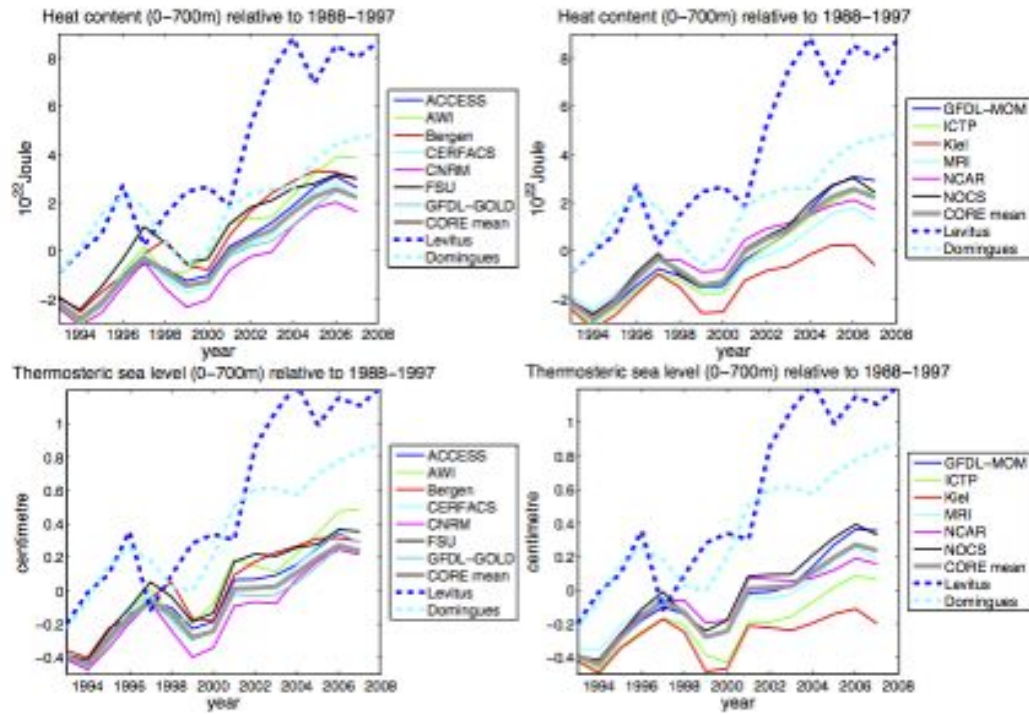


Figure 8: Time series for ocean heat content and thermosteric sea level integrated in the upper 700 m of ocean. To reduce dependence on a single chosen reference date, each result is computed with respect to the ten year mean for the respective model or observational time series, and we chose years 1988–1997. The CORE-II ensemble mean is also shown, as computed from all of the simulations. We also show estimates from observations based on analysis of Levitus et al. (2012) and Domingues et al. (2008). Model results are global, and correspond to the sum from roughly the upper 700 m in the vertical-time plots shown in Figure 6. Note that if we remove a linear trend, variability in the CORE-II simulations are closer in agreement to Domingues et al. (2008) than Levitus et al. (2012). In Section 2.6, we discuss the slower increase in heating within the CORE-II simulations relative to observations.

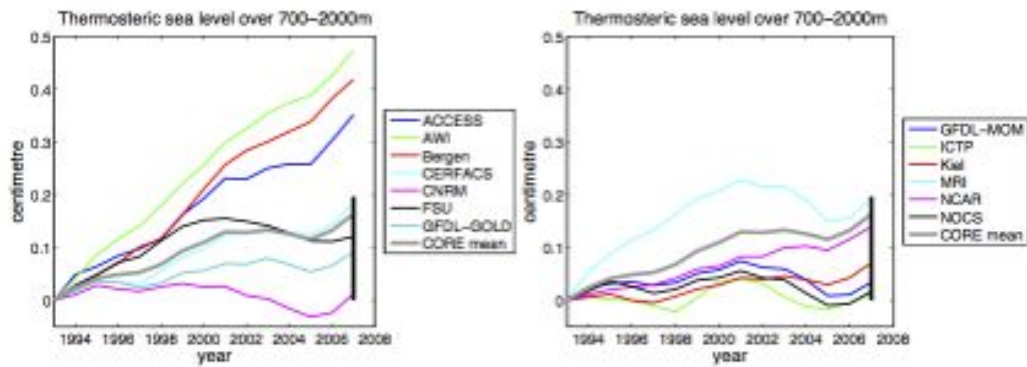


Figure 9: Time series for the thermosteric sea level computed from the depth range 700-2000 m. The CORE-II ensemble mean is shown as computed from all of the simulations. The solid black vertical line at year 2007 represents an estimate of the spread in the observational estimates at the end of the 15 years, computed using a trend of $0.1 \pm 0.1 \text{ mm yr}^{-1}$ for 700-2000 m (Section 3.5). Each time series is computed relative to the respective model's steric sea level at 1993.

795 4. Temperature and heat content trends for 1993-2007

796 Global sea level change in the CORE-II simulations is directly correlated to the change in
797 ocean heat content, with the global mean temperature shown in Figure 3 directly related to the
798 net heat flux entering the ocean through its boundaries (equation (40) in Appendix A4). We thus
799 find it useful to consider the heat fluxes and ocean heat content and temperature trends seen in
800 the CORE-II simulations. Following the discussion in Sections 2.6 and 2.7, we consider the
801 period 1993-2007 in the fifth CORE-II cycle.

802 4.1. Boundary heat fluxes

803 Figure 10 shows the time mean boundary heat flux computed over years 1993-2007 for the
804 CORE-II simulations. These patterns include the shortwave, longwave, latent, and sensible heat
805 flux passing across the ocean surface, as well as geothermal heating in those models where it is
806 included (Table 1). Additionally, the heat flux due to water transport across the ocean surface is
807 included for those models employing a real water flux (Table 1), with this heat flux detailed in
808 Section A4. Finally, there is an adjustment of the heat flux associated with frazil ice formation.

809 All models exhibit heating in the tropics, which is where global mean sea level is affected
810 the most from surface heating due to the relatively large tropical thermal expansion coefficient
811 (Figure 1). All models also show a heat loss in western boundary currents due to the sensible and
812 latent heat loss arising from generally warm waters under a cooler atmosphere. The subpolar
813 North Atlantic is a region where the models generally experience surface heat loss, though with
814 all models except ICTP exhibiting heat gain near Newfoundland, and with the FSU-HYCOM
815 simulation losing far less surface heat than the other simulations. Deviations between the models
816 largely reflect the paths of the Gulf Stream and North Atlantic Current. Such differences are also
817 reflected in coupled climate models contributing to CMIP (Yin et al., 2010a; Pardaens et al.,
818 2011b; Yin, 2012; Slangen et al., 2012; Bouttes et al., 2013).

819 The global mean of the ocean boundary heat flux during years 1993-2007 is indicated on
820 each panel of Figure 10. There are rather large differences in heat flux regionally, particularly
821 in the high latitudes. In general, differences in heat flux illustrate that although the CORE-II
822 simulations use the same atmospheric state, they do not necessarily realize the same heat flux
823 due to differences in simulated ocean and sea ice states. Many models have a net heat flux in the
824 range $0.2 - 0.6 \text{ W m}^{-2}$, though the AWI-FESOM model exhibits a larger heat flux of roughly
825 1 W m^{-2} and GFDL-GOLD and NOCS show a near zero mean boundary heat flux. The FSU-
826 HYCOM simulation shows a negative surface heat flux of roughly -0.7 W m^{-2} . However, global
827 mean sea level in the FSU-HYCOM simulation is rising slightly during the period 1993-2007
828 (see Figure 4), with the rise due to the spurious numerical heat source on the order of 1 W m^{-2}
829 (Appendix C and Table 1).

830 Figure 11 shows the time series for the running sum of the global mean annual ocean heat
831 flux for the years 1993-2007. The running sum measures how much heat accumulates within
832 the ocean relative to the start of the integration. All models, except FSU-HYCOM, agree that
833 surface fluxes are adding heat globally to the ocean during the period 1993-2007.

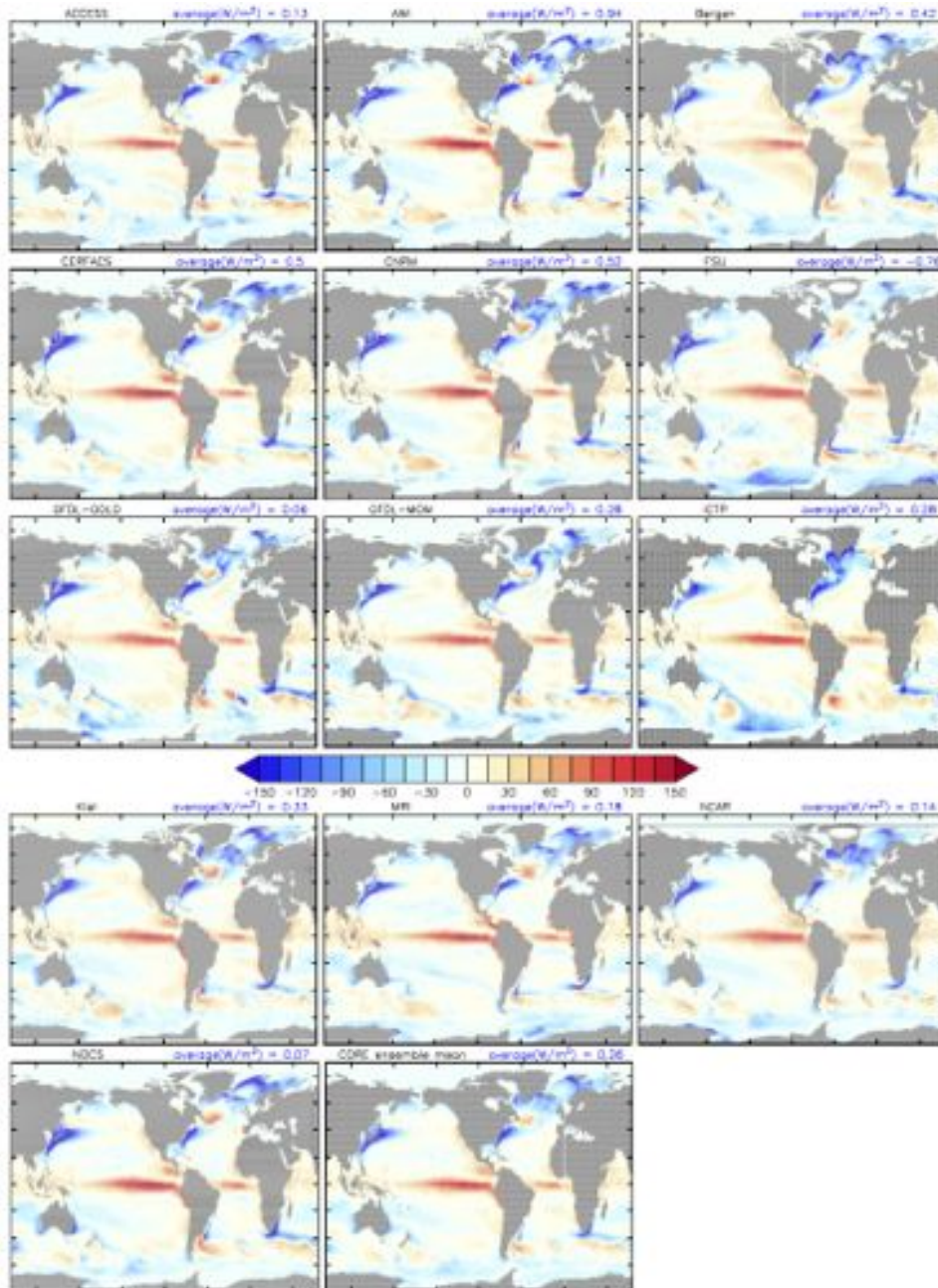


Figure 10: Boundary ocean heat fluxes (units W m^{-2}) for the years 1993-2007 as computed from the fifth CORE-II cycle. A positive number represents heat going into the ocean. The time mean heat flux over this period is indicated on the title to each panel. Also note the simulations from GFDL-GOLD, GFDL-MOM, and ICTP include a geothermal heat flux, with a global ocean mean of 0.06 W m^{-2} ; the CERFACS and CNRM simulations include a geothermal heat flux with a global ocean mean of 0.084 W m^{-2} . Land masking is set according to the respective model land-sea masks.

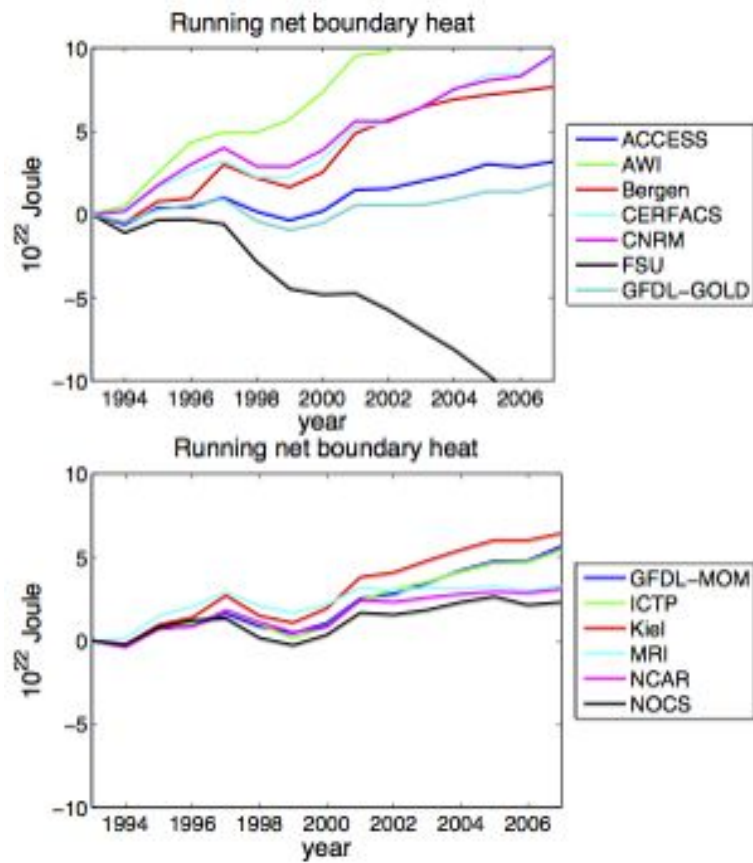


Figure 11: Time series for the running global integrated heat entering the ocean for the CORE-II simulations, relative to 1993 in the fifth CORE-II cycle. Note that all simulations, except that from FSU-HYCOM, exhibit an upward trend in heat accumulation.

834 *4.2. Ocean heat content trends*

835 Figure 12 shows the linear trend in full-depth integrated ocean heat content, per unit ocean
 836 horizontal area, over the years 1993-2007. We compute this diagnostic according to

$$\frac{\Delta \mathcal{H}}{\Delta t} = \rho_o C_p \sum_z \left(\frac{\partial \Theta}{\partial t} \right) dz \quad \text{W m}^{-2}, \quad (11)$$

837 where the tendency $\partial \Theta / \partial t$ is approximated by computing the slope of a line fit to the annual
 838 mean temperature over the years 1993-2007. Because of the vertical weighting, a relatively
 839 small change in the deep ocean temperature can correspond to sizable changes in heat content.
 840 We also show the vertically integrated heat content trend, per unit ocean horizontal area, over
 841 just the upper 700 m of water in Figure 13, with this depth range allowing us to compare to
 842 three observation-based analyses. Finally, the trend in zonally averaged temperature is shown in
 843 Figure 14, which reveals the vertical and meridional extent of temperature changes. The zonal
 844 mean trends reveal that much of the trend in the high latitude occurs below 700 m.

845 We use three observation-based analyses in Figure 13 to help expose uncertainties in com-
 846 parison to the CORE-II simulations, and offer the following comments regarding these three
 847 analyses.

- 848 • Domingues et al. (2008) and Levitus et al. (2012) generally agree in the low and middle
 849 latitudes of all ocean basins, with warming in the west Pacific the dominant pattern of
 850 change. Moving southward, the Domingues et al. (2008) analysis shows broad regions
 851 of cooling in the northern flank of the Antarctic Circumpolar Current, whereas Levitus
 852 et al. (2012) has a much smaller signal. Cooling in the Southern Ocean is seen in the
 853 Durack and Wijffels (2010) analysis, reflective of that seen by Domingues et al. (2008) in
 854 the Pacific sector but not the Atlantic. We caveat the Southern Ocean observation-based
 855 estimates by noting that this is the most sparsely sampled region of the World Ocean.
- 856 • In the North Atlantic, Levitus et al. (2012) shows a sizable warming in the subpolar region,
 857 and slight cooling to the south along the Gulf Stream region. This warm-north / cold-south
 858 pattern has been analyzed in several studies, such as Häkkinen (2000) and Esselborn and
 859 Eden (2001) and recently by Yin and Goddard (2013), with this pattern associated with
 860 fluctuations in the Atlantic meridional overturning circulation. We comment more on this
 861 pattern in Section 5.5. In contrast to this distinct Atlantic signal in the Levitus et al. (2012)
 862 analysis, Domingues et al. (2008) picks up very little signal. Durack and Wijffels (2010)
 863 capture a warming in the subpolar North Atlantic, though more confined to the Labrador
 864 Sea compared to Levitus et al. (2012), and a weaker cooling than Levitus et al. (2012)
 865 within the Gulf Stream region.
- 866 • As compared to Domingues et al. (2008) and Levitus et al. (2012), the Durack and Wijffels
 867 (2010) analysis exhibits larger warm anomalies in the west Pacific and cold anomalies in
 868 the east, with the cold anomalies having an El Niño Southern Oscillation (ENSO) signa-
 869 ture largely absent from Domingues et al. (2008) and Levitus et al. (2012). To support this
 870 connection to ENSO, we considered a modified analysis based on Durack and Wijffels
 871 (2010) that includes a filter to remove the ENSO signal. This filtered pattern (not shown)

872 in fact diminishes the amplitude of the Pacific heating trend in Figure 13, thus suggesting
873 that ENSO is a key contributor.

874 In general, the CORE-II ensemble mean shows a low and middle latitude warming roughly
875 consistent, though larger, with the observation-based analyses. Models agree that heat is ac-
876 cumulating in the subpolar North Atlantic, with heat accumulating even in the abyssal regions
877 (Figure 14). This warming is reflected also in the Levitus et al. (2012) estimate, and to a lesser
878 extent in Durack and Wijffels (2010), yet largely absent from Domingues et al. (2008).

879 In the 1980s and early 1990s, the North Atlantic Oscillation (NAO) exhibited a persistent
880 positive phase and the associated large negative surface fluxes acted as a pre-conditioner for an
881 enhanced Atlantic meridional overturning circulation (AMOC). During this period, enhanced
882 poleward oceanic heat transport associated with an enhanced AMOC was largely balanced by
883 surface cooling due to the positive NAO. Around 1995/1996, a reduction in the surface ocean
884 heat loss associated with a change in the NAO to its negative (or neutral) phase allowed for the
885 northward oceanic heat transport to cause the subpolar gyre to transition to an anomalously warm
886 phase. See Esselborn and Eden (2001) for attribution of 1990s sea level variability to redistribu-
887 tion of upper-ocean heat content associated with a fast dynamical response of the circulation to
888 a drop in the NAO index. Further details can be found in Lohmann et al. (2009), Robson et al.
889 (2012), Yeager et al. (2012) and Danabasoglu et al. (2014). This behaviour highlights that much
890 of the Atlantic trend shown over this period is related to natural variability, with this point also
891 emphasized by Large and Yeager (2012). We also note that the dipole pattern of warm-north /
892 cold-south within the North Atlantic, recently analyzed by Yin and Goddard (2013), is indeed
893 reflected in the CORE ensemble mean (see Section 5.5 for more discussion).

894 Most models indicate a net cooling over the central and eastern tropical Pacific reflecting an
895 ENSO-like pattern (as in the Durack and Wijffels (2010) analysis); a general pattern of warming
896 in the equatorial flank of the Southern Ocean and cooling to the poleward flank; and a general
897 warming for the Kuroshio region of the northwest Pacific (Figure 12 and 13). For regions outside
898 the strong trends in the North Atlantic, the zonal mean trends shown in Figure 14 indicate some
899 variety in the upper ocean warming, largely in the middle to lower latitudes. There is a slight
900 cooling seen around $20^{\circ} - 30^{\circ}N$ in the upper ocean, and cooling in the abyssal Southern Ocean
901 in many models. The deep Southern Ocean cooling trend may be indicative of a model drift
902 that does not correspond to the estimated observed warming trends discussed by Purkey and
903 Johnson (2010). It may also indicate a problem with the CORE-II atmospheric state, perhaps
904 with too cold air temperatures inducing deep cooling, despite the corrections detailed in Large
905 and Yeager (2009).

906 The broad qualitative agreement between the CORE-II simulations and observation-based
907 analyses indicates some skill in the CORE-II simulations to capture patterns of observed trends
908 in upper 700 m heat content. Certainly there are regions of differences. But given uncertainty
909 in the observation-based analysis, and the wide range of model formulations considered in the
910 CORE-II suite, we are generally pleased with the agreement. Furthermore, the agreement adds
911 confidence to both the observation-based analyses and to the CORE-II simulations.

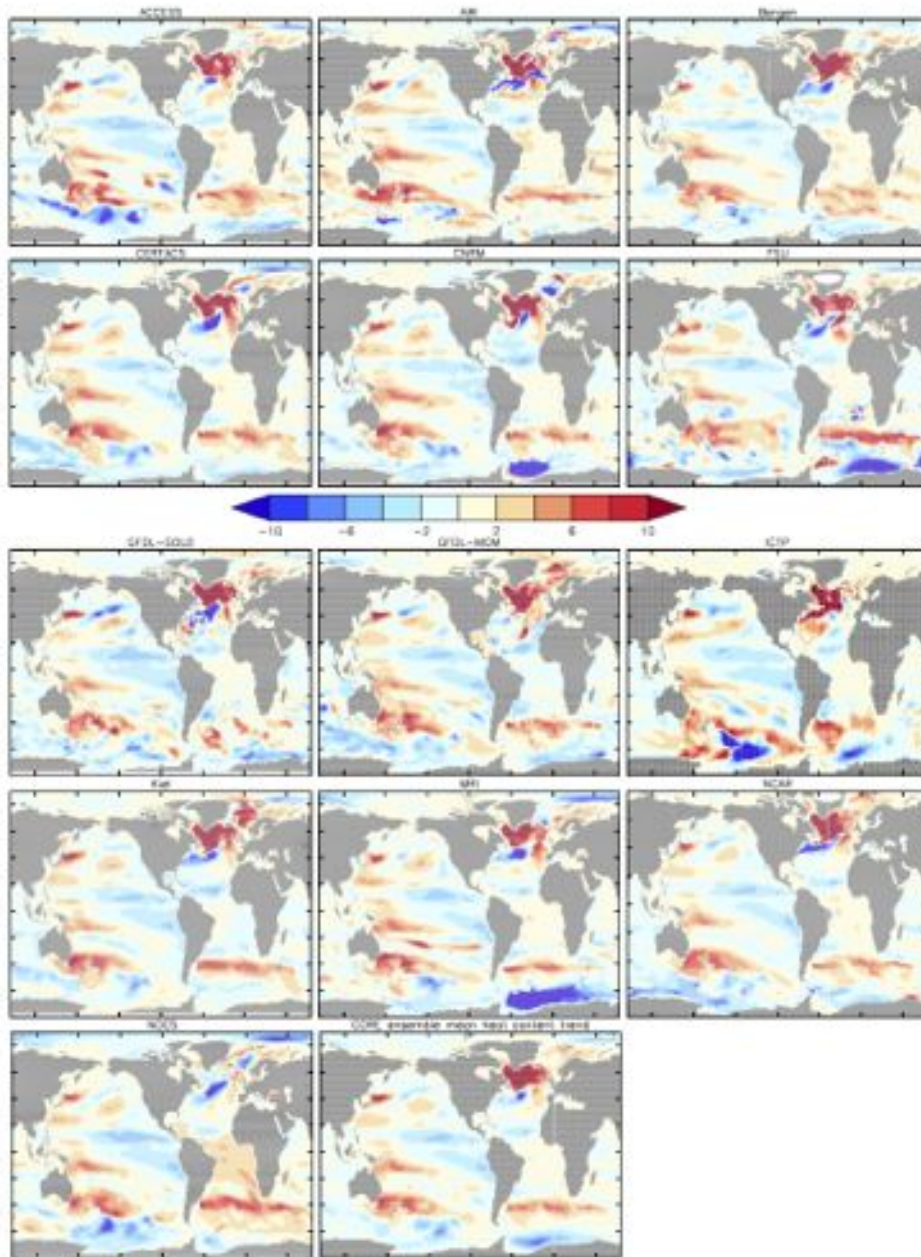


Figure 12: Linear trend in depth integrated annual mean ocean heat content (units W m^{-2}) for the years 1993-2007 as computed from the fifth CORE-II cycle. Note that most models exhibit a relatively strong warming in the subpolar North Atlantic (the NOCS model is a notable exception); a warming in the Kuroshio extension of the Pacific; warming in the mode water regions of the Southern Hemisphere centred around 40°S ; and cooling in the eastern central Pacific. Most models show a negligible trend in both the Arctic Ocean and Indian Ocean. Some show a strong cooling trend in the Weddell Sea and Ross Sea sectors of the Southern Ocean. The colour bar range is chosen to match that shown in Figure 13 for the upper 700 m heat trends.

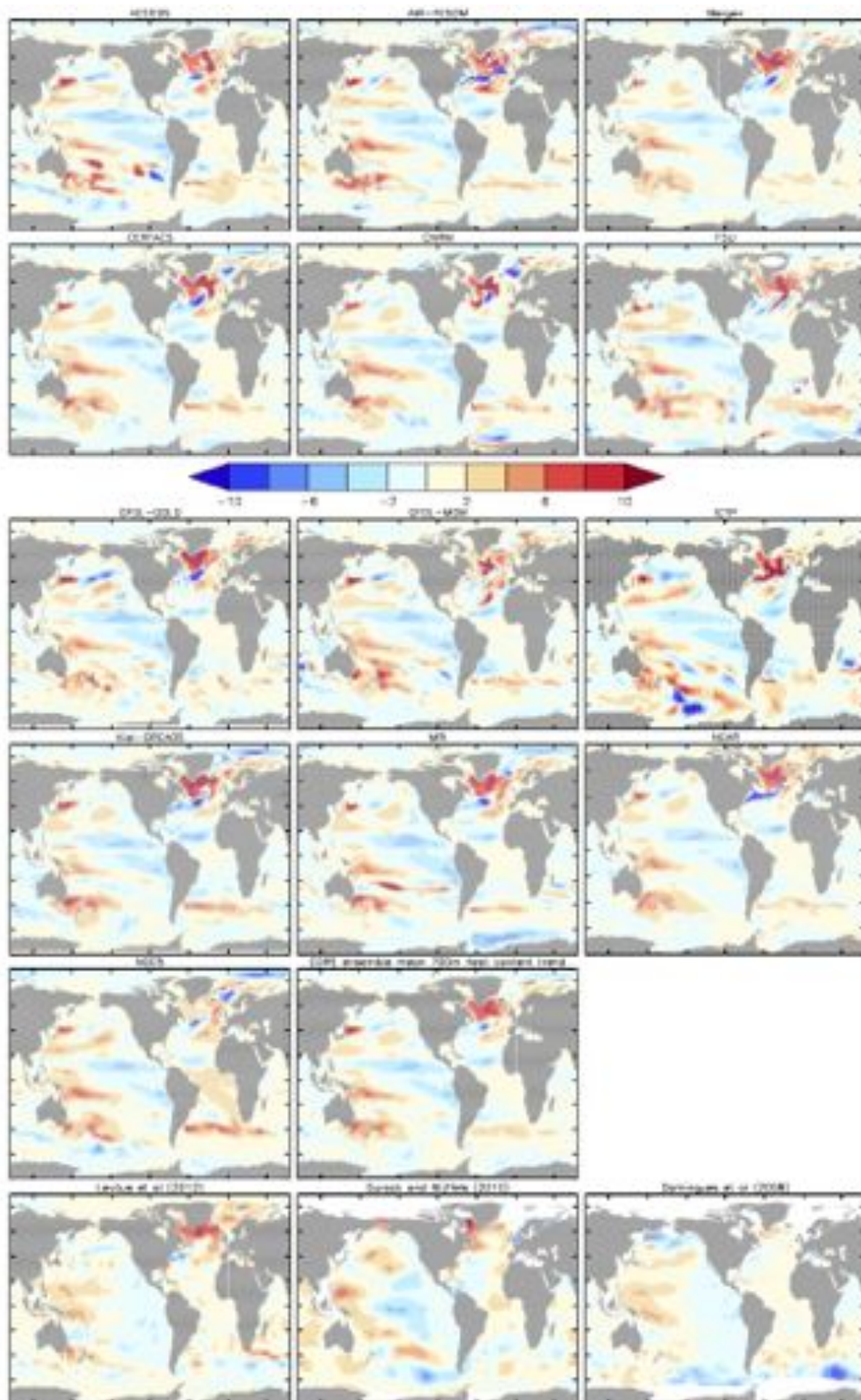


Figure 13: Linear trend in annual mean ocean heat content vertically integrated over the upper 700 m of ocean (units $W m^{-2}$) for the years 1993-2007, computed from the fifth CORE-II cycle. Also shown is the corresponding trend over years 1993-2007 from Levitus et al. (2012) analysis; an updated analysis from Domingues et al. (2008) and Church et al. (2010) (see their Figure 6.3b); and the trend over years 1990-2010 using an updated version of the Durack and Wijffels (2010) analysis. Note that much of the high latitude trend seen in Figures 12 and 14 is missing here, since those trends occur in regions deeper than 700 m. The models also generally show some cooling in the west/central Pacific, with this cooling absent from the observation-based analyses. The spatial correlation between the CORE ensemble mean and the observation-based analyses is given by CORE-Levitus=0.44, CORE-Domingues=0.34, CORE-Durack=0.29, where the correlation is computed as $corr(A,B) = \frac{\int AB dx dy}{\left(\int A^2 dx dy\right)^{1/2} \left(\int B^2 dx dy\right)^{1/2}}$, and we ignore regions where the observation-based analyses are missing.

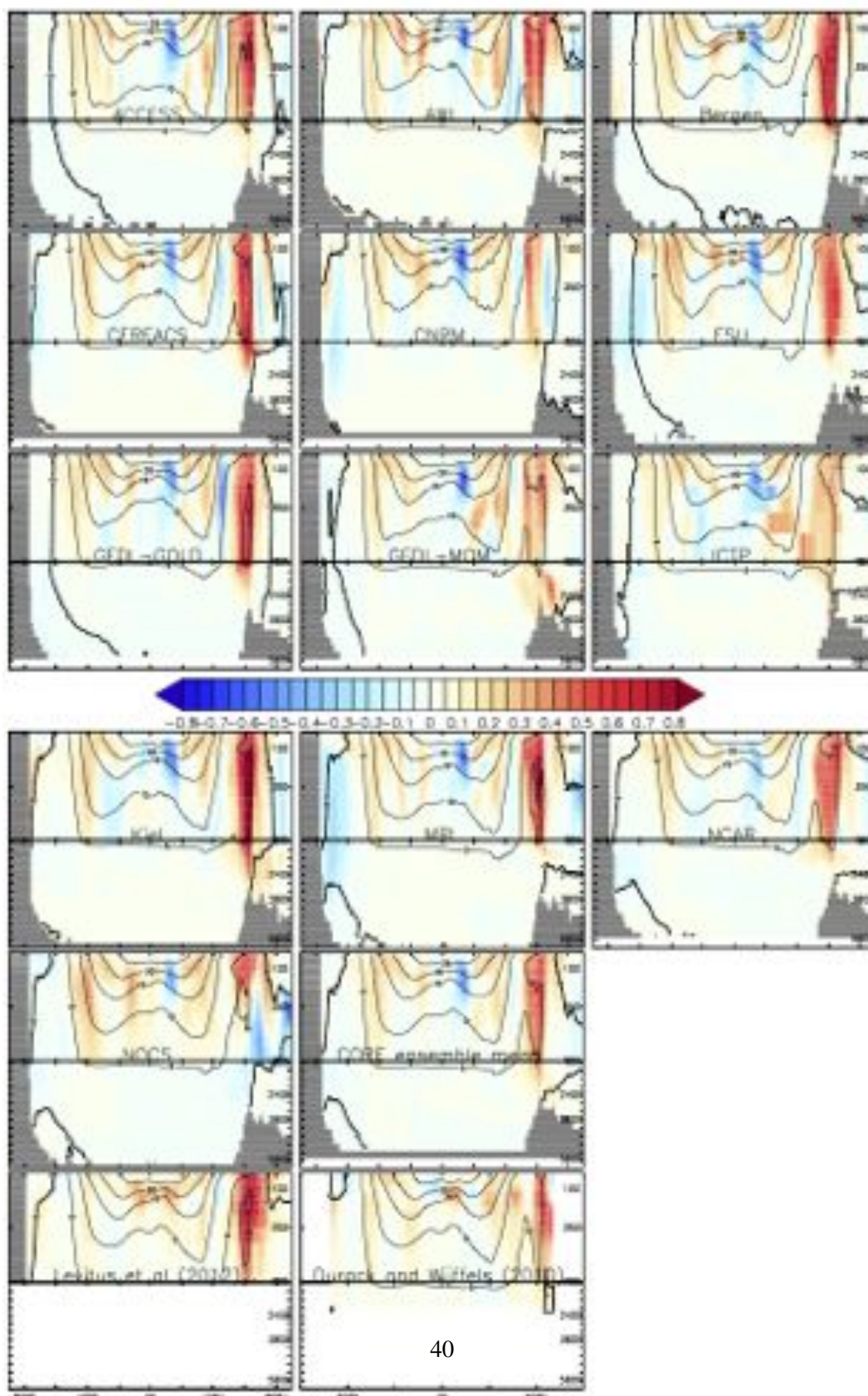


Figure 14: Zonal average of the linear trend in annual mean ocean temperature (deg C decade^{-1}) for the years 1993-2007 as computed from the fifth CORE-II cycle. Also shown are two estimates of the observation-based trends. Overlaying the trends are contours for the time mean temperature computed from each respective model and observation-based analysis. The upper 700 m of the ocean is split from the deeper ocean to emphasize changes in the upper ocean. The images are computed by first mapping the 3d model results to a common spherical grid with a common vertical spacing, and then performing the zonal average.

912 **5. Dynamic sea level during 1993-2007**

913 In Figure 15, we present the time mean of the dynamic sea level (equation (5)) over years
 914 1993-2007 for the CORE-II simulations, as well as the dynamic sea level from the gridded
 915 satellite altimeter product from the AVISO project (Archiving, Validation, and Interpolation of
 916 Satellite Oceanographic) (Le Traon et al., 1998; Ducet et al., 2000). Recall from the definition
 917 in equation (5), the DSL has a zero global area mean. Figure 16 shows the anomalies (model
 918 minus satellite), with model results mapped to the same spherical grid as the satellite analysis.
 919 The root-mean-square difference over the satellite region is computed according to

$$\text{RMS} = \sqrt{\frac{\int dA (\zeta - \zeta^{\text{obs}})^2}{\int dA}}, \quad (12)$$

920 with dA the area of a grid cell and ζ^{obs} the dynamic sea level from AVISO. The numbers are
 921 given in Table 2. The models cluster around a global error between 0.09 – 0.15 m. The ensemble
 922 mean has a smaller difference than any of the models, except for CERFACS and NOCS.

923 Figure 17 shows the zonal mean of the RMS difference for the dynamic sea level in the
 924 models relative to AVISO, including the zonal mean of the difference for the ensemble mean.
 925 Note how the models generally are more consistent with observations in the lower latitudes,
 926 with the high latitudes leading to largest errors, particularly in regions of mode and deep water
 927 formation (poleward of 40 degrees latitude) as well as western boundary currents in the Atlantic
 928 and Pacific (see the difference maps in Figure 16). Differences in simulated high latitude sea
 929 ice may also contribute to model differences from the satellite measures.³ The north-south gra-
 930 dient of dynamic sea level across the Southern Ocean is weaker for many of the simulations
 931 relative to AVISO, perhaps suggesting a weaker than observed zonal transport in the Antarctic
 932 Circumpolar Current or a latitudinal shift in the models. The positive anomalies in the tropical
 933 Pacific, extending eastward from the warmpool region, may be a result of wind errors, as sug-
 934 gested when running the CERFACS model using the ECMWF-reanalysis based Drakkar forcing
 935 from Brodeau et al. (2010) (Christophe Cassou, personal communication, 2013). In general, we
 936 conclude that each of the CORE-II simulations produces a respectable 1993-2007 time mean
 937 dynamic sea level, meeting or surpassing the accuracy of the historical simulations considered
 938 as part of the CMIP3 analysis of Yin et al. (2010a).

939 In the remainder of this section, we present linear trends in dynamic sea level and associated
 940 steric and bottom pressure patterns computed over years 1993-2007 during the 5th CORE-II
 941 cycle. Note that for all figures in this section, we first subtract the global area mean of a chosen
 942 pattern for each year (to reveal the dynamic sea level as defined by equation (5)), and then
 943 compute the linear trend for the anomalous patterns.

944 *5.1. Description of dynamic sea level (DSL) trends*

945 Figure 18 shows the linear trend in annual mean dynamic sea level for years 1993-2007 in
 946 the CORE-II simulations, as well as the satellite measured sea level trend of the AVISO analysis.

³A detailed analysis of the freshwater budget and sea ice over the Arctic Ocean in the CORE-II simulations will be presented in a companion paper focusing on the Arctic region (Qiang Wang, personal communication 2013).

MODEL	RMS DIFF FOR MEAN DSL (metre)	RMS DIFF FOR LINEAR TREND DSL (mm yr ⁻¹)
ACCESS	0.11	3.0
AWI-FESOM	0.12	3.2
Bergen	0.12	2.6
CERFACS	0.10	2.8
CNRM	0.11	2.9
GFDL-GOLD	0.12	2.8
GFDL-MOM	0.12	3.0
FSU-HYCOM	0.12	3.5
ICTP	0.15	3.1
Kiel-ORCA05	0.10	3.1
MRI	0.13	3.1
NCAR	0.12	2.8
NOCS	0.09	2.7
CORE-II ensemble mean	0.10	2.6

Table 2: Root-mean-square difference (metre) between the time mean (1993-2007) dynamic sea level from the CORE-II simulations and the JPL/AVISO satellite product over the same years (see Figure 15 for the horizontal patterns). Also shown is the RMS difference (mm yr⁻¹) between the DSL linear trend over years 1993-2007 in the CORE-II relative to the JPL/AVISO analysis (see Figure 18 for the horizontal patterns). The statistics were computed over the satellite region, which is roughly within the latitude band 60°N – 60°S. Each model result is remapped to the one-degree spherical grid defined by the JPL/AVISO grid in order to compute pattern differences.

947 Table 2 provides a root-mean-square difference between the models and AVISO within the satel-
948 lite region. The observed DSL trend shows positive values in the western Pacific and the North
949 Atlantic subpolar gyre, and negative values in the eastern and North Pacific as well as the Gulf
950 Stream region. There is also a notable positive trend in the Southern Ocean south of Australia
951 extending from the east Indian sector into the west Pacific sector. Adding the global sea level rise
952 of 3.1mm yr⁻¹ since 1993 increases/decreases the area and magnitude of the positive/negative
953 sea level trends. In particular, the total sea level trend in the western Pacific since 1993 has been
954 up to 10 mm yr⁻¹, at least three times faster than the global mean, whereas sea level in the eastern
955 Pacific has depressed. The Pacific pattern is likely dominated by inter-decadal variability and
956 is closely related to the Pacific Decadal Oscillation (Feng et al., 2010; Bromirski et al., 2011;
957 Merrifield et al., 2012; McGregor et al., 2012; Zhang and Church, 2012). We further discuss
958 the Pacific patterns in Section 5.6. Similarly, the pattern in the North Atlantic mainly reflects
959 decadal to multi-decadal time scale variability as impacted by the North Atlantic Oscillation
960 (Häkkinen and Rhines, 2004; Lohmann et al., 2009; Yeager et al., 2012; Danabasoglu et al.,
961 2014).

962 Determining whether long-term DSL trends exist in the Pacific and Atlantic basins is difficult
963 due to the relatively short satellite records (Zhang and Church, 2012; Meyssignac et al., 2012).
964 In the Atlantic subpolar gyre and eastern North Atlantic, it takes about 20-30 years for a decadal
965 sea level trend to rise above variability associated with high-frequency wind-driven and eddy
966 generated processes (Lorbacher et al., 2010). Kopp (2013) suggests that long-term trends in sea
967 level along the eastern US coast is only a recent occurrence, with no detectable trends in this
968 region prior to 1980. Köhl and Stammer (2008), following Roemmich et al. (2007), suggest that
969 much of the rise in dynamic sea level within the South Pacific subtropical gyres is associated
970 with atmospheric decadal variability modes impacting the wind stress curl.

971 The simulations generally show positive/negative values in the western/eastern Pacific DSL

972 trends, with structures comparing reasonably well to observations. However, most models sim-
 973 ulate a strong negative centre at 135° W, 15° N, with the magnitude stronger than in the obser-
 974 vations. Also, the models generally show a decreasing trend in the Southern Ocean south of
 975 Australia, which is opposite to the positive trend found in the satellite analysis.

976 To varying degrees, the simulations and observations show a rise of the DSL south of Green-
 977 land. This rise in the models reflects the increased heat content in this region, as shown in Figures
 978 12 and 14. This heat content increase is associated with a recent spin-down of the subpolar gyre
 979 by decreased surface cooling in this region (Häkkinen and Rhines, 2004), whilst the northward
 980 meridional heat transport coming from the south is still high (Lohmann et al., 2009; Yeager et al.,
 981 2012; Danabasoglu et al., 2014).

982 In the Arctic ocean, where no satellite sea level measurements are available, most models
 983 simulate a significant rise of the DSL, especially in the Beaufort gyre region, and a lowering in
 984 the Canadian Archipelago and around Greenland. As shown in Figure 23 discussed in Section
 985 5.3, these changes are associated with halosteric effects. The rise in sea level north of Eurasia is
 986 associated with reductions in sea ice cover (e.g., Laxon et al., 2013), and increases in Eurasian
 987 river discharge (e.g., Peterson et al., 2002; Rabe et al., 2011). The lowering of DSL in the
 988 Canadian Archipelago and around Greenland is associated with the increased salt content in
 989 regions impacted by the North Atlantic, where the changes in meridional transport are advecting
 990 more salt into this region.

991 In addition to the above regional trends, there are changes in the tropical Indian and Atlantic
 992 oceans and the South Atlantic, with CORE-II simulations and observations agreeing that the
 993 trends are small. Moving further south, the Southern Ocean mode water regions around 40°S –
 994 50°S generally show an increasing sea level trend, with AVISO also showing such a trend,
 995 though somewhat smaller than some of the models. The trend may be related to the southward
 996 shift of the westerlies (Yin, 2005; Yin et al., 2010a).

997 5.2. Sea level trends decomposed into mass and local steric effects

998 Tendencies in sea level can be decomposed into tendencies from mass and local steric
 999 changes. It has proven useful in various studies to perform this decomposition (e.g., Lowe and
 1000 Gregory, 2006; Landerer et al., 2007b; Yin et al., 2009, 2010a; Pardaens et al., 2011a). For a
 1001 hydrostatic fluid, this decomposition is written (see equation (47) in Appendix B1)

$$\underbrace{\frac{\partial \eta}{\partial t}}_{\text{sea level tendency}} = \underbrace{\frac{1}{g \rho_o} \left(\frac{\partial (p_b - p_a)}{\partial t} \right)}_{\text{mass tendency}} - \underbrace{\frac{1}{\rho_o} \left(\int_{-H}^{\eta} \frac{\partial \rho}{\partial t} dz \right)}_{\text{local steric tendency}}. \quad (13)$$

1002 This expression was introduced by Gill and Niiler (1973) for their analysis of observed steric
 1003 changes over a seasonal cycle. The first term on the right hand side exposes those changes to sea
 1004 level due to changes in the mass of fluid in an ocean column. As mass increases within a column,
 1005 either through the movement of mass within the ocean, changes to the mass crossing the ocean
 1006 boundary, or changes to the atmospheric pressure loading, the bottom pressure in turn increases
 1007 and sea level also increases. We note that for the CORE-II simulations, changes associated
 1008 with atmospheric loading are ignored, as all models impose a zero weight atmosphere on the

1009 ocean for purposes of driving ocean dynamics (see Appendix C5 in Griffies et al. (2009b)). The
 1010 second term in equation (13) arises from local steric changes, in which decreasing density (as
 1011 through warming) expands an ocean column and so raises sea level. As stated earlier, we are
 1012 focused here on pattern changes, so differences in global means are removed, thus making our
 1013 application of equation (13) equivalent for both Boussinesq and non-Boussinesq fluids.

1014 Figure 19 exposes the linear trend in steric sea level (second term on right hand side of
 1015 equation (13)), and Figure 20 shows the trend in bottom pressure (first term on right hand side
 1016 of equation (13)). Comparison to Figure 18 indicates that the majority of the sea level trend
 1017 is associated with steric changes. We thus have more to say regarding steric trends, including
 1018 thermosteric and halosteric trends, in subsequent subsections.

1019 The bottom pressure trends are largely localized to the Arctic regions, as well as certain shelf
 1020 regions, with the shelf patterns more visible when choosing a smaller range for the colour bar
 1021 as shown in Figure 21. Landerer et al. (2007a,b), Yin et al. (2009), and Yin et al. (2010a) in-
 1022 terpreted projections in the late 21st century of increased bottom pressure loading along shelves
 1023 and marginal seas as arising from the tendency for deeper waters to expand more, thus creating
 1024 a steric gradient moving mass towards the coast (see also Appendix B1). The redistribution of
 1025 ocean mass from the ocean interior towards the shallower shelf region is evident for the CORE-II
 1026 simulations especially in the Arctic, given that the Arctic is the shallowest of the World Ocean
 1027 basins. Indeed, as noted by Landerer et al. (2007a), there is a general movement of ocean mass
 1028 from the Southern Hemisphere to the Northern Hemisphere, which is reflected in the ensemble
 1029 mean of the CORE-II simulations in Figure 20. One exception is the region surrounding the
 1030 Bering Strait and adjacent Siberian shelf region.

MODEL	BOTT PRESS	STERIC (700 M)	THERMOSTERIC (700 M)	HALOSTERIC (700 M)	CORRELATE THERMO/HALO
ACCESS	0.48	1.53 (1.5)	2.2 (2.1)	1.4 (1.3)	-0.42
AWI	0.40	1.8 (1.56)	2.6 (2.3)	1.6 (1.4)	-0.28
Bergen	0.42	0.96 (0.86)	1.6 (1.3)	1.3 (0.92)	-0.36
CERFACS	0.36	1.0 (0.85)	1.7 (1.2)	1.3 (0.93)	-0.32
CNRM	0.51	2.2 (1.5)	2.7 (1.9)	1.6 (1.5)	-0.29
FSU	0.75	1.7 (1.3)	2.5 (1.9)	1.5 (1.2)	-0.49
GFDL-GOLD	0.48	1.4 (1.2)	2.4 (1.8)	2.0 (1.4)	-0.52
GFDL-MOM	0.54	1.4 (1.3)	2.6 (2.2)	2.0 (1.5)	-0.43
ICTP	1.51	2.1 (1.9)	3.4 (2.8)	2.2 (1.6)	-0.45
Kiel	0.58	1.6 (1.5)	2.0 (1.4)	2.1 (1.7)	-0.30
MRI	0.76	2.0 (1.6)	2.6 (2.0)	1.4 (1.2)	-0.38
NCAR	0.48	1.2 (1.1)	1.5 (1.2)	1.1 (1.0)	-0.33
NOCS	0.47	1.1 (0.88)	1.8 (1.2)	1.2 (0.94)	-0.30

Table 3: Global ocean root-mean-square difference (mm yr^{-1}) between an individual CORE-II simulation and the ensemble mean of all CORE-II simulations. This statistic measures the spread amongst the ensemble. We compute this statistic for the linear trend in bottom pressure (Figure 20); steric sea level (Figure 19) and steric sea level over the upper 700 m of the ocean (Figure 25); thermosteric sea level (Figure 22) and thermosteric sea level over the upper 700 m of the ocean (Figure 26); halosteric sea level (Figure 23), and halosteric sea level over the upper 700 m of the ocean (Figure 27). To compute the ensemble mean and differences, each model result is remapped to the one-degree spherical grid defined by the JPL/AVISO grid (Figure 15). The final column shows the global area average of the correlation between the thermosteric and halosteric time series for the years 1993-2007, with the maps of this correlation shown in Figure 24.

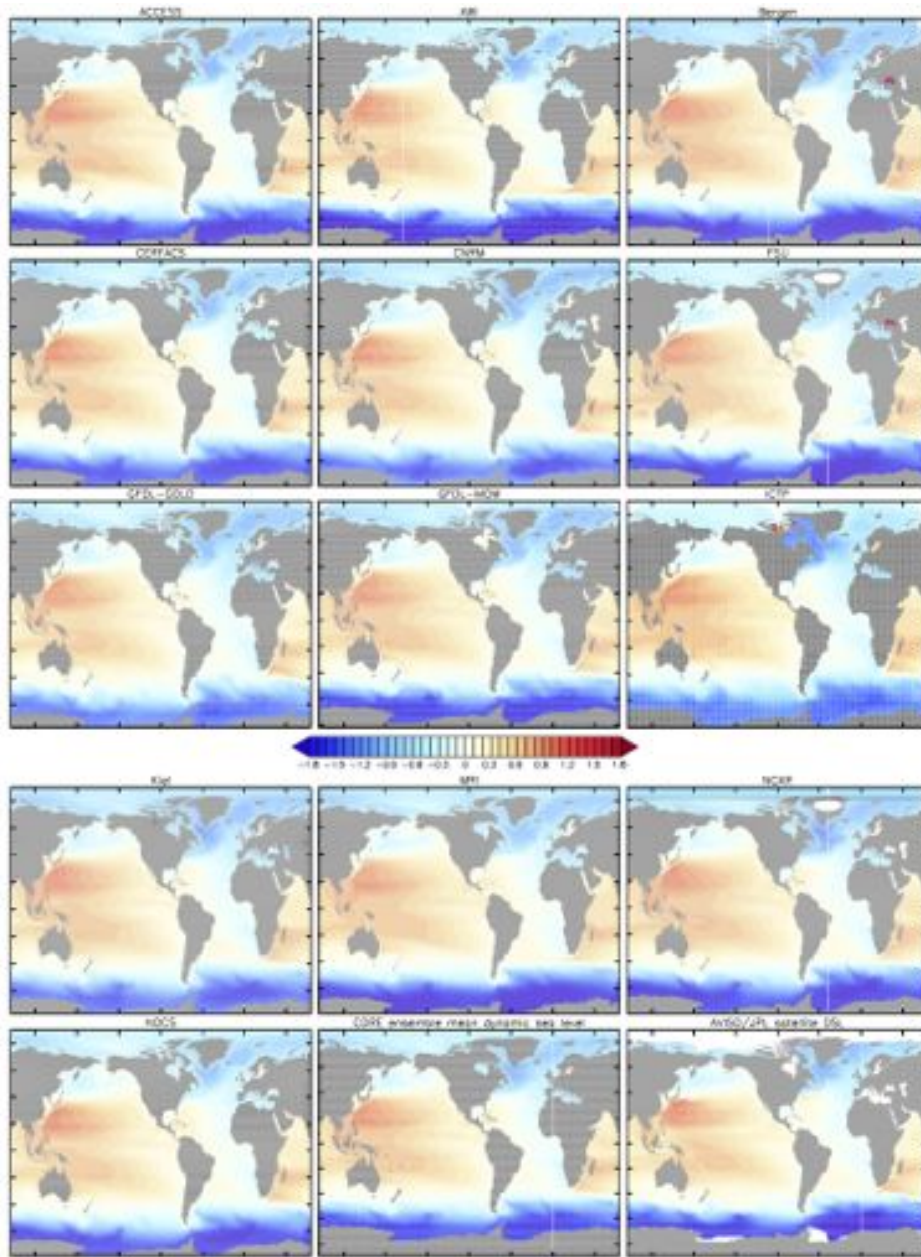


Figure 15: Time mean dynamic sea level (metre) (equation (5)) for the years 1993-2007 as computed from the fifth CORE-II cycle, along with the ensemble mean from the CORE-II simulations. Also shown are observation-based estimates of the time mean based on satellite measurements as analyzed by JPL. The JPL sea level field was obtained from AVISO, and downloaded from podaac.jpl.nasa.gov/dataset/AVISO_L4_DYN_TOPO_1DEG_1MO. The area mean for each pattern has been removed, so that the field has a zero area integral. The spatial correlation between the CORE ensemble mean and the AVISO analysis is 0.95.

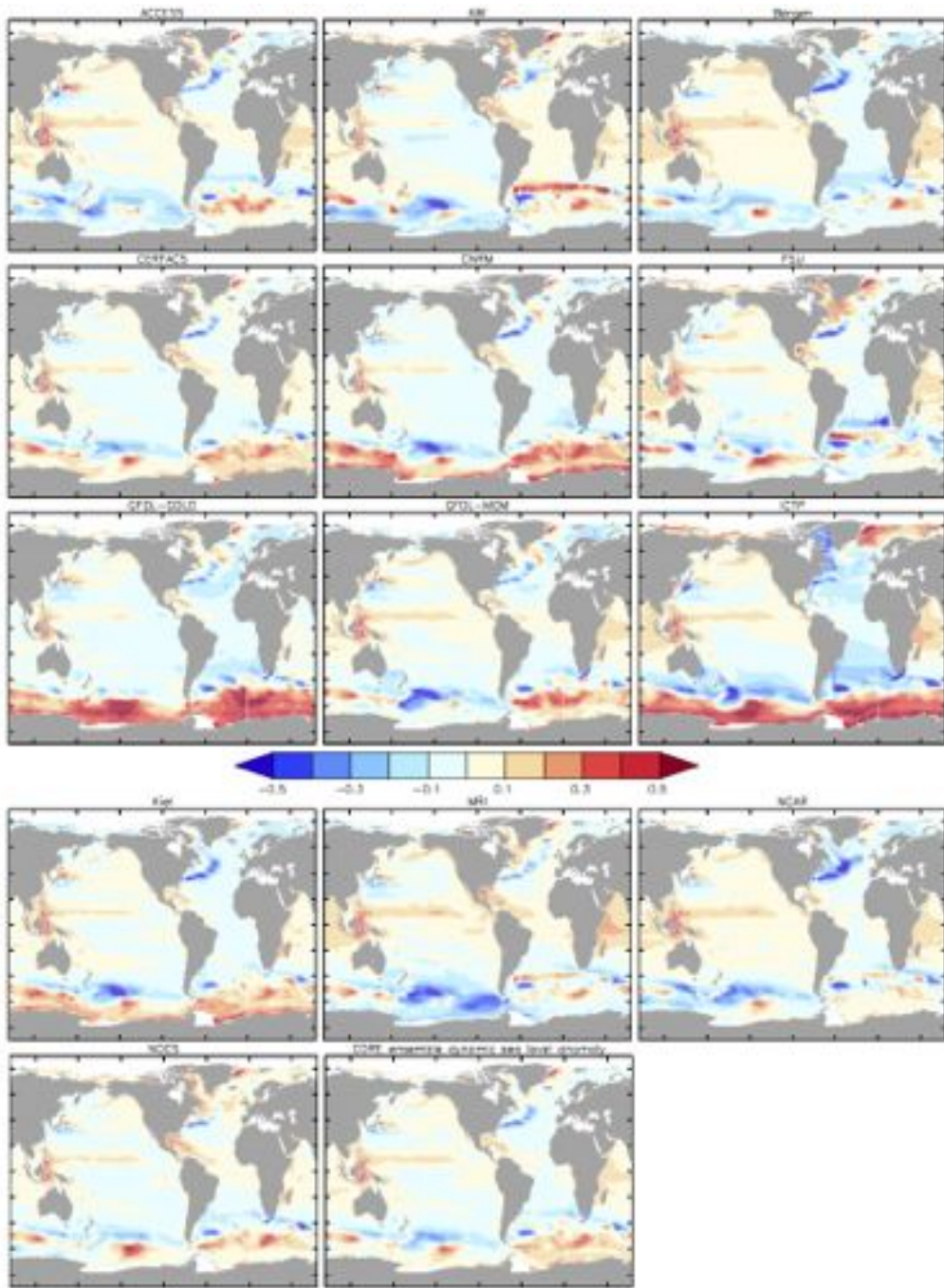


Figure 16: Bias in dynamic sea level (metre) for the years 1993-2007 as computed from the fifth CORE-II cycle as compared to the satellite measurements analyzed by JPL/AVISO (see Figure 15 caption). These patterns are computed as model minus satellite. The area mean for each pattern has been removed, so that the field has a zero area integral.

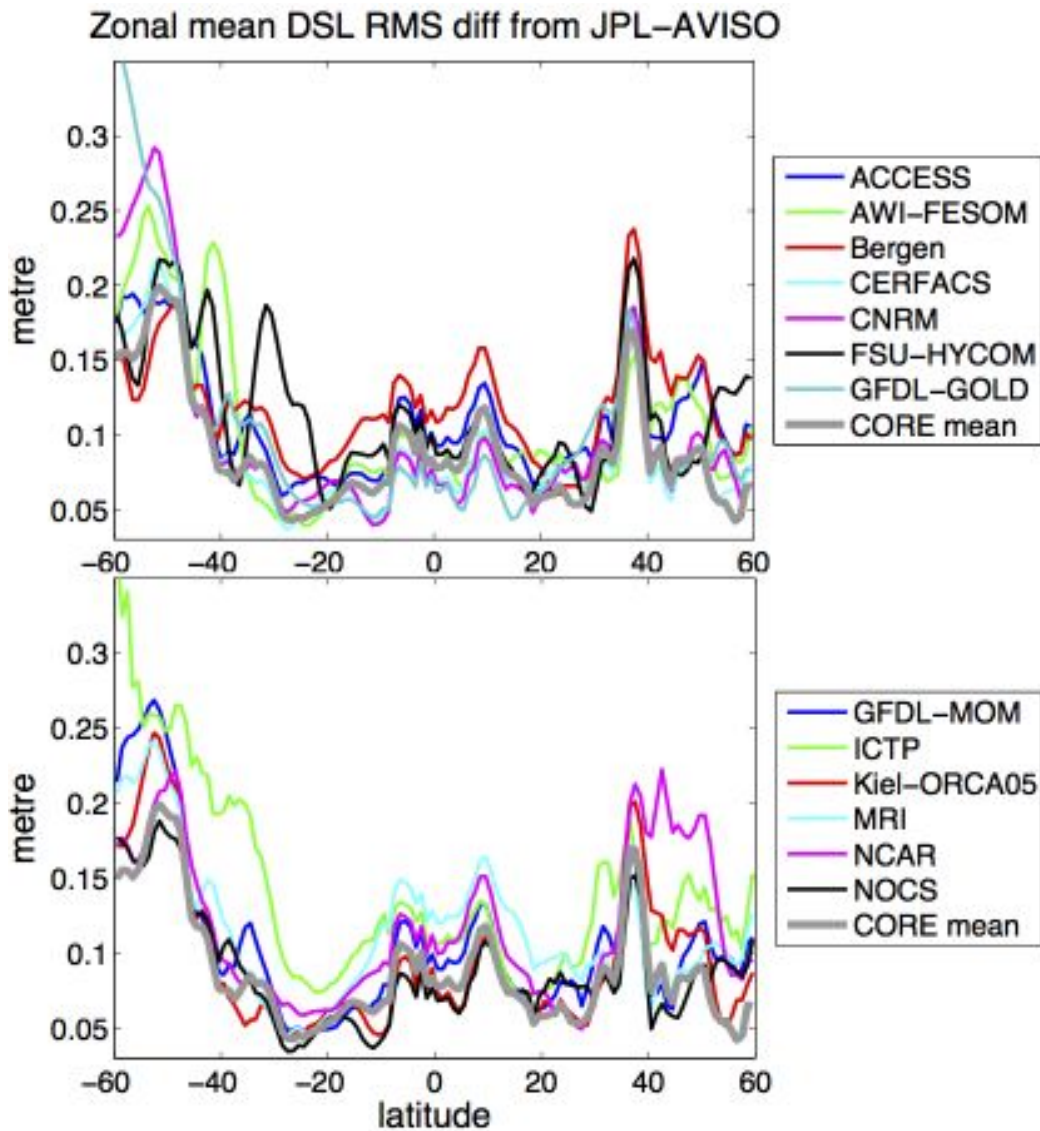


Figure 17: Zonal mean of the root-mean-square difference in the 1993-2007 time mean dynamic sea level with respect to the observations (Figure 15). This difference was computed as $\sqrt{\int dx (\zeta - \zeta^{\text{obs}})^2 / \int dx}$, where ζ^{obs} is the dynamic sea level taken from the AVISO product detailed in the caption to Figure 15, and the zonal integral extends over the World Ocean. The satellite measurements cover a latitude band roughly equal to 60°N – 60°S. The zonal mean difference for the ensemble mean sea level pattern is shown here in solid gray. Note the relatively small difference in the lower latitudes and large differences in the high latitudes, particularly in the Southern Ocean.

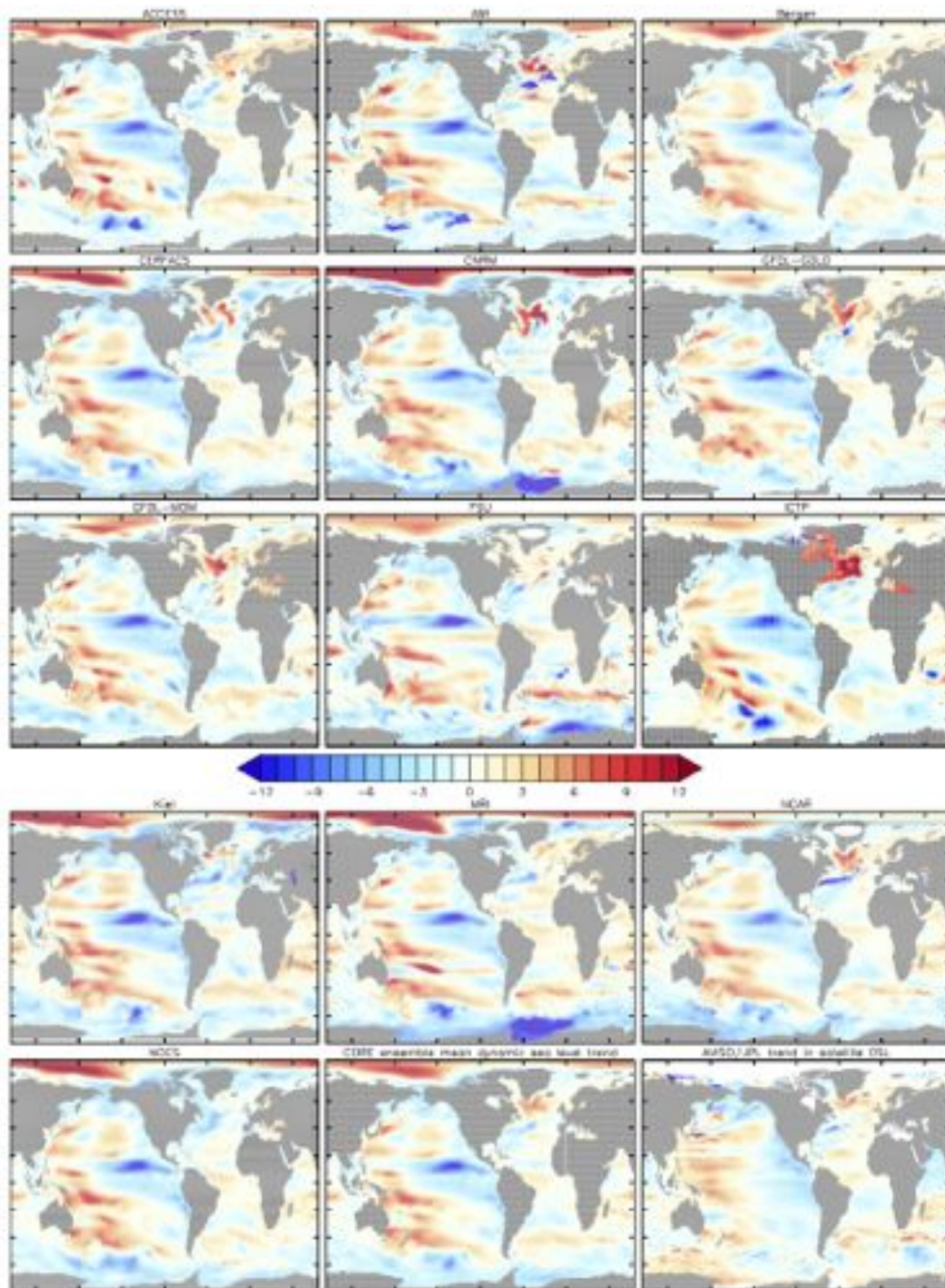


Figure 18: Linear trend in annual mean dynamic sea level (mm yr^{-1}) for the years 1993-2007 as computed from the fifth cycle of CORE-II simulations. Shown are results from the individual models as well as the ensemble mean computed using all simulations. Also shown are observation-based estimates of the trend based on satellite measurements (between roughly $60^\circ N - 60^\circ S$) as analyzed at the Jet Propulsion Laboratory. The JPL sea level field was obtained from AVISO, and downloaded from podaac.jpl.nasa.gov/dataset/AVISO_L4_DYN_TOP01_DEG_1M0. Root-mean-square differences of the trends are computed between the CORE-II simulations and the AVISO trend between roughly $60^\circ N - 60^\circ S$, with results given in Table 2. Linear trends for the model and observations are based on the annual mean of the spatial anomalous sea level field. That is, the trend is computed by first taking the annual mean sea level for each year and removing the global area mean, and then computing the trends of these annual mean spatial anomalies. The trends thus emphasize changes in patterns and do not include changes in the global mean. Consequently, positive trends in this figure represent sea level increases greater than the global mean, and negative trends are less than the global mean. For those regions where the AVISO analysis is nonzero, the spatial correlation between the CORE ensemble mean trend and the AVISO trend is 0.40.

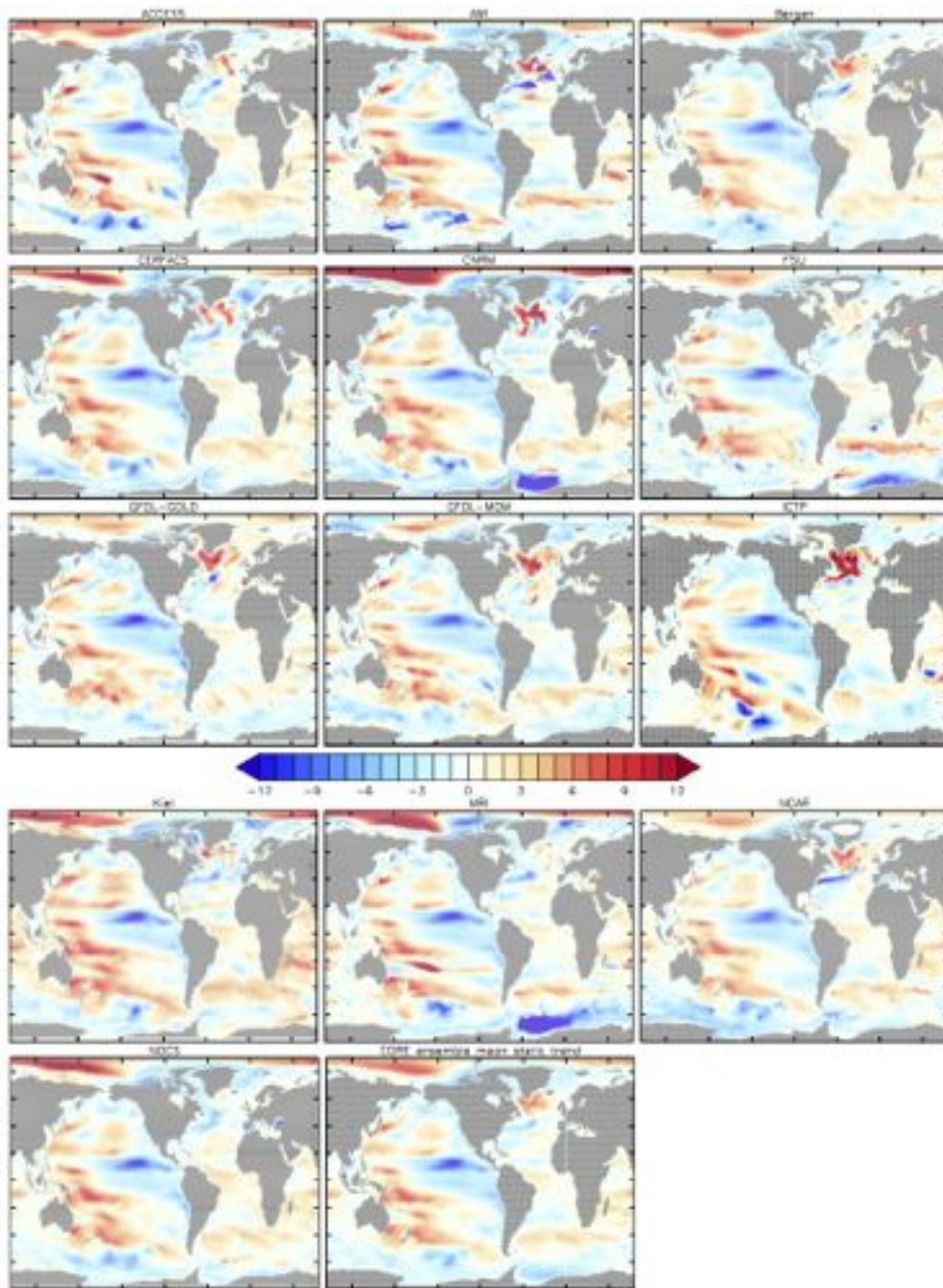


Figure 19: Linear trend in local steric sea level over the years 1993-2007 for the 5th CORE-II cycle, following from equations (3) and (13). Shown are results from the individual models as well as the ensemble mean. The units are mm yr^{-1} . A root-mean-square difference from the ensemble mean is given in Table 3, with this statistic indicating the spread amongst the ensemble of CORE-II simulations. The linear trends are computed by taking the annual mean steric contribution to sea level for each year and removing the global mean, so that the trends emphasize changes in patterns.

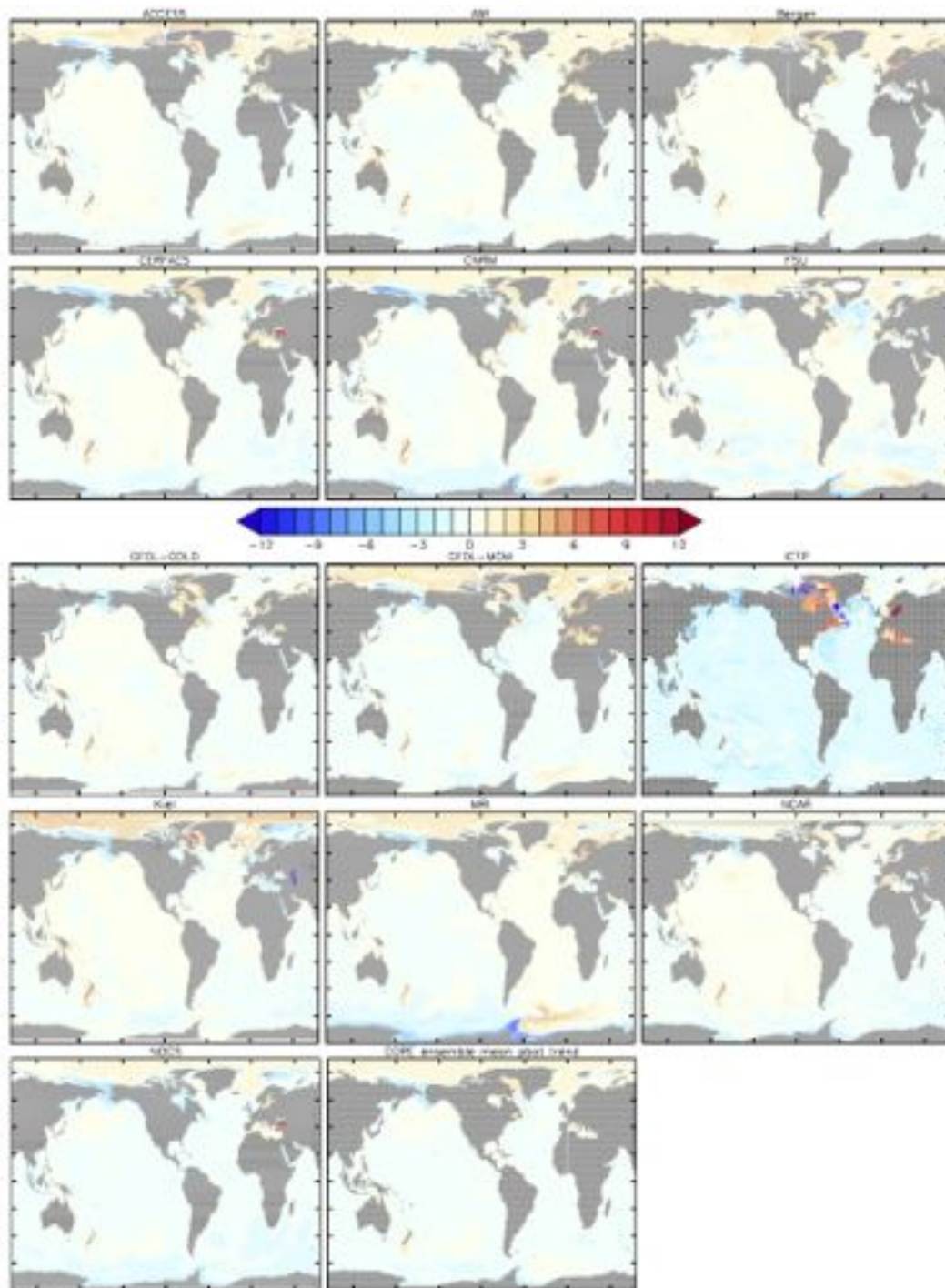


Figure 20: Linear trend in bottom pressure, converted to mm yr^{-1} according to equation (13), for the years 1993-2007 as computed from the fifth CORE-II cycle. Shown are results from the individual models as well as the ensemble mean. The linear trends are computed by taking the annual mean bottom pressure for each year and removing the global mean, so that the trends emphasize changes in patterns. We keep the same colour scale as for the sea level and steric trends shown in Figures 18–23, and 26 to facilitate direct comparison. However, Figure 21 shows the ensemble mean with a smaller colour range to highlight changes in the higher latitudes. In general, the bottom pressure trends are far smaller than the steric trends. A root-mean-square difference from the ensemble mean is indicated in Table 3, with this statistic indicating the spread amongst the ensemble of CORE-II simulations. Note that the small basin-wide downward trend for the ICTP simulation is associated with the absence of water in this model returning from enclosed marginal seas to the main ocean basins. Correspondingly, we exclude the Baltic from this simulation for computation of the ensemble mean.

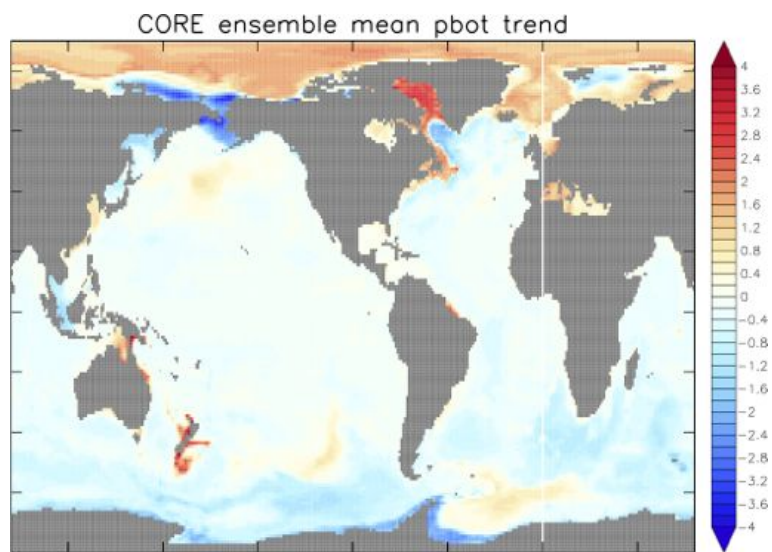


Figure 21: Ensemble mean of the linear trend in bottom pressure, converted to mm yr^{-1} according to equation (13), for the years 1993-2007 as computed from the fifth CORE-II cycle. Shown are results from the ensemble mean as in Figure 20, but with the colour scale reduced to emphasize the changes particularly in the higher latitudes and along shelves. Note the broad movement of mass from the Southern Hemisphere to the Northern Hemisphere, as discussed by Landerer et al. (2007a).

1031 5.3. Steric sea level trends decomposed into thermosteric and halosteric trends

1032 The steric term in equation (13) can be split into thermosteric and halosteric contributions,
1033 with details given in Appendix B1. We note that changes in sea level due to pressure dependence
1034 of the *in situ* density are generally negligible (see Section A5 for discussion of global mean sea
1035 level). Figures 22 and 23 show the thermosteric and halosteric trends. In the Pacific, the steric sea
1036 level trend is dominated by thermosteric processes. However, the halosteric effect is important
1037 in the Atlantic, especially in the subpolar gyre region. In this region, the thermosteric and
1038 halosteric effects partially compensate, with the thermosteric effect being larger. Both the steric
1039 effect, through halosteric processes, and ocean mass redistribution contribute to the positive sea
1040 level trend in the Arctic.

1041 Following Lombard et al. (2009) (see their Figure 8), we present in Figure 24 the correla-
1042 tion between time series of halosteric and thermosteric effects. Negative correlations indicate
1043 halosteric and thermosteric effects act mostly in a density-compensated manner so to reduce
1044 the overall steric effects relative to either the thermosteric or halosteric effects alone. Con-
1045 versely, positive correlations mean thermosteric and halosteric effects act in concert. Density-
1046 compensated changes occur when advection is the dominant mechanism for transport, in which
1047 potential temperature and salinity are conserved on fluid parcels. We speculate that their impacts
1048 on density compensate one another largely because warm/salty waters and cold/fresh waters tend
1049 to occur in the mean due to climatological forcing (excess of precipitation in cold high latitudes;
1050 excess of evaporation in warm low latitudes). See also Section 2b in Wunsch et al. (2007) for
1051 more discussion.

1052 The area average for the thermosteric/halosteric correlation over the World Ocean is nega-
1053 tive for all of the models (see figure caption). As noted above, the Atlantic basin is notable for
1054 its rather large density-compensated fluctuations, whereas the other basins have some regions of
1055 nontrivial positive correlation. The bulk of the simulations have area averaged values of around
1056 -0.3 to -0.4, with ACCESS, GFDL-MOM, ICTP, and GFDL-GOLD the largest negative correla-
1057 tions. Notably, the GFDL-GOLD and ICTP simulations indicate that compensation dominates
1058 in the Southern Ocean, whereas other models show closer to zero or slight positive correlations.

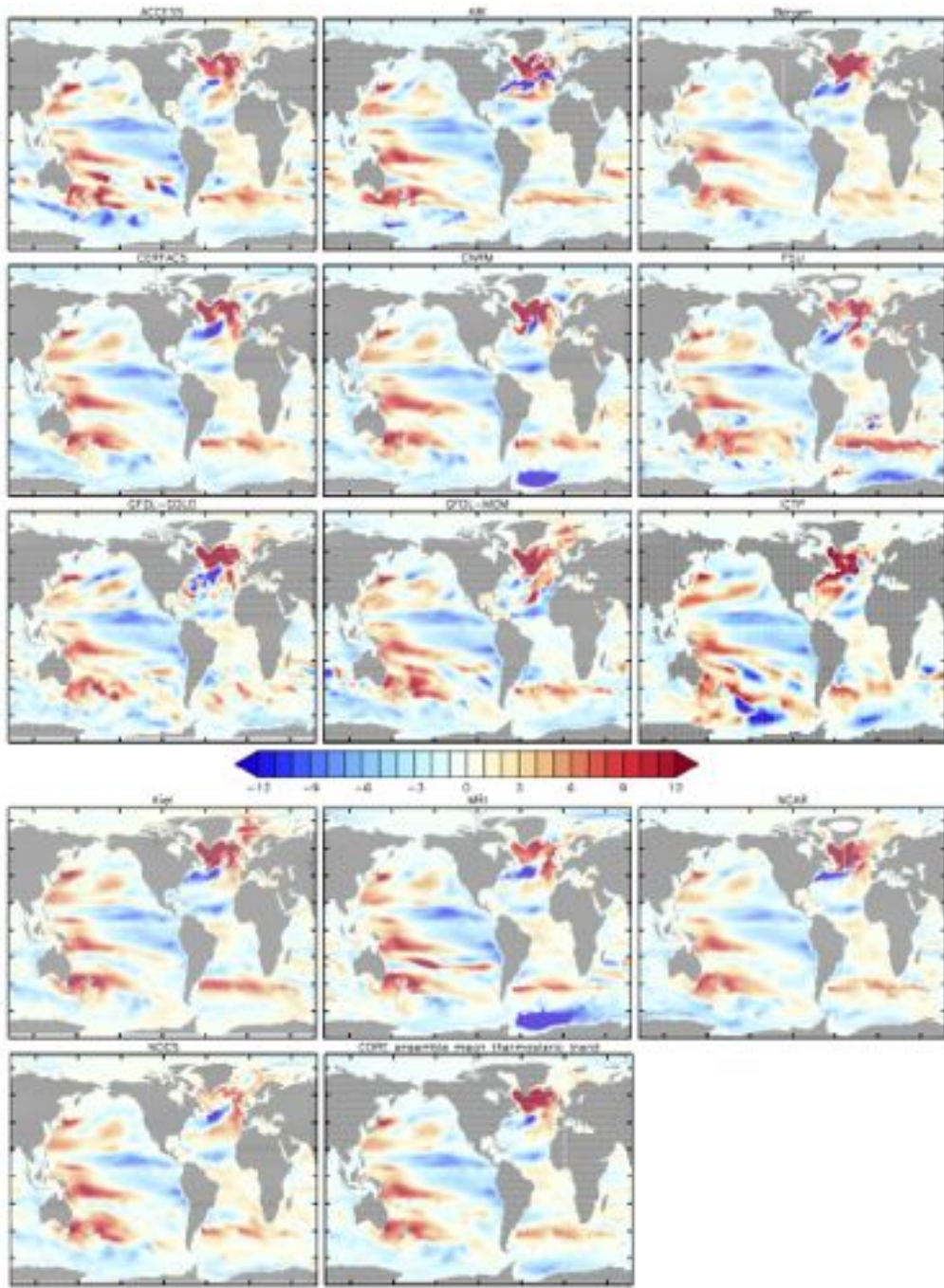


Figure 22: Linear trend in thermosteric sea level over the years 1993-2007 for the 5th CORE-II cycle. Shown are results from the individual models as well as the ensemble mean. The ensemble mean is computed using all simulations. The units are mm yr^{-1} . The linear trends are computed by taking the annual mean thermosteric contribution to sea level for each year and removing the global mean, so that the trends emphasize changes in patterns. A root-mean-square difference from the ensemble mean is given in Table 3, with this statistic indicating the spread amongst the ensemble of CORE-II simulations.

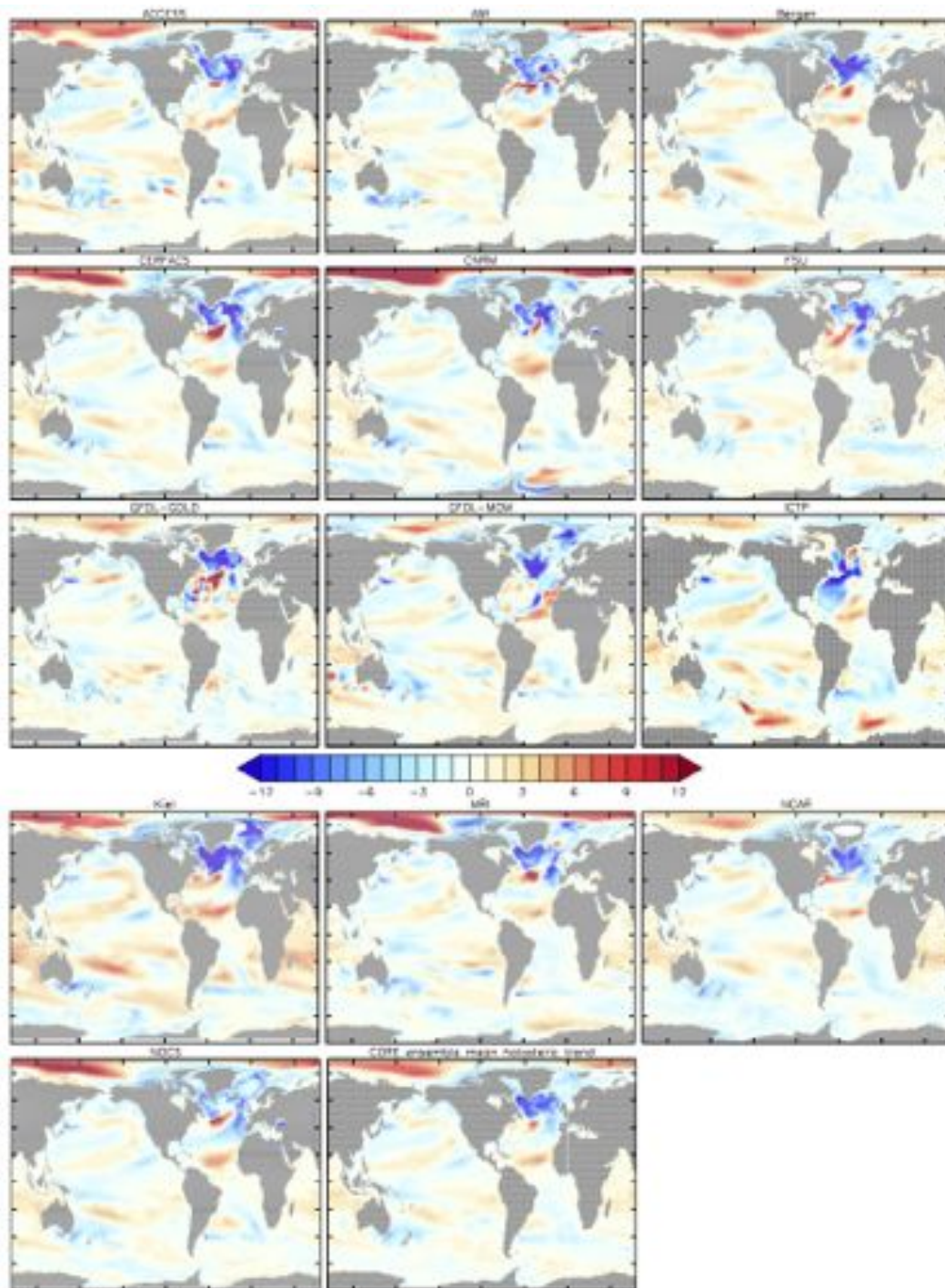


Figure 23: Linear trend in halosteric sea level over the years 1993-2007 for the 5th CORE-II cycle. The units are mm yr^{-1} . Shown are results from the individual models as well as the ensemble mean. The ensemble mean is computed using all simulations. The linear trends are computed by taking the annual mean halosteric contribution to sea level for each year and removing the global mean for that year, so that the trends emphasize changes in patterns. Note the generally smaller magnitude for the halosteric patterns in this figure relative to the thermosteric patterns shown in Figure 22, with exceptions being the rather large contributions in the subpolar North Atlantic and the Arctic ocean. A root-mean-square difference from the ensemble mean is given in Table 3, with this statistic indicating the spread amongst the ensemble of CORE-II simulations.

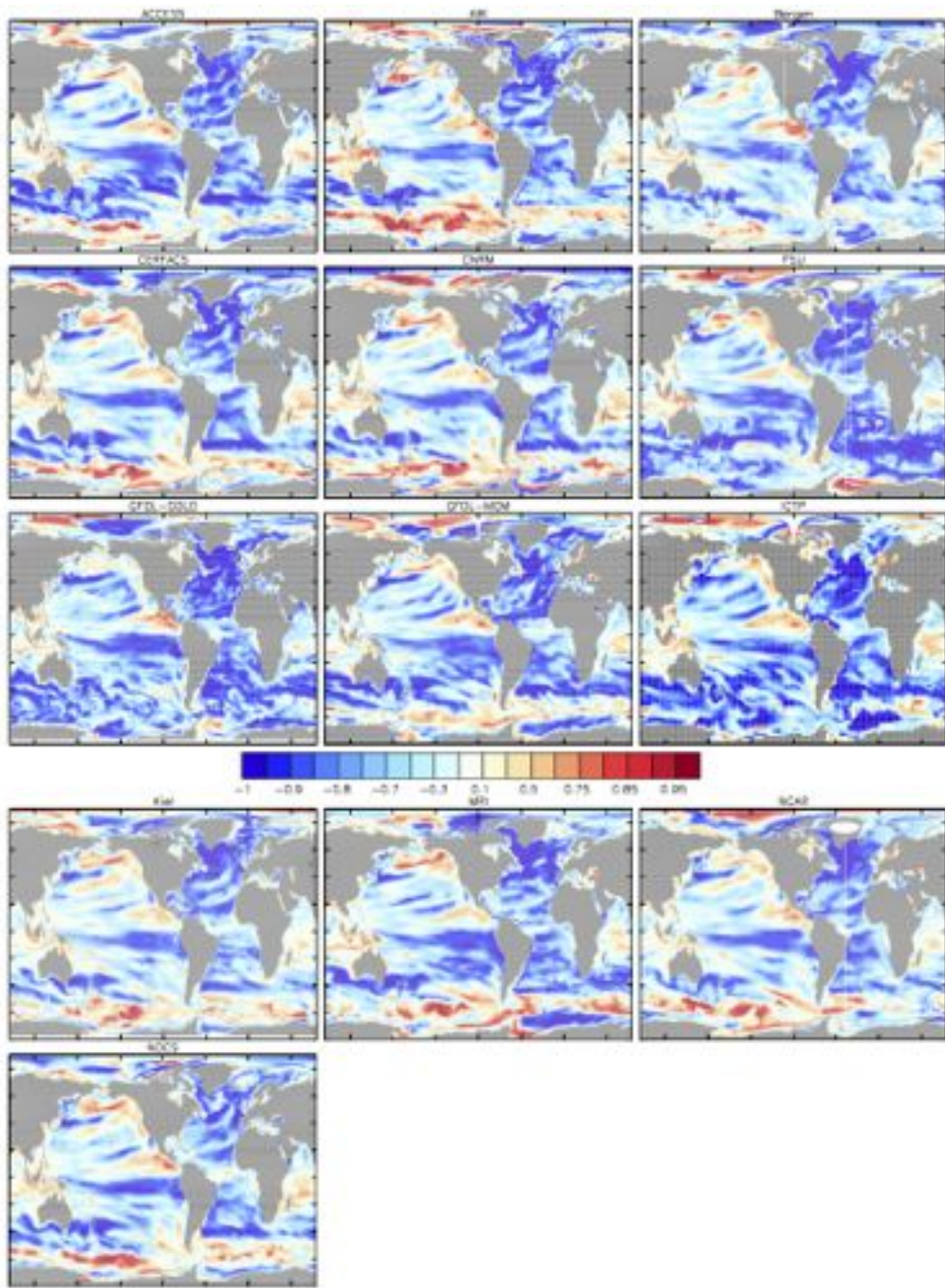


Figure 24: Correlation between the time series of halosteric and thermosteric effects over the years 1993-2007 for the fifth CORE-II cycle. Positive values indicate halosteric and thermosteric effects act in concert to either raise or lower sea level. The global area average of the correlation for each model is given in Table 3. The dominance of negative correlations indicates the dominance of density-compensated fluctuations in water masses.

1059 *5.4. Steric, thermosteric, and halosteric patterns over the upper 700 m*

1060 Limiting the analysis of steric trends to just the upper 700 m of the ocean allows us to
1061 compare the CORE-II simulations to various observation-based analyses. The Domingues et al.
1062 (2008) and Levitus et al. (2012) analyses focus on temperature changes, and so render an es-
1063 timate only for thermosteric changes. The Durack and Wijffels (2010) analysis provides both
1064 temperature and salinity trends, and we use it to estimate linear trends in observed steric, ther-
1065 mosteric, and halosteric sea level.

1066 We show the upper 700 m steric sea level trend in Figure 25, with Figures 26 and 27 showing
1067 the corresponding thermosteric and halosteric trends, respectively. As for the full depth trends
1068 (Figures 19, 22, and 23), the upper 700 m steric trend is dominated by the thermosteric trend,
1069 except in the subpolar North Atlantic and Arctic. A prominent steric sea level trend pattern
1070 for both the models and the observations is seen in the Pacific west-east gradient. Domingues
1071 et al. (2008) and Levitus et al. (2012) show a somewhat diffuse western Pacific high and eastern
1072 Pacific low, reflecting that seen for the satellite-based dynamical sea level trends in Figure 18.
1073 The models generally show a western Pacific positive trend closely aligned with the subtropical
1074 gyres, as well as an equatorial low that extends further into the western Pacific than seen in
1075 Domingues et al. (2008) and Levitus et al. (2012), but somewhat reflective of that seen in Durack
1076 and Wijffels (2010). We have more to say regarding the Pacific trends in Section 5.6.

1077 All models exhibit a maximum increase in steric sea level (Figure 25) along a zonal band
1078 extending across the south tropical Indian Ocean at about $10^{\circ} - 15^{\circ}\text{S}$. This pattern is indicative
1079 of a remote impact of the western Pacific warming via the Indonesian Passages and subsequent
1080 westward transmission by baroclinic Rossby waves as suggested by Schwarzkopf and Böning
1081 (2011).

1082 All models exhibit a rather small thermosteric trend in the Southern Ocean, whereas the
1083 full-depth thermosteric trend in Figure 22 shows a somewhat larger trend magnitude. Hence,
1084 the full-depth trend has a significant contribution from trends in the deep waters. Some of
1085 the deep Southern Ocean trend is associated with model drift, as some models show cooling
1086 whereas others show warming (see Figure 14 for the trends in zonal mean temperature). Each
1087 of the observation-based analyses show a positive trend in the Southern Hemisphere middle
1088 latitude mode water regions, particularly in the southwest Pacific, South Atlantic, and South
1089 Indian Ocean. The models also respect this positive trend, though somewhat more strongly in
1090 the Southwest Pacific. It has been suggested by Sallée et al. (2008) and Lombard et al. (2009)
1091 that these changes arise from movement of ocean fronts due to wind changes associated with
1092 Southern Annular Mode variations.

1093 We noted in Section 5.1 that the models exhibit an increase in sea level in the subpolar
1094 North Atlantic region, with this increase triggered (initiated) by decreased surface cooling in
1095 the sub-polar gyre over the period studied here, whilst the advective heat transport from the
1096 south is still anomalously high. The studies of Lohmann et al. (2009), Yeager et al. (2012)
1097 and Danabasoglu et al. (2014) provide more details. The Levitus et al. (2012) and Durack and
1098 Wijffels (2010) analyses reflect the positive sea level trend in this region, whereas it is largely
1099 missing in Domingues et al. (2008). As part of the North Atlantic changes in the models, many
1100 exhibit a significant thermosteric sea level decrease in the Gulf Stream extension, which is also
1101 reflected in the Levitus et al. (2012) analysis and to a smaller degree in Durack and Wijffels

1102 (2010) and Domingues et al. (2008).

1103 As mentioned in Section 3, the halosteric patterns are subject to caveats related to the use
1104 of surface salinity restoring for the CORE-II simulations. Additionally, the details of restoring
1105 are distinct across the models (see Danabasoglu et al. (2014)). Nonetheless, there are some
1106 common patterns, notably a positive halosteric trend in the Arctic and negative halosteric trend
1107 in the subpolar North Atlantic. The trends found in the Durack and Wijffels (2010) analysis
1108 share some features with the CORE-II simulations, such as a halosteric sea level lowering in
1109 the subpolar North Atlantic associated with an increased salinity. The Pacific patterns, however,
1110 show low correlation. The low Pacific agreement may be due to the smaller amplitude of the
1111 trend. The smaller trend may in turn be impacted more in a relative manner by differences in the
1112 surface salinity restoring between the CORE-II simulations. In general, the spatial correlation
1113 for the halosteric trends between Durack and Wijffels (2010) and the CORE ensemble mean is
1114 smaller than for the thermosteric trends.

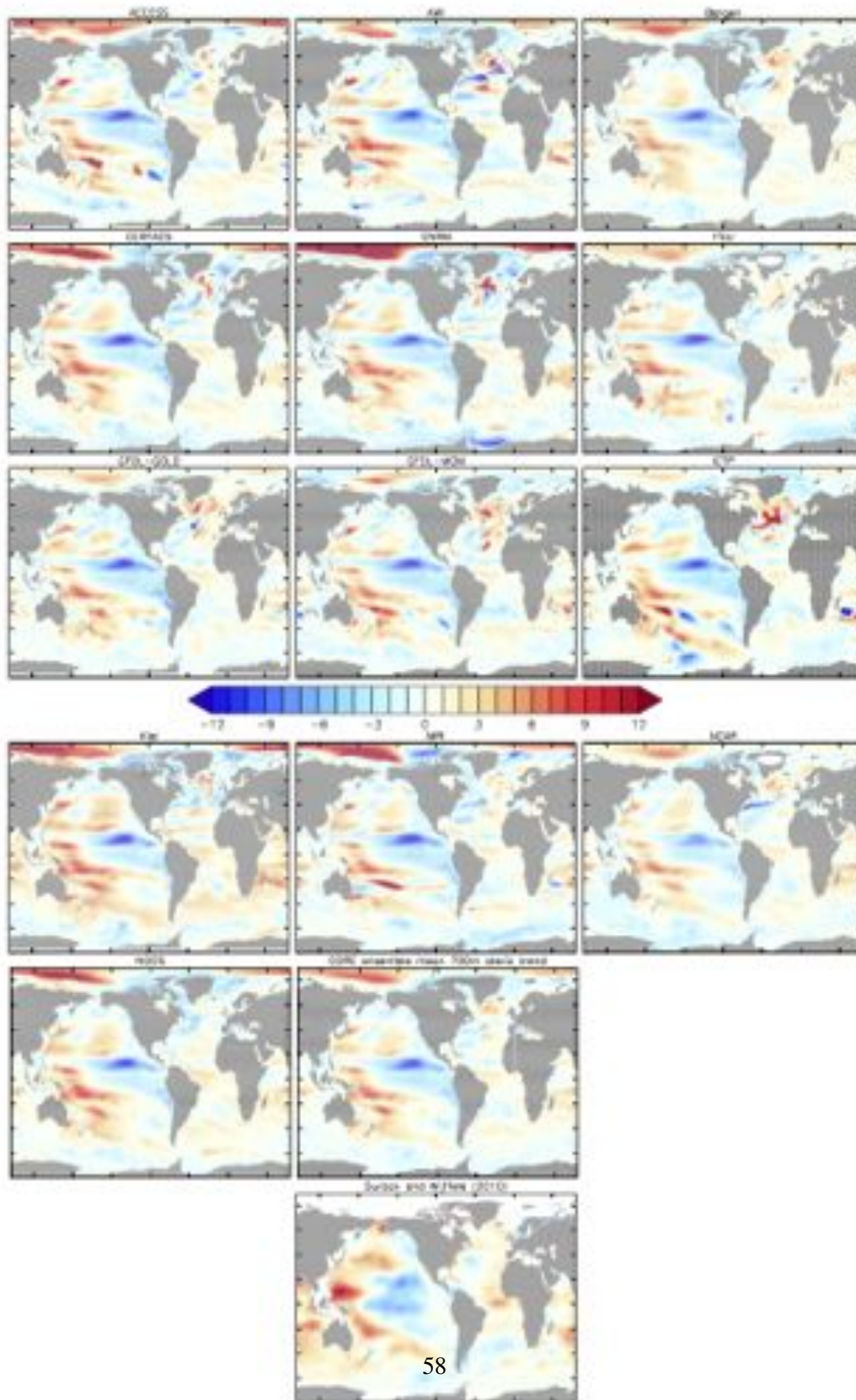


Figure 25: Linear trend (mm yr^{-1}) in steric sea level computed in the upper 700 m of water for years 1993-2007. The model results are taken from the 5th CORE-II cycle. The CORE-II ensemble mean is computed using all simulations. Observation-based estimates are shown from an updated analysis based on Durack and Wijffels (2010). The linear trends are computed by taking the annual mean steric contribution to sea level for each year and removing the global mean, so that the trends emphasize changes in patterns. A root-mean-square difference from the ensemble mean is given in Table 3. The spatial correlation between the CORE ensemble mean and the Durack and Wijffels (2010) observational analyses is 0.39.

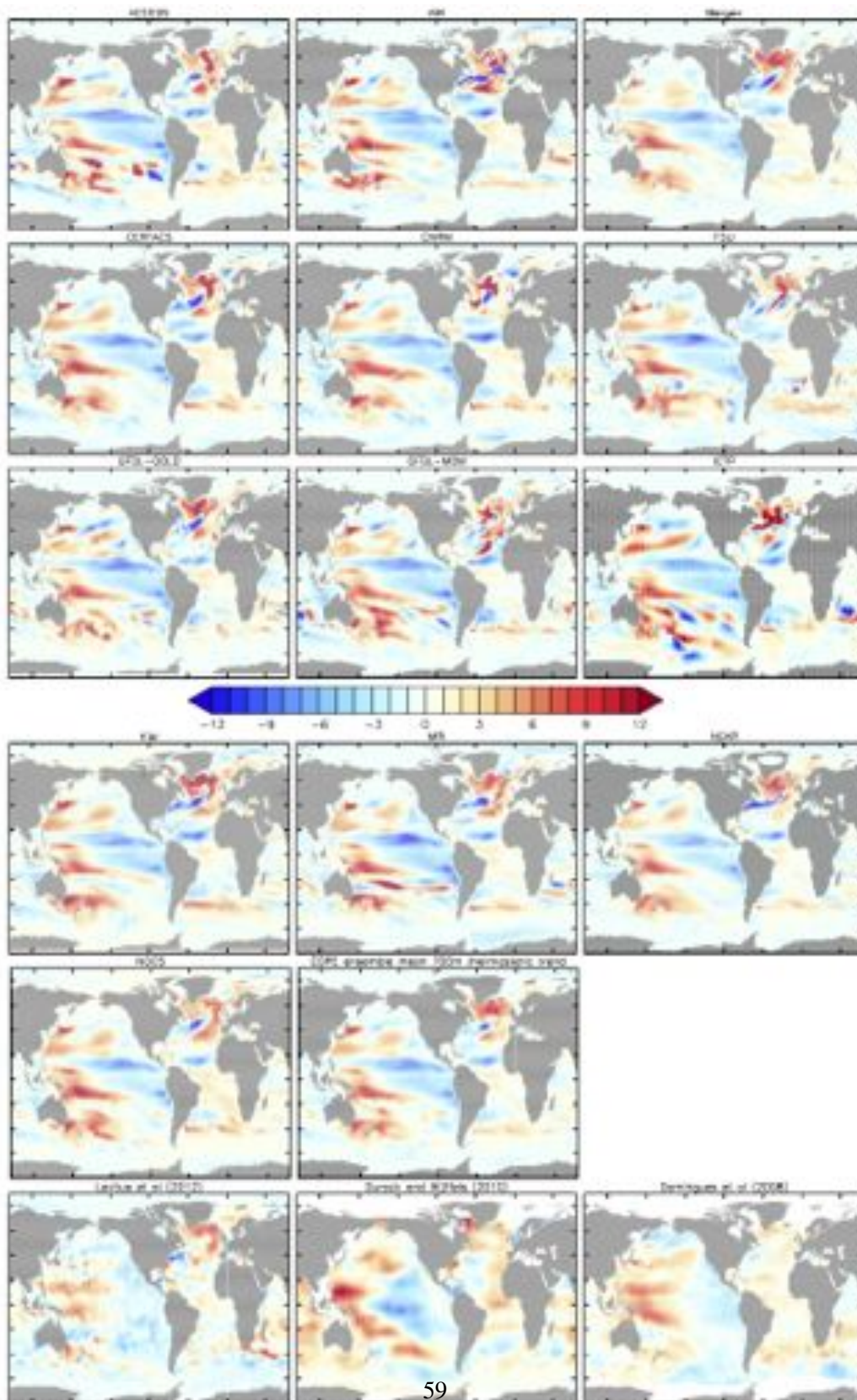


Figure 26: Linear trend (mm yr^{-1}) in thermosteric sea level computed in the upper 700 m of water for years 1993-2007. The model results are taken from the 5th CORE-II cycle. The CORE-II ensemble mean is computed using all simulations. Observation-based estimates are shown from Levitus et al. (2012); an updated analysis based on Domingues et al. (2008) and Church et al. (2010); and an updated analysis based on Durack and Wijffels (2010). The linear trends are computed by taking the annual mean thermosteric contribution to sea level for each year and removing the global mean, so that the trends emphasize changes in patterns. A root-mean-square difference from the ensemble mean is given in Table 3. The spatial correlation between the CORE ensemble mean and the observational analyses is given by CORE-Levitus=0.31, CORE-Domingues=0.43, CORE-Durack=0.31.

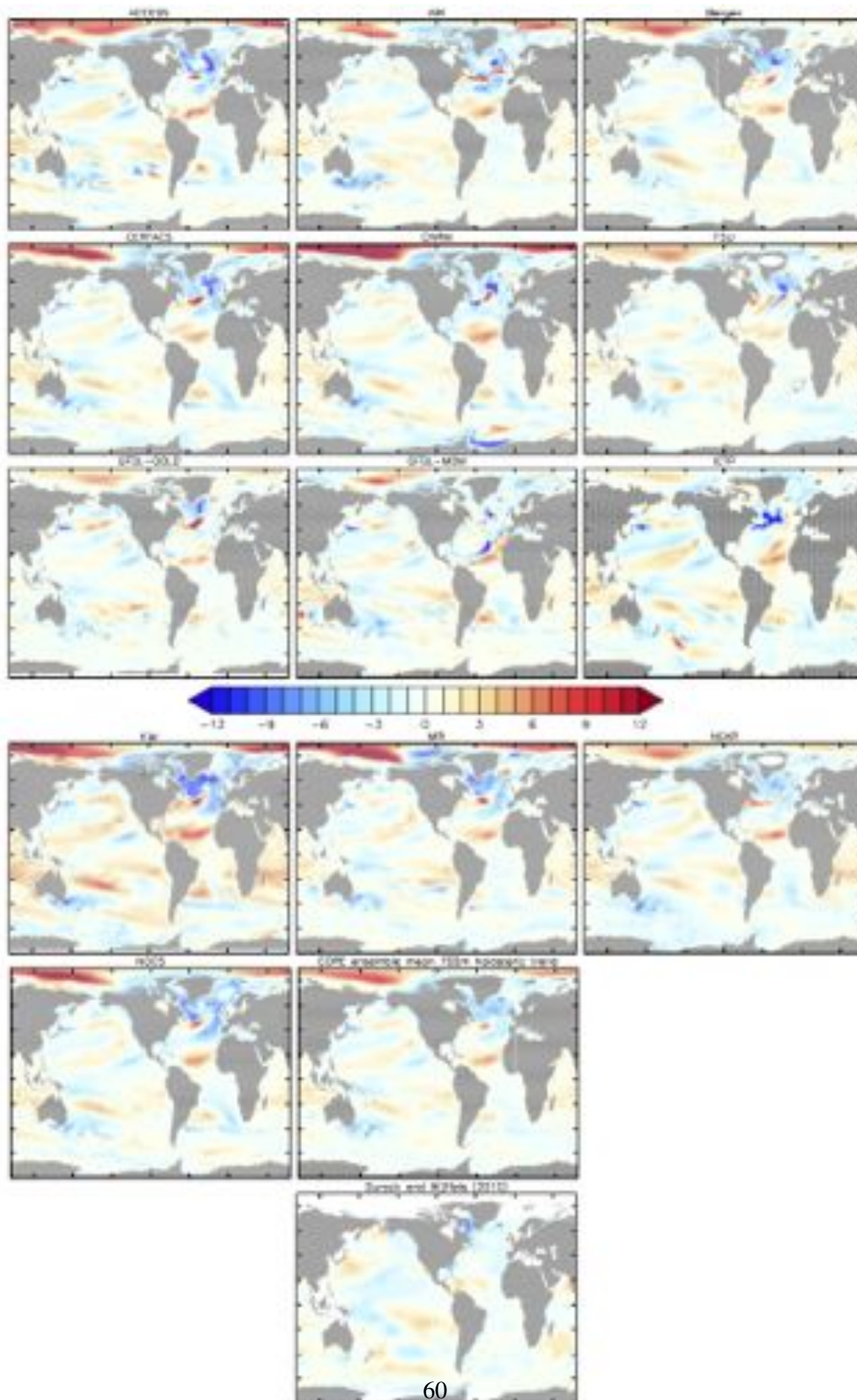


Figure 27: Linear trend (mm yr^{-1}) in halosteric sea level computed in the upper 700 m of water for years 1993-2007. The model results are taken from the 5th CORE-II cycle. The CORE-II ensemble mean is computed using all simulations. Observation-based estimates are shown from an updated analysis based on Durack and Wijffels (2010). The linear trends are computed by taking the annual mean halosteric contribution to sea level for each year and removing the global mean, so that the trends emphasize changes in patterns. A root-mean-square difference from the ensemble mean is given in Table 3, with this statistic indicating the spread amongst the ensemble of CORE-II simulations. The spatial correlation between the CORE ensemble mean and the Durack and Wijffels (2010) observational analysis is 0.18.

1115 *5.5. Comments on the North Atlantic patterns of sea level change*

1116 North Atlantic dynamic sea level changes are influenced by the Atlantic meridional over-
1117 turning circulation (AMOC). High-quality tide gauge records show that both the absolute values
1118 and acceleration of the sea level rise along the northeast USA, north of Cape Hatteras, were
1119 faster and larger than the global mean during the past 60 years (Sallenger et al., 2012; Ezer
1120 et al., 2013), consistent with model projections under the 21st century greenhouse-gas emission
1121 scenarios (Yin et al., 2009; Yin, 2012). In addition to a possible long-term trend, some studies
1122 have identified the potential role of multidecadal variability in this region (Chambers et al., 2012;
1123 Kopp, 2013). Nonetheless, recent sea level rise in this region exhibited some unusual behavior.
1124 For example, most tide gauge stations on the New England and Canada coast recorded a large
1125 sea level jump during 2009-2010 of up to 100 mm, which is unprecedented and correlated with
1126 the 30% downturn of the AMOC (McCarthy et al., 2012) as well as the NAO index. During the
1127 period 1993-2007 considered in the present paper, the dynamic sea level in the North Atlantic
1128 was dominated by a dipole structure, with a DSL fall in the Gulf Stream and a DSL rise in the
1129 subpolar gyre (see Häkkinen and Rhines (2004) and Zhang (2008)). This dipole pattern has been
1130 captured by the CORE-II models as shown by the CORE-II ensemble mean in Figure 18. Due
1131 to multi-decadal variability in North Atlantic, the decadal DSL trend shown in Figure 18 may
1132 not be representative of the longer term.

1133 *5.6. Comments on the Pacific patterns of sea level change*

1134 The western Pacific is a hotspot for observed sea level rise, with the fastest sea level rise on
1135 the globe having occurred in this region since 1993. The west-east gradient of the dynamic sea
1136 level change seen in the simulations (Figure 18) is consistent with the intensification of the east-
1137 erly trade winds (see Figure 28), according to the balance of the pressure gradient force and wind
1138 stress in the equatorial region (Timmermann et al., 2010; Merrifield, 2011; Merrifield and Mal-
1139 trud, 2011; McGregor et al., 2012). The negative anomalies of the wind stress curl in the middle
1140 and western tropical Pacific cause downwelling of surface warm waters, and deepening of the
1141 thermocline (see Figure 29). The downward migration of the thermocline leads to a significant
1142 thermosteric sea level rise in the western Pacific (Becker et al., 2012). In contrast, positive wind
1143 stress curl anomalies in the eastern tropical Pacific and along the west coast of South America
1144 result in an enhanced suction of cold deep water, and a shoaling of the thermocline. This process
1145 leads to a reduction in the sea level in the eastern Pacific.

1146 Feng et al. (2010), Merrifield et al. (2012), Meyssignac et al. (2012), and McGregor et al.
1147 (2012) suggest that the west-east gradient of the DSL change reflects the negative phase of the
1148 Pacific Decadal Oscillation, rather than a trend induced by external climate forcing as originally
1149 proposed by Merrifield (2011) and Merrifield and Maltrud (2011). Interestingly, the wind stress
1150 curl caused a similar downwelling in the tropical Atlantic. But the dynamic sea level signal is
1151 weaker than in the Pacific (Figure 18), with this difference perhaps due to the different size of
1152 the two ocean basins. Zhang and Church (2012) pointed out that the spatial patterns of sea level
1153 trend over a similar period in the Pacific are significantly affected by decadal climate variability,
1154 and to first order the spatial patterns can be approximated by sea level trends due to aliasing of
1155 the decadal variability plus the global mean sea level rise. Finally, we note that the CORE-II

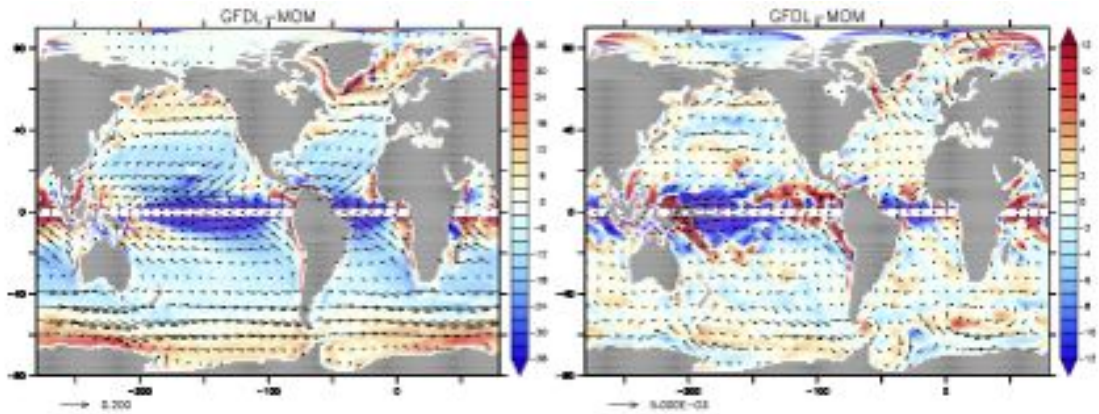


Figure 28: Left panel: time mean wind stress vectors (stress applied to the ocean model surface; N m^{-2}) and Ekman suction/pumping velocity, $w_e = \rho_0^{-1} \hat{\mathbf{z}} \cdot [\nabla \wedge (\boldsymbol{\tau}/f)]$, (colours; 10^{-7} m s^{-1}) for years 1993-2007. Blue shading indicates downward Ekman pumping. The equatorial region is omitted due to vanishing Coriolis parameter. Right panel: linear trends, with wind stress trend (vectors) in units of $\text{N m}^{-2} \text{ yr}^{-1}$ and trend in Ekman suction/pumping (colours) in units of $10^{-8} \text{ m s}^{-1} \text{ yr}^{-1}$. To minimize clutter, only every 9th vector in the x-direction and 7th vector in the y-direction are shown. We show results from the GFDL-MOM simulation, with other models showing similar structures, given that they all use the same atmospheric winds to generate stress. For the tropical and mid-latitude Pacific, note the trend for increased trade winds (easterlies) with near-equatorial Ekman downwelling in the central-west that pushes down the thermocline. This forcing is associated with increased thermocline rise in the west Pacific as shown in Figure 26 and as discussed by Feng et al. (2010); Bromirski et al. (2011); Merrifield (2011); Merrifield and Maltrud (2011).

1156 simulations generally show a strong negative centre at the eastern Pacific, with the magnitude
 1157 stronger than in the observations.

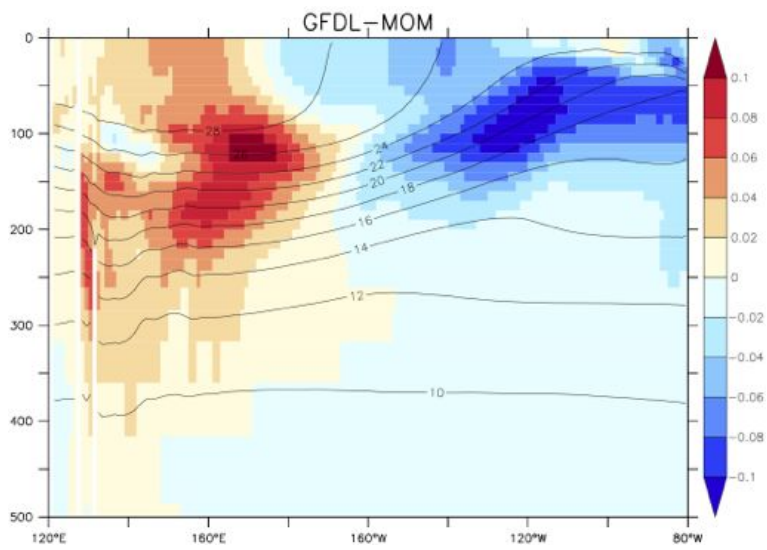


Figure 29: Linear temperature trend along the equator in the Pacific for years 1993-2007 in the GFDL-MOM simulation, shown in units of degrees Celsius per year. The contours show the time mean temperature over years 1993-2007. Note the warming in the west and cooling in the east, with these trends reflected in the thermosteric sea level trends seen in Figure 26.

1158 **6. Summary and discussion**

1159 Sea level emerges from mechanical and thermodynamic forcing on the ocean boundaries,
1160 and is affected by transport and mixing in the ocean interior. Thus, all physical processes im-
1161 pacting the ocean impact sea level, including physical oceanographic processes as well as geo-
1162 physical processes associated with changes in the earth’s gravity and rotation. Sea level is a key
1163 field to accurately capture in simulations to assess the potential for climate impacts, particularly
1164 in coastal regions. Simulation of both its global mean and regional patterns in turn provides a
1165 strong test for numerical model integrity and utility.

1166 In this study, we followed the protocol of the Coordinated Ocean-sea ice Reference Experi-
1167 ments, with details given by Griffies et al. (2009b) and Danabasoglu et al. (2014). These global
1168 ocean-sea ice simulations do not include all processes important for sea level (see Slangen et al.
1169 (2012) for a more comprehensive approach). Rather, the present study focuses on the global
1170 ocean-sea ice climate problem using a prescribed atmospheric state to derive boundary fluxes
1171 and with a static gravitational force, fixed land-sea boundaries (i.e., fixed ocean bottom topog-
1172 raphy). We therefore focused on ocean-centric measures of simulation features, predominantly
1173 associated with steric, thermosteric, and halosteric effects.

1174 *6.1. Why CORE comparisons are useful*

1175 The models contributing to this study represent a cross-section of the state-of-the-science
1176 configurations used for global ocean and climate studies, with many research groups using
1177 ocean-sea ice configurations taken from their companion coupled climate models that con-
1178 tributed to the CMIP5 project (Taylor et al., 2012). Additionally, some of the participating
1179 groups are only just now entering the “mainstream” of ocean climate modelling, such as the
1180 finite element ocean model from AWI-FESOM.

1181 The various CORE comparison projects (e.g., the present paper as well as Griffies et al.
1182 (2009b) and Danabasoglu et al. (2014)) provide a valuable framework for ocean-sea ice climate
1183 modelling. One key feature of such projects is the sharing of experience and knowledge between
1184 research groups that is essential for advancing both the model tools and the associated science
1185 supported by the simulations. That is, it is deeply valuable to analyze a suite of simulations
1186 in a side-by-side manner under well defined experimental conditions such as CORE. Doing
1187 so offers a powerful means to expose errors that may otherwise go unnoticed, and to identify
1188 robust features of scientific interest. Furthermore, if the present paper and its companions have
1189 longevity in the literature, we suggest they will do so largely by detailing analysis methods and
1190 model diagnostics of use to characterize ocean climate simulations.

1191 There are reasons to expect the mean of a well sampled model suite to perform better than
1192 any individual model, largely due to the cancellation of model errors. We have partial support
1193 for this result from Figure 17 and Table 2, which consider the model dynamic sea level compared
1194 to the satellite measures. In the following summary of CORE-II results, we therefore focus on
1195 the model ensemble mean as it compares to various observation-based estimates. We weight
1196 each model equally. We focus here on a descriptive discussion, particularly given the largely
1197 unquantified uncertainties in the observation-based analyses. At this stage, the use of more
1198 sophisticated statistical comparison tools is unnecessary.

1199 *6.2. Summary of global mean heat and global mean sea level*

1200 We considered global mean heat content and thermosteric sea level during the first portion
1201 of this paper. We raised important caveats in Sections 2.6 and 2.7 regarding the ability of the
1202 CORE-II protocol to make assessments of global mean sea level over long time scales. As
1203 emphasized by Doney et al. (2007), Large and Yeager (2009), and Large and Yeager (2012),
1204 the CORE-II atmospheric state is designed primarily for studies of interannual ocean variability.
1205 Our investigations of multi-decadal time scales supported this restricted use of the CORE-II
1206 simulations for global mean sea level studies, prompting us to focus the global mean analysis on
1207 the same 1993-2007 period used for regional pattern analysis.

1208 Much of the trend in thermosteric sea level from the CORE-II simulations during 1993-2007
1209 arises from changes in the upper 700 m of ocean (Figure 8). We exhibit in Figure 30 the time
1210 series for the CORE-II ensemble mean global mean heat content and thermosteric sea level,
1211 computed over the upper 700 m. The starting point for the ocean heat content and thermosteric
1212 sea level is biased low relative to the observation-based estimates. However, the rate of change is
1213 compatible with that estimated by Domingues et al. (2008), yet lower than the rate estimated by
1214 Levitus et al. (2012). We offered conjectures in Section 2.6 for why we may expect the CORE-II
1215 simulations to be biased low. One reason relates to an insufficient amount of warming found
1216 in the CORE-II atmospheric state, as suggested by the smaller rise in global mean SST in the
1217 simulations relative to observation-based estimates (Figure 2). Another reason is related to the
1218 use of a repeated 60-year cycle for the CORE-II simulations, which in effect introduces a lag in
1219 the ocean response related to the time scale for ocean adjustment to changes in the surface heat
1220 fluxes.

1221 There is negligible trend in global mean steric changes between 700 m-2000 m (Figure
1222 9), with the notable exception being in the high latitudes (Figure 14). High latitude regions
1223 furthermore show widely varying trends for water deeper than 2000 m, due to the differing drifts
1224 inherent in simulations that have run for only 300 years. It takes a few thousand years for the
1225 deep ocean to reach equilibrium (Stouffer, 2004; Danabasoglu, 2004).

1226 *6.3. Summary of temperature trend patterns*

1227 We considered pattern changes in ocean heat content and temperature in Section 4. Direct
1228 comparison to observation-based analyses are available for heat content trends (Figure 12), or
1229 for the related trends in temperature as averaged over the upper 700 m of the ocean. The CORE-
1230 II ensemble mean of the depth average temperature change is shown in Figure 31. We also show
1231 the zonal mean of the temperature change in Figure 14 for the full suite of CORE-II simulations,
1232 and the ensemble mean is again shown in Figure 32.

1233 We highlight here salient features of the linear trend in upper 700 m vertically averaged
1234 temperature and zonal mean temperature from the CORE-II ensemble mean as compared to the
1235 observation-based analyses.

- 1236 • PACIFIC: Both CORE-II simulations and observation-based analyses indicate a warming in
1237 the west and cooling in the east low to mid-latitude Pacific. CORE-II and Durack and
1238 Wijffels (2010) exhibit an eastern cooling that reflects an El Niño Southern Oscillation
1239 pattern, whereas the cooling in Domingues et al. (2008) and Levitus et al. (2012) is less
1240 distinct. Cooling is found in the South Pacific and into the Southern Ocean in Domingues

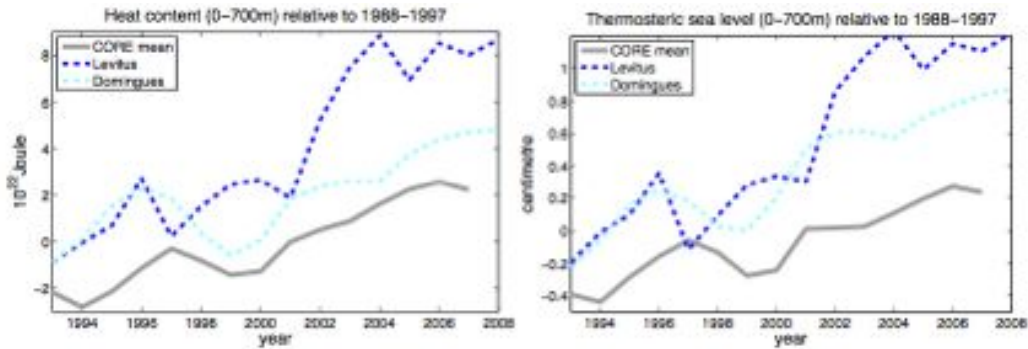


Figure 30: Time series for annual mean ocean heat content and thermosteric sea level integrated over the upper 700 m of ocean, taken from the ensemble mean of the CORE-II simulations and two observation-based analyses. Results from the full model suite are presented in Figure 8. The warming rate found in the CORE-II simulations is largely compatible with that estimated by Domingues et al. (2008), yet lower than the rate estimated by Levitus et al. (2012).

1241 et al. (2008) and Durack and Wijffels (2010), and marginally in the CORE-II simulations,
 1242 whereas there is marginal warming in this region in the Levitus et al. (2012) analysis.
 1243 The CORE-II simulations show a warming in the Kuroshio extension of the North Pacific,
 1244 yet there is a weaker signal in the observation-based analyses. This discrepancy may be
 1245 related to an inaccurate representation of the Kuroshio in the coarse-resolution CORE-II
 1246 simulations, where the Kuroshio generally overshoots the correct separation latitude
 1247 (around 35°N) and flows northward along the east coast of Japan. Warmer surface waters
 1248 are in turn carried by the biased Kuroshio during recent years in the simulations.

- 1249 • ATLANTIC: Both CORE-II and observation-based analyses indicate a warming in the sub-
 1250 polar North Atlantic, with the warming found in Domingues et al. (2008) muted relative to
 1251 the others. The zonal mean changes in Figure 32 indicate that the North Atlantic warming
 1252 extends to around 1000-2000 m.

1253 The Gulf Stream extension for CORE-II and observation-based analyses show some cool-
 1254 ing, with the signal in CORE-II stronger. This cooling is associated with a southward shift
 1255 of the Gulf Stream during 1993-2007. CORE-II simulations also show some cooling in
 1256 the near equatorial region, which is largely missing in the observation-based analyses. The
 1257 South Atlantic is generally warming in CORE-II and observation-based analyses, though
 1258 CORE-II and Durack and Wijffels (2010) reveal mild cooling in the high latitudes of the
 1259 South Atlantic.

- 1260 • INDIAN: The observation-based analyses indicate general warming in the Indian Ocean,
 1261 with Durack and Wijffels (2010) showing the largest that extends through to the Indian
 1262 Ocean sector of the Southern Ocean. The CORE-II simulations show a marginal cooling,
 1263 whereas Domingues et al. (2008) and Levitus et al. (2012) show a marginal warming,
 1264 though note that Domingues et al. (2008) and Durack and Wijffels (2010) show a hint of
 1265 cooling in the north Arabian Sea.

- 1266 • SOUTHERN: The CORE-II simulations reveal a warming in the South Pacific, South At-
1267 lantic, and South Indian ocean, with some cooling to the far south next to Antarctica. The
1268 observation-based analyses generally agree that the region south of Australia is warming,
1269 as is the high latitude South Atlantic. However, Domingues et al. (2008) shows a strong
1270 cooling in the Indian sector of the Southern Ocean missing from other observation-based
1271 analyses and CORE-II, whereas both Domingues et al. (2008) and Durack and Wijffels
1272 (2010) show cooling in the South Pacific sector that is marginal at best in the CORE-II
1273 simulations and largely missing in Levitus et al. (2012).
- 1274 We suspect that much of the observation-observation and model-observation ambivalence
1275 in the Southern Ocean arises from the relative paucity of *in situ* data and uncertainties in
1276 the CORE-II atmospheric state of Large and Yeager (2009).
- 1277 • ARCTIC: The CORE-II simulations suggest a marginal cooling in the Arctic, whereas Lev-
1278 itus et al. (2012) suggests a marginal warming. The other observation-based analyses do
1279 not cover the Arctic.
- 1280 • ZONAL MEAN: Besides the deep warming in the North Atlantic for CORE-II, Levitus et al.
1281 (2012), and Durack and Wijffels (2010), there is a broad warming in the upper 700 m
1282 throughout the ocean. However, there is a patch of cooling in the tropical northern hemi-
1283 sphere found in CORE-II that is marginally present in Durack and Wijffels (2010) but
1284 largely absent in Levitus et al. (2012). The CORE-II simulations indicate a marginally
1285 cooler Southern Ocean, which contrasts to the marginally warmer analysis from Levitus
1286 et al. (2012).

1287 6.4. Summary of dynamic sea level patterns

1288 All of the CORE-II simulations considered here produce a respectable time mean dynamic
1289 sea level as compared to the 1993-2007 satellite measurements analyzed by AVISO (Figure 15).
1290 However, consistent with other assessments, such as Lombard et al. (2009) (see their Figure 2)
1291 and Church et al. (2010) (see their Figure 6.3), the simulations here produce larger differences
1292 from satellite measurements in the high latitudes, particularly in the Atlantic basin and Southern
1293 Ocean. In general, those regions exhibiting deep water formation, mode water formation, and
1294 strong western boundary currents, display larger sea level deviations from satellites (Figure 16).
1295 We suggest that these differences point to limitations of the models associated with the rather
1296 complex physical processes associated with mode and deep water formation and boundary cur-
1297 rents. We do not have a suite of simulations where only the model resolution is varied, so we
1298 cannot make robust statements regarding the ability of refined resolution models to more accu-
1299 rately represent sea level at both the regional and global scales. Such represents an important
1300 ongoing aspect of developing models with skill at regional scales. In general, we acknowledge
1301 that some differences can arise from processes not simulated in the CORE-II models, such as
1302 changes to the gravity field impacting the static equilibrium sea level (Kopp et al., 2010).

1303 As shown in Figure 18 for the full suite of CORE-II simulations, and summarized in Figure
1304 33 for just the ensemble mean, the simulations exhibit dynamic sea level trends over the years
1305 1993-2007 that reflect certain features also found in the satellite-based analysis. We highlight
1306 here some of the agreements and disagreements.

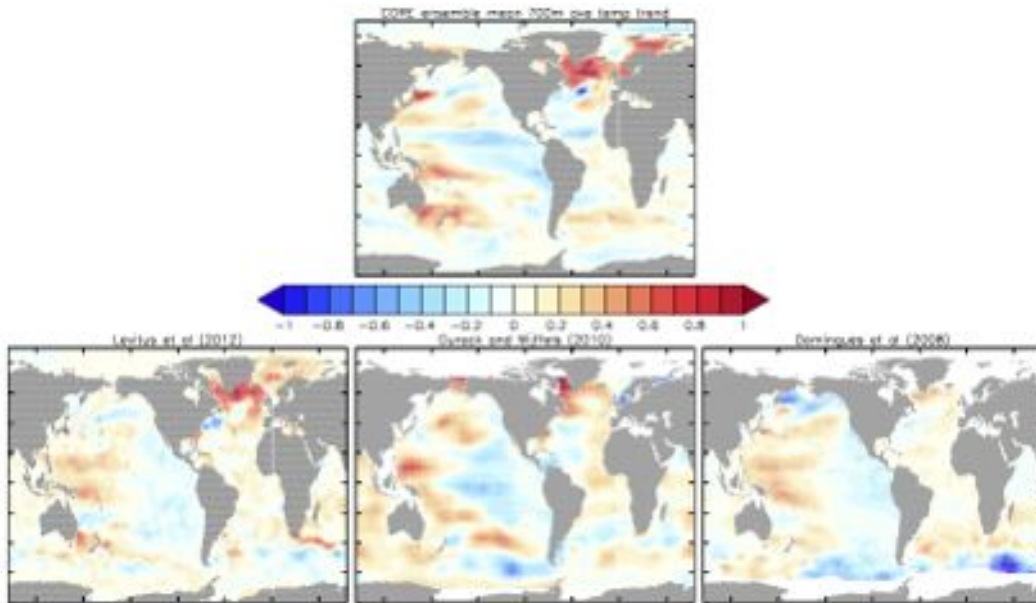


Figure 31: Linear trend in annual mean ocean temperature as vertically averaged over the upper 700 m of ocean (units $^{\circ}\text{C decade}^{-1}$) for the years 1993-2007, computed from the ensemble mean of the simulations over the fifth CORE-II cycle. Also shown is the corresponding observation-based trends over years 1993-2007 from Levitus et al. (2012); an updated analysis from Domingues et al. (2008) and Church et al. (2010); along with the trend over years 1990-2010 using an updated version of Durack and Wijffels (2010). This trend is quite similar to that shown in Figure 13 for the heat content shown there for each of the simulations as well as the CORE-II ensemble mean. The spatial correlation between the CORE ensemble mean and the observational analyses is given by CORE-Levitus=0.45, CORE-Domingues=0.33, CORE-Durack=0.28.

- 1307 • **PACIFIC:** The models exhibit a rise in the western Pacific and fall in the eastern Pacific.
 1308 Mechanisms for these changes in dynamic sea level are consistent with hypotheses put
 1309 forward in the literature as associated with wind trends (Feng et al., 2010; Bromirski
 1310 et al., 2011; Merrifield et al., 2012; McGregor et al., 2012; Zhang and Church, 2012) (see
 1311 Figures 28 and 29). However, the westward extent and magnitude of the sea level depres-
 1312 sion in the east is larger in CORE-II than the satellite, perhaps suggesting limitations with
 1313 the CORE-II wind stress forcing.
- 1314 Both the CORE-II mean and satellite indicate a sea level drop in the North Pacific, ex-
 1315 tending into the Arctic sector just north of the Bering Strait. Both also indicate a rise in
 1316 the Kuroshio region of the west Pacific.
- 1317 • **ATLANTIC:** Both CORE-II and satellites indicate a sea level rise in the subpolar North At-
 1318 lantic, with these changes associated with a switch in the North Atlantic Oscillation around
 1319 1995/1996 and the attendant impact from ocean meridional heat and salt transport into the
 1320 subpolar region (Häkkinen and Rhines, 2004; Lohmann et al., 2009; Yeager et al., 2012;
 1321 Danabasoglu et al., 2014). There is an associated dipole pattern in sea level trends found

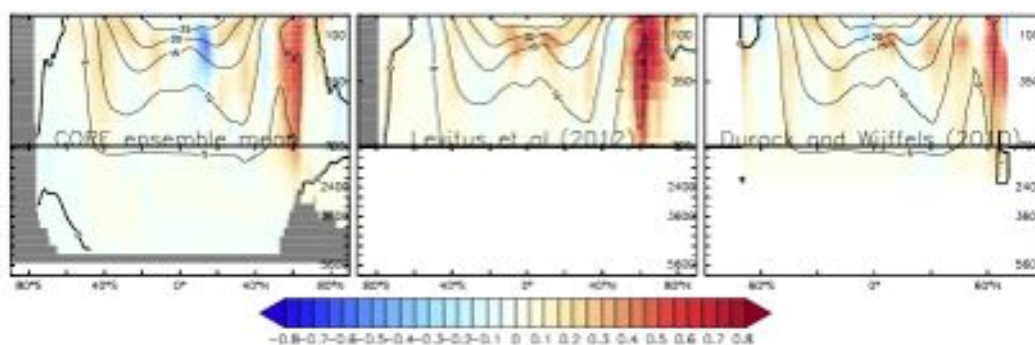


Figure 32: Zonal average of the linear trend in annual mean ocean temperature (deg C decade^{-1}) for the years 1993-2007 as computed from the CORE-II ensemble mean over the fifth CORE-II cycle. Also shown are two estimates of the observation-based trends. Overlaying the trends are contours for the time mean temperature computed from each respective model and observation-based analysis. The upper 700 m of the ocean is split from the deeper ocean to emphasize changes in the upper ocean. The images are computed by first mapping the 3d model results to a common spherical grid with a common vertical spacing, and then performing the zonal average.

1322 along the east coast of the US, with recent altimetry and tide gauge data suggesting that the
 1323 pattern is switching to one with a faster sea level rise north of Cape Hatteras, and slower
 1324 sea level rise to the south (Yin and Goddard, 2013; Kopp, 2013). These studies suggest
 1325 that the decadal trend of the dynamic sea level in the North Atlantic is not representative
 1326 of the long-term, with trends quite different over the years 1993-2002 versus 2003-2012.
 1327 One should thus keep this point in mind when comparing our results to previous studies.

1328 • **INDIAN:** Both the CORE-II ensemble mean and satellite indicate a sea level rise in the South
 1329 Atlantic and extending eastward into the South Indian Ocean. The trend in the Indian
 1330 Ocean extends eastward from Madagascar. However, the satellite measures indicate a sea
 1331 level fall in the North Indian Ocean during 1993-2007, whereas CORE-II indicates a rise.

1332 • **SOUTHERN OCEAN:** A notable disagreement between models and satellite occurs in the
 1333 Southern Ocean south of Australia, where the models generally show a decreasing sea
 1334 level trend whereas the satellite shows a positive trend. This region is also one where
 1335 the observation-based analysis of thermosteric sea level trends differs (Figure 34), where
 1336 Levitus et al. (2012) shows a marginally negative trend whereas Domingues et al. (2008)
 1337 and Durack and Wijffels (2010) show a positive trend. We suspect that much of the
 1338 observation-observation and model-observation disagreement in this region arises from
 1339 the relative paucity of *in situ* data and uncertainties in the CORE-II atmospheric state of
 1340 Large and Yeager (2009).

1341 • **ARCTIC:** Changes in the Arctic found in the CORE-II simulations are largely associated
 1342 with halosteric changes, as summarized in Section 6.5. Unfortunately, they are missing
 1343 from the satellite measurements due to coverage limitations.

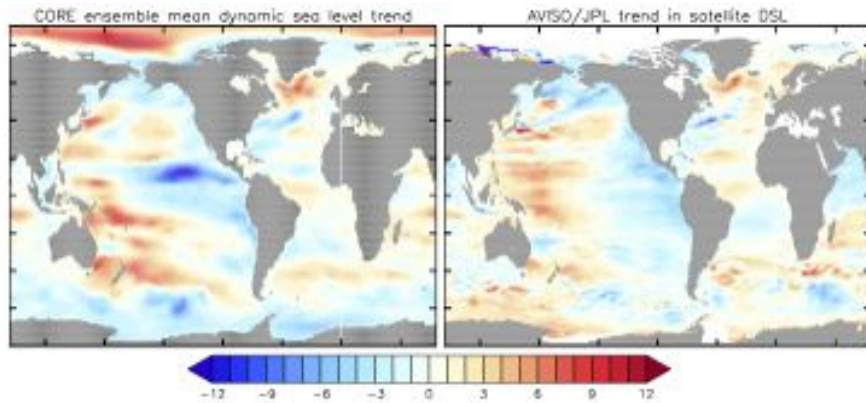


Figure 33: Linear trend in annual mean dynamic sea level (mm yr^{-1}) for the years 1993-2007 as computed from the ensemble mean of the CORE-II simulations over the fifth CORE-II cycle. Also shown are observation-based estimates of the trend based on satellite measurements (between roughly $60^\circ N - 60^\circ S$). The JPL sea level field was obtained from AVISO, and downloaded from `podaac.jpl.nasa.gov/dataset/AVISO_L4_DYN_TOPO_1DEG_1MO`. The full suite of simulations is presented in Figure 18. The spatial correlation between the CORE ensemble mean and the satellite analysis is 0.40.

1344 6.5. Summary of steric sea level patterns

1345 Trends in dynamic sea level can be decomposed into steric and bottom pressure changes,
 1346 according to the method proposed by Gill and Niiler (1973) (see equation (13) as well as Ap-
 1347 pendix B1). The dynamic sea level trends from the CORE-II simulations are dominated by steric
 1348 changes (Figure 19), with changes in bottom pressure about an order of magnitude smaller (Fig-
 1349 ure 20).

1350 Local changes in steric sea level can in turn be decomposed into thermosteric and halosteric
 1351 changes (Appendix B1.2). Thermosteric effects (Figure 22) are generally larger than halosteric
 1352 effects (Figure 23), with notable exceptions being the Arctic and subpolar North Atlantic. We
 1353 provide a discussion of these patterns in Section 5.3.

1354 When limiting the analysis of steric trends to just the upper 700 m of the ocean, we are
 1355 able to compare the CORE-II simulations to various observation-based analyses, in addition to
 1356 the Durack and Wijffels (2010) analysis that extends to 2000 dbar. As discussed in Section
 1357 2.8, the Durack and Wijffels (2010) analysis offers both temperature and salinity trends, and so
 1358 can render an estimate of trends for steric, thermosteric, and halosteric sea level changes. The
 1359 Domingues et al. (2008) and Levitus et al. (2012) analyses focus on temperature changes, and
 1360 so allow an estimate only for thermosteric changes. We exhibit results from the full suite of
 1361 CORE-II simulations in Figures 25, 26, and 27. A summary of the results for the thermosteric
 1362 trends is given in Figure 34, and halosteric trends in Figure 35. Discussion of the agreements
 1363 and disagreements for thermosteric patterns follow largely from those already considered for
 1364 dynamic sea level in Section 6.4 and temperature trends in Section 6.3.

1365 The halosteric trends are generally sub-dominant to the thermosteric trends, with important
 1366 exceptions found in the North Atlantic, where they are comparable and counteract the ther-
 1367 mal effects, and in the Arctic, where they are the dominant contributor in the CORE-II simula-

1368 tions. Unfortunately, there are no observation-based analyses providing estimates for the Arctic
 1369 halosteric trends. For the remainder of the ocean, the CORE-II ensemble mean and Durack and
 1370 Wijffels (2010) analysis suggest rather striking and complex trend patterns. However, many el-
 1371 ements of these trend patterns do not agree well. As discussed in Section 3, we are unconvinced
 1372 that details of the simulated halosteric patterns are physically meaningful since the CORE-II
 1373 simulations use surface salinity relaxation of varying strength between the models, with such
 1374 relaxation having no counterpart in the climate system (see Section 3 of Griffies et al., 2009b).
 1375 This is an unfortunate limitation of the CORE-II design.

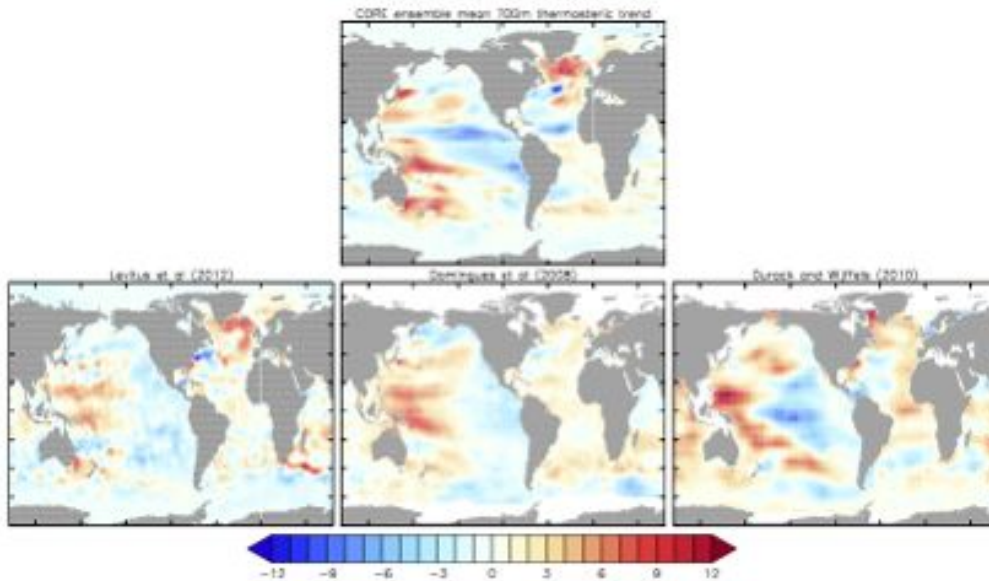


Figure 34: Linear trend (mm yr^{-1}) in thermosteric sea level computed in the upper 700 m of water for years 1993-2007. The model results are taken from the ensemble mean of the 5th CORE-II cycle. Observation-based estimates are shown from Levitus et al. (2012); an updated analysis of Domingues et al. (2008) and Church et al. (2010); and an updated analysis based on Durack and Wijffels (2010). Results from the full suite of CORE-II simulations are shown in Figure 26. The spatial correlation between the CORE ensemble mean and the observational analyses is given by CORE-Levitus=0.31, CORE-Domingues=0.43, CORE-Durack=0.31.

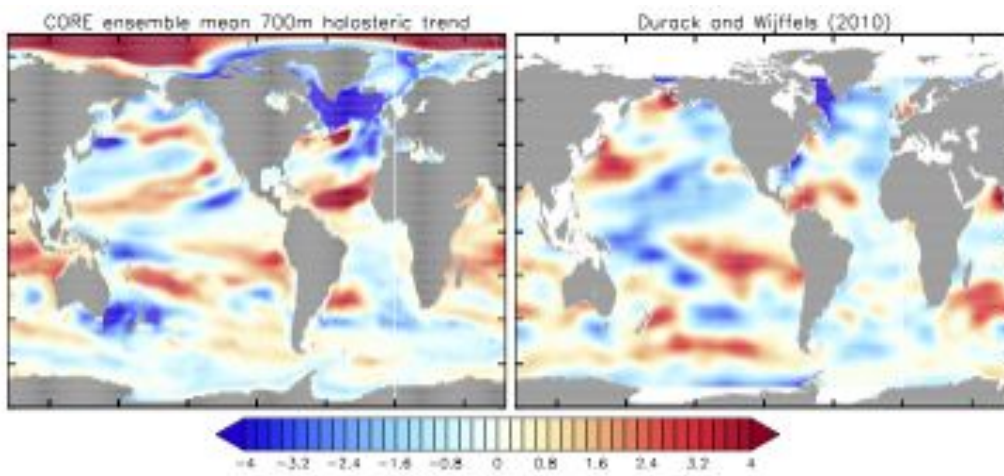


Figure 35: Linear trend (mm yr^{-1}) in halosteric sea level computed in the upper 700 m of water for years 1993-2007. The model results are taken from the ensemble mean of the 5th CORE-II cycle. Observation-based estimates are shown from an updated analysis based on Durack and Wijffels (2010). Results from the full suite of CORE-II simulations are shown in Figure 27. We exhibit here a smaller color bar range than in other steric trend figures (e.g., Figure 27) in order to better highlight the patterns. The spatial correlation between the CORE ensemble mean and the Durack and Wijffels (2010) observational analysis is 0.18.

1376 *6.6. Closing comments*

1377 Details certainly do differ amongst the suite of models, and we do not presume all details are
1378 correct either from the models or from the observation-based analyses. Furthermore, we cannot
1379 expect perfect agreement between models and observation-based analyses, particularly given the
1380 coarseness in the models, the limitations of the Large and Yeager (2009) CORE-II atmospheric
1381 state, the many holes in the observation-based analyses, and the additional processes impact-
1382 ing sea level that are missing from the simulations (e.g., gravitational and rotational effects).
1383 Nonetheless, we are satisfied that the CORE-II simulations, particularly in the upper 700 m of
1384 the ocean, are responding to the CORE-II atmospheric state in a consistent manner. Further-
1385 more, the ensemble mean of the CORE-II simulations exhibits trends in both global mean and
1386 regional patterns generally within the spread of the observation-based analyses.

1387 Although we answered the questions posed at the start of this paper concerning global mean
1388 and regional patterns (Section 1.1), it is difficult to reach the end of an assessment paper such as
1389 this without a list of questions longer than at the start. In a nutshell, our assessment is that the
1390 CORE-II simulations are not inconsistent, at the larger scales, with a suite of observation-based
1391 analyses. Breaking open that nut, however, reveals many facets to the comparison that remain
1392 unanswered. Namely, can we explain details of how thermosteric and halosteric patterns differ
1393 amongst the models or in comparison to the observations, particularly at the regional scale? One
1394 piece required to answer these questions sits with forcing differences. Even though the CORE-II
1395 protocol aims to reduce such differences, the open-ended treatment of salinity boundary con-
1396 ditions leads to differences in the halosteric effects. Although halosteric effects were found to
1397 be sub-dominant to thermosteric effects in many regions, there are notable exceptions such as
1398 in the Arctic, where halosteric effects dominate, and North Atlantic, where they largely com-
1399 pensate for the strong thermosteric rise. We consider the absence of a robust statement about
1400 halosteric patterns, particularly in the lower latitudes, to be a notable weakness of the CORE-II
1401 protocol.

1402 We suspect that a further key reason for model differences concerns physical and numerical
1403 formulations of the various ocean model configurations, with sea ice model differences con-
1404 jectured to be less important. We note that there are opportunities for parameterization and/or
1405 numerical choices within a single model code to contribute to substantial differences in sea level
1406 patterns and global mean trends. For example, the NOCS and CERFACS models are based on
1407 the same ocean and sea ice model, but differ in ocean physical parameterizations. More gener-
1408 ally, studies of vertical ocean mixing, both physically motivated as in MacKinnon et al. (2013)
1409 and numerically induced as in Griffies et al. (2000), provide examples where physical parame-
1410 terizations and numerical choices impact on heat uptake, with attendant impacts on model drift
1411 and hence on simulations of sea level. Parameterization and/or representation of mesoscale ed-
1412 dies (Fox-Kemper et al., 2013) also play a potentially important role in determining regional sea
1413 level patterns.

1414 We contend that a physical process-based analysis is needed on a model-by-model basis
1415 to uncover mechanisms accounting for model differences. Examples include the analysis of
1416 Griffies and Greatbatch (2012), who decomposed the global mean sea level budget, as well as
1417 that from Palter et al. (2014), who decomposed the local steric sea level budget. Such analyses
1418 are nontrivial to perform with a single model. They are logistically even more difficult across a

1419 broad suite of models such as considered here. Nonetheless, we expect that significant progress
1420 will be made to understand model-model differences only when detailed budget analyses are
1421 performed at the level of specific physical processes. We hope that the present paper provides a
1422 useful starting point for such studies.

1423 We close this paper by commenting on the potential for more intimate interactions between
1424 CORE and CMIP. As discussed in Section 2.1, there are important differences between CORE
1425 (coupled ocean / sea ice models with prescribed atmospheric state) and CMIP (fully coupled
1426 climate models). The complementary aspects of the two efforts foster independent questions and
1427 methods, all of which supports the scientific value of ocean and climate modelling. However,
1428 we contend that more interaction between the two communities would prove of value as well,
1429 particularly now that CORE simulations are becoming a *de facto* community standard for vetting
1430 global ocean-sea ice models in a manner akin to AMIP (Atmospheric Model Intercomparison
1431 Project) (Gates, 1993). Do biases in CORE simulations transfer into coupled climate models
1432 using the same ocean and sea ice models as components? Are CORE simulations a necessary
1433 and/or sufficient means of benchmarking ocean / sea ice models used as part of CMIP coupled
1434 climate models? Answering these questions requires a new phase in the CORE process, whereby
1435 thorough comparisons of model behaviour in “CORE-mode” versus “coupled climate mode”
1436 are considered. Preliminary ideas are being contemplated within the community of ocean and
1437 climate modellers. We trust that future papers will document results from such deliberations.

1438 *Acknowledgements*

1439 The WCRP/CLIVAR Working Group on Ocean Model Development (WGOMD) is respon-
1440 sible for organizing the Coordinated Ocean-sea ice Reference Experiments. The conceptual and
1441 technical details associated with global ocean-sea ice model comparisons have comprised the
1442 majority of the group’s deliberations since its inception in 1999. We thank Anna Pirani from the
1443 CLIVAR staff for her tireless and gracious support of WGOMD activities.

1444 Much of the analysis in this paper made use of the free software package Ferret, developed at
1445 NOAA-PMEL. We thank Frank Bryan, Carolina Dufour, Matthew England, Andy Hogg, Robert
1446 Kopp, Angelique Melet, and Ron Stouffer for comments and discussions that have greatly helped
1447 this paper. We thank Christophe Cassou for comments on the possible effects from wind errors
1448 in their relation to biases in equatorial Pacific sea level patterns. Finally, we thank the critical
1449 input from three anonymous reviewers.

1450 NCAR is sponsored by the US National Science Foundation. The ACCESS model is sup-
1451 ported by the Australian Government Department of the Environment, the Bureau of Meteo-
1452 rology and CSIRO through the Australian Climate Change Science Programme. E. Fernandez
1453 was supported by the BNP-Paribas foundation via the PRECLIDE project under the CNRS re-
1454 search convention agreement 30023488. P.J. Durack was supported by Lawrence Livermore
1455 National Laboratory, which is funded by the U.S. Department of Energy under contract DE-
1456 AC52-07NA27344. A.M. Treguier acknowledges support of the European Commission’s 7th
1457 Framework Programme, under Grant Agreement number 282672, EMBRACE project.

1458 Appendix A: Global mean sea level

1459 We summarize in this appendix basic elements of the kinematic evolution of the sea surface
1460 height (SSH), with particular attention given to how the global mean sea level is impacted by
1461 steric effects. There are two basic assumptions made here, consistent with the models considered
1462 in this study.

- 1463 • **CONSTANT GRAVITATIONAL ACCELERATION:** The gravitational acceleration is assumed to be con-
1464 stant in space and time. Hence, the issues associated with changes in the geoid or earth
1465 rotation (Mitrovica et al., 2001; Kopp et al., 2010) are ignored.
- 1466 • **CONSTANT HORIZONTAL AREA OF OCEAN:** The ocean is assumed to have a time independent
1467 horizontal area, so that questions of wetting and drying, important for coastal erosion
1468 studies and changes to ice shelf grounding lines, are not captured by the ocean models in
1469 this study.

1470 A1. Mass continuity and the kinematic evolution of sea level

1471 We start by considering the equation for mass conservation of a fluid parcel

$$\frac{1}{\rho} \frac{d\rho}{dt} = -\nabla \cdot \mathbf{v}, \quad (14)$$

1472 where $\mathbf{v} = (\mathbf{u}, w)$ is the three dimensional velocity of a fluid parcel, \mathbf{u} the horizontal component
1473 and w the vertical, and $d\rho/dt$ is the material time evolution of *in situ* density. Integration of mass
1474 conservation over the full depth of an ocean column, with use of the surface ($z = \eta(x, y, t)$) and
1475 bottom ($z = -H(x, y)$) kinematic boundary conditions, renders the kinematic sea level equation

$$\frac{\partial \eta}{\partial t} = \frac{Q_m}{\rho(\eta)} - \nabla \cdot \mathbf{U} - \int_{-H}^{\eta} \frac{1}{\rho} \frac{d\rho}{dt} dz. \quad (15)$$

1476 In this equation, $\eta(x, y, t)$ is the sea surface height (SSH) that measures the height of the ocean
1477 free surface above the $z = 0$ geoid;

$$\mathbf{U} = \int_{-H}^{\eta} \mathbf{u} dz \quad (16)$$

1478 is the vertically integrated horizontal velocity that measures the horizontal volume transport
1479 through a column of fluid; $\rho(\eta) = \rho(x, y, z = \eta(x, y, t), t)$ is the liquid seawater density at the
1480 ocean free surface, and Q_m is the material mass per time per horizontal area entering the ocean
1481 through the surface boundary. There has been no dynamical assumption made to derive the sea
1482 surface height equation (15). Instead, it follows solely from the kinematics of a mass conserving
1483 fluid.

1484 Equation (15) provides a kinematic partition of SSH evolution into three physical processes:

- 1485 • **MASS:** boundary fluxes of mass associated with precipitation, evaporation, river runoff, and
1486 land ice melt;

1487 • CURRENTS: the convergence of vertically integrated currents, which act to redistribute vol-
 1488 ume without altering the global mean sea level;

1489 • NON-BOUSSINESQ STERIC: vertically integrated material changes in the ocean *in situ* density,
 1490 referred to as the non-Boussinesq steric effect by Griffies and Greatbatch (2012).

1491 When taking a global mean, it is only the mass term and non-Boussinesq steric term that con-
 1492 tribute to global mean SSH evolution

$$\partial_t \bar{\eta} = \overline{\left(\frac{Q_m}{\rho(\eta)} \right)} - \overline{\left(\int_{-H}^{\eta} \frac{1}{\rho} \frac{d\rho}{dt} dz \right)}, \quad (17)$$

1493 where a global area mean is given by

$$\bar{\eta} = \mathcal{A}^{-1} \int_{\text{globe}} \eta \, dA, \quad (18)$$

1494 with horizontal integration over the global ocean surface. The global ocean surface area, $\mathcal{A} =$
 1495 $\int_{\text{globe}} dA$, is assumed to be constant, and dA is the horizontal area element (equal in a numerical
 1496 model to the grid cell horizontal area). Equation (17) is the form of the global mean sea level
 1497 equation examined by Griffies and Greatbatch (2012), with their focus on how physical pro-
 1498 cesses impact on the global mean non-Boussinesq steric effect. However, when detailed online
 1499 diagnostics are not available, it is more practical to employ the alternative partition of global
 1500 mean SSH evolution as presented in Section A2.

1501 The non-Boussinesq steric effect arises from the impacts on SSH evolution due to material
 1502 changes in ocean *in situ* density. In particular, a material reduction in density over the depth
 1503 of a fluid column leads to an increase in SSH due to the expansion of the water column. This
 1504 term is dropped when determining the evolution of sea surface height, η^B , in volume conserving
 1505 Boussinesq ocean simulations, whereby

$$\frac{\partial \eta^B}{\partial t} = \frac{Q_m}{\rho_o} - \nabla \cdot \mathbf{U}. \quad (19)$$

1506 This equation results from volume conservation for a column of Boussinesq fluid, which con-
 1507 trasts to the evolution of SSH given by equation (15) arising from mass conservation. The use of
 1508 volume conserving kinematics in Boussinesq fluids is accurate for many applications of ocean
 1509 climate modelling, where the relatively small degree of seawater compressibility can be safely
 1510 ignored for kinematic purposes. For example, the large-scale patterns of SSH from both volume
 1511 conserving and mass conserving ocean models is quite similar (e.g., see Figure 3 in Griffies and
 1512 Greatbatch (2012)). However, it is through the non-Boussinesq steric effect that global mean
 1513 SSH rises through ocean warming (Greatbatch, 1994). Griffies and Greatbatch (2012) detail a
 1514 global adjustment to the Boussinesq SSH that renders it more consistent with the non-Boussinesq
 1515 SSH (see their Appendix D), with a summary provided here in Section A3.

1516 **A2. Global steric effects and the evolution of global mean sea level**

1517 The global ocean liquid seawater mass is given by

$$\mathcal{M} = \int dA \int_{-H}^{\eta} \rho dz, \quad (20)$$

1518 and the corresponding expression for the global ocean volume is

$$\mathcal{V} = \int dA \int_{-H}^{\eta} dz = \int (H + \eta) dA, \quad (21)$$

1519 so that the global mean *in situ* seawater density is

$$\langle \rho \rangle = \frac{\mathcal{M}}{\mathcal{V}}. \quad (22)$$

1520 Time evolution of the global ocean mass is thus written as

$$\partial_t \mathcal{M} = \langle \rho \rangle \partial_t \mathcal{V} + \mathcal{V} \partial_t \langle \rho \rangle. \quad (23)$$

1521 The global ocean mass changes due to the input of mass through the ocean boundaries, so that

$$\partial_t \mathcal{M} = \mathcal{A} \overline{Q_m}, \quad (24)$$

1522 where $\overline{Q_m}$ is the global area mean surface mass flux. The global ocean volume changes due to
1523 changes in the global mean ocean free surface (assuming the ocean bottom remains constant)

$$\partial_t \mathcal{V} = \mathcal{A} \partial_t \bar{\eta}. \quad (25)$$

1524 Use of these expressions in the mass budget (23) thus leads to an evolution equation for the
1525 global mean sea level

$$\partial_t \bar{\eta} = \frac{\overline{Q_m}}{\langle \rho \rangle} - \frac{\mathcal{V}}{\mathcal{A}} \left(\frac{1}{\langle \rho \rangle} \frac{\partial \langle \rho \rangle}{\partial t} \right). \quad (26)$$

1526 As expected, if the global mean *in situ* density decreases, the global mean sea level rises. We
1527 refer to the term

$$\left(\frac{\partial \bar{\eta}}{\partial t} \right)^{\text{global steric}} \equiv - \frac{\mathcal{V}}{\mathcal{A}} \left(\frac{1}{\langle \rho \rangle} \frac{\partial \langle \rho \rangle}{\partial t} \right) \quad (27)$$

1528 as the global steric contribution to global mean sea level evolution. This term is absent from the
1529 evolution of the prognostic sea level in Boussinesq ocean models (Greatbatch, 1994). Appendix
1530 D in Griffies and Greatbatch (2012) detail some straightforward adjustments required to measure
1531 global mean sea level in Boussinesq models, with salient points also provided in Section A3
1532 below.

1533 Equation (26) is more convenient for model comparison diagnostics than the alternative
1534 equation (17). The reason is that it is more convenient to work with time tendencies of global
1535 mean density, which is readily computed from model output, than the global mean of the material
1536 time change, which requires more terms than generally available from model output. Hence, we
1537 make use of the evolution equation (26) in our studies of the CORE-II simulations in Section 3.

1538 A3. Approximations for diagnosing global mean sea level changes in CORE-II simulations

1539 Although there are exceptions, the CORE-II simulations considered in this paper are de-
 1540 signed to have a zero net mass/volume flux crossing the ocean surface (Griffies et al., 2009b).
 1541 The one exception is the relatively small exchanges associated with sea ice melt and formation,
 1542 with such phase changes leaving the effective global mean sea level unchanged, as a result of the
 1543 inverse barometer response of the liquid ocean to sea ice loading (see Appendix C2 in Griffies
 1544 and Greatbatch (2012)). Hence, global mean sea level for our purposes changes only through
 1545 changes in global mean seawater density, in which case equation (26) takes the form

$$\partial_t \bar{\eta} = -\frac{\mathcal{V}}{\mathcal{A}} \left(\frac{1}{\langle \rho \rangle} \frac{\partial \langle \rho \rangle}{\partial t} \right). \quad (28)$$

1546 This continuous time relation is approximated by

$$\bar{\eta}(t) - \bar{\eta}(t-1) \approx -\left(\frac{\mathcal{V}(0)}{\mathcal{A} \langle \rho(0) \rangle} \right) (\langle \rho(t) \rangle - \langle \rho(t-1) \rangle), \quad (29)$$

1547 in which time evolution is computed as a finite difference, and where $\langle \rho(0) \rangle$ is the initial global
 1548 ocean seawater *in situ* density, and $\mathcal{V}(0)$ is the initial global ocean volume. The diagnostics
 1549 presented in this paper use annual means for the global mean *in situ* density. Sensitivity to this
 1550 time average has been found to be negligible with tests using the GFDL-MOM configuration.

1551 A4. Global mean ocean temperature

1552 Globally integrated ocean heat content (SI units of Joules) is given by

$$\mathcal{H} = C_p^0 \mathcal{V} \langle \rho \Theta \rangle = C_p^0 \mathcal{M} \langle \Theta \rangle^\rho, \quad (30)$$

1553 where

$$\langle \Theta \rangle^\rho = \frac{\langle \rho \Theta \rangle}{\langle \rho \rangle} \quad (31)$$

1554 introduces a density weighted mean temperature. Note that the *in situ* density weighting in these
 1555 equations reduces, for a Boussinesq fluid, to a constant reference density ρ_o weighting. The
 1556 specific heat capacity of sea water, C_p^0 , is assumed to be constant here for the various models.
 1557 However, as noted by McDougall (2003) (see also IOC et al. (2010)), use of a constant spe-
 1558 cific heat capacity is accurately justified only when the temperature variable is the conservative
 1559 temperature rather than the commonly used potential temperature.

1560 It follows from the definition (30) that the total ocean heat changes according to changes in
 1561 the mean temperature and the ocean mass

$$\frac{\partial_t \mathcal{H}}{\mathcal{H}} = \frac{\partial_t \langle \Theta \rangle^\rho}{\langle \Theta \rangle^\rho} + \frac{\partial_t \mathcal{M}}{\mathcal{M}}. \quad (32)$$

1562 As heat (or more correctly potential enthalpy) is a conserved quantity in the ocean (McDougall,
 1563 2003), we know that the net ocean heat changes only via the net heat flux crossing the liquid
 1564 ocean surface, in which we write

$$\partial_t \mathcal{H} = \mathcal{A} \overline{Q^{\text{heat}}}. \quad (33)$$

1565 The term $\mathcal{A} \overline{Q^{\text{heat}}}$ is the area integrated boundary heat flux (SI units of Watts). This heat flux
 1566 includes the surface fluxes from shortwave, longwave, latent, and sensible heating, as well as
 1567 exchanges with sea ice (see Section 3.4.1 of Griffies and Greatbatch (2012)). Some models
 1568 also include geothermal heating. We denote the sum of these terms the non-advective heat flux,
 1569 $Q_{\text{non-advect}}^{\text{heat}}$. In addition, the ocean heat content changes when mass is exchanged, since the mass
 1570 will carry a nonzero heat across the ocean boundary, so that the total heat flux is the sum

$$Q^{\text{heat}} = Q_{\text{non-advect}}^{\text{heat}} + Q_{\text{advect}}^{\text{heat}}. \quad (34)$$

1571 The advective surface heat flux for CORE simulations is typically approximated by

$$Q_{\text{advect}}^{\text{heat}} \approx Q_m C_p^0 T_{\text{sst}}, \quad (35)$$

1572 where C_p^0 is the ocean heat capacity, Q_m is the mass transport across the ocean boundary, and T_{sst}
 1573 is the sea surface *in situ* temperature. If $Q_{\text{advect}}^{\text{heat}}$ is not diagnosed online with each time step, it is of
 1574 sufficient accuracy for CORE diagnostics to estimate it with the monthly mean mass flux multi-
 1575 plying the monthly mean sea surface temperature. Use of annual means to approximate $Q_{\text{advect}}^{\text{heat}}$ is
 1576 not accurate due to the importance of the seasonal cycle. In the real climate system, evaporation
 1577 generally leaves the ocean in regions of warmer sea surface temperature than precipitation, thus
 1578 leading to a negative area mean $Q_{\text{advect}}^{\text{heat}}$. In the coupled model study of Delworth et al. (2006) (see
 1579 their Section 3), they find $Q_{\text{advect}}^{\text{heat}} \approx -0.15 \text{ W m}^{-2}$. For the CORE-II simulations considered here,
 1580

$$Q_{\text{advect}}^{\text{heat}} \approx -0.3 \text{ W m}^{-2}. \quad (36)$$

1581 Finally, we note that those models that use a virtual salt flux rather than a real water flux (see
 1582 Table 1) necessarily have

$$Q_{\text{advect}}^{\text{heat}} = 0 \quad \text{if } Q_m = 0. \quad (37)$$

1583 Substitution of equations (33) and (24) into equation (32) leads to an expression for the
 1584 evolution of global mean ocean temperature

$$\frac{\partial \langle \Theta \rangle^\rho}{\partial t} = \mathcal{A} \left(\frac{\overline{Q^{\text{heat}}}}{\mathcal{H}} - \frac{\overline{Q_m}}{\mathcal{M}} \right). \quad (38)$$

1585 Use of expression (30) for the heat content leads to

$$\frac{\partial \langle \Theta \rangle^\rho}{\partial t} = \frac{\mathcal{A}}{C_p \mathcal{M}} \left(\overline{Q^{\text{heat}}} - C_p \langle \Theta \rangle^\rho \overline{Q_m} \right). \quad (39)$$

1586 Finally, we substitute the advective heat flux (35) to render

$$\frac{\partial \langle \Theta \rangle^\rho}{\partial t} = \frac{\mathcal{A}}{C_p \mathcal{M}} \left(\overline{Q_{\text{non-advect}}^{\text{heat}}} + C_p \overline{Q_m \Theta_{\text{sst}}} - C_p \langle \Theta \rangle^\rho \overline{Q_m} \right). \quad (40)$$

1587 It remains very accurate for global models to set the mass term \mathcal{M} to a constant, since its relative
 1588 change is tiny. For those CORE simulations where the global mean ocean mass flux is nonzero
 1589 only due to exchanges with sea ice, the term $C_p \langle \Theta \rangle^\rho \overline{Q_m}$ is far smaller than the non-advective
 1590 and advective heat fluxes $\overline{Q_{\text{non-advect}}^{\text{heat}}} + C_p \overline{Q_m \Theta_{\text{sst}}}$.

1591 **A5. Global mean sea level and global mean boundary heating**

1592 Global mean steric sea level is dominated by global mean temperature, with this dominance
 1593 understood by considering how global mean density evolves. For this purpose, recall the *in situ*
 1594 density is a function of temperature (potential or conservative temperature are used in ocean
 1595 models), salinity, and pressure

$$\rho = \rho(\Theta, S, p). \quad (41)$$

1596 We assume that the time evolution of global mean density can be written (we comment on this
 1597 assumption at the end of the section)

$$\partial_t \ln \langle \rho \rangle = -\alpha_{\text{bulk}} \partial_t \langle \Theta \rangle^\rho + \beta_{\text{bulk}} \partial_t \langle S \rangle^\rho + \frac{\partial_t \langle p \rangle^\rho}{(\rho c^2)_{\text{bulk}}}. \quad (42)$$

1598 This expression is only approximate, due to nonlinearities in the equation of state. We consider it
 1599 to be a physically relevant expression *if* the linear expansion coefficients correspond to physically
 1600 relevant values for a bulk thermal expansion coefficient (α_{bulk}), haline contraction coefficient
 1601 (β_{bulk}), and density times the squared sound speed ($(\rho c^2)_{\text{bulk}}$).

1602 For the majority of the CORE-II simulations considered in this paper, the liquid ocean salt
 1603 content is nearly constant since the only exchanges are associated with either melting and freez-
 1604 ing of sea ice, or through the surface salinity restoring, which is normalized to zero globally
 1605 in most of the simulations. Since the ocean mass is also nearly constant, changes in the global
 1606 mean salinity are negligible. Pressure effects in equation (42) are likewise relatively small. The
 1607 reason is that in a hydrostatic fluid, pressure at a depth equals to the mass per horizontal area of
 1608 liquid above that depth. So unless there is a systematic rearrangement of mass in the ocean, we
 1609 expect the horizontal area averaged pressure at each depth to remain roughly unchanged, thus
 1610 leading to global averaged pressure remaining roughly unchanged. Figure 36 exhibits the terms
 1611 appearing in equation (42) for the GFDL-MOM simulation, thus verifying the above empha-
 1612 sis on mean temperature evolution for determining global mean sea level changes due to steric
 1613 effects.

1614 We conclude that for our purposes, the global mean density changes are dominated by global
 1615 mean potential or conservative temperature changes. Correspondingly, the global mean steric sea
 1616 level equation (28) takes on the approximate form

$$\frac{\partial \bar{\eta}}{\partial t} \approx \left(\frac{\mathcal{V} \alpha_{\text{bulk}}}{\mathcal{A}} \right) \frac{\partial \langle \Theta \rangle^\rho}{\partial t}. \quad (43)$$

1617 Equation (40) relates the mean temperature evolution to surface mass and heat fluxes. Focusing
 1618 on the heat fluxes, and using (30) for the global mean heat content, renders

$$\frac{\partial \bar{\eta}}{\partial t} \approx \left(\frac{\alpha_{\text{bulk}}}{C_p \langle \rho \rangle} \right) \overline{Q^{\text{heat}}}. \quad (44)$$

1619 This expression, though approximate, provides a useful guide for how global mean sea level
 1620 evolves as a function of boundary fluxes. We identify the bulk thermal expansion coefficient,
 1621 α_{bulk} , as the measure for how efficient surface ocean heating is for changing global mean sea

1622 level. A warmer ocean generally has a larger α_{bulk} (Figure 1), in which case surface heating
 1623 increases sea level more efficiently than for a cooler ocean. This increased efficiency is also
 1624 reflected by a reduction in the global mean density $\langle \rho \rangle$ appearing in the denominator of equation
 1625 (44). To garner an order of magnitude estimate, assume the bulk thermal expansion coefficient to
 1626 be $\alpha_{\text{bulk}} \approx 1.54 \times 10^{-4} \text{ K}^{-1}$ (i.e., the global mean from Figure 1), and set $\langle \rho \rangle = 1035 \text{ kg m}^{-3}$ (an
 1627 estimate for the global mean density). In this case, a global mean heat flux of $\overline{Q^{\text{heat}}} = 1 \text{ W m}^{-2}$
 1628 yields a thermosteric sea level rise of roughly 1.2 mm yr^{-1} .

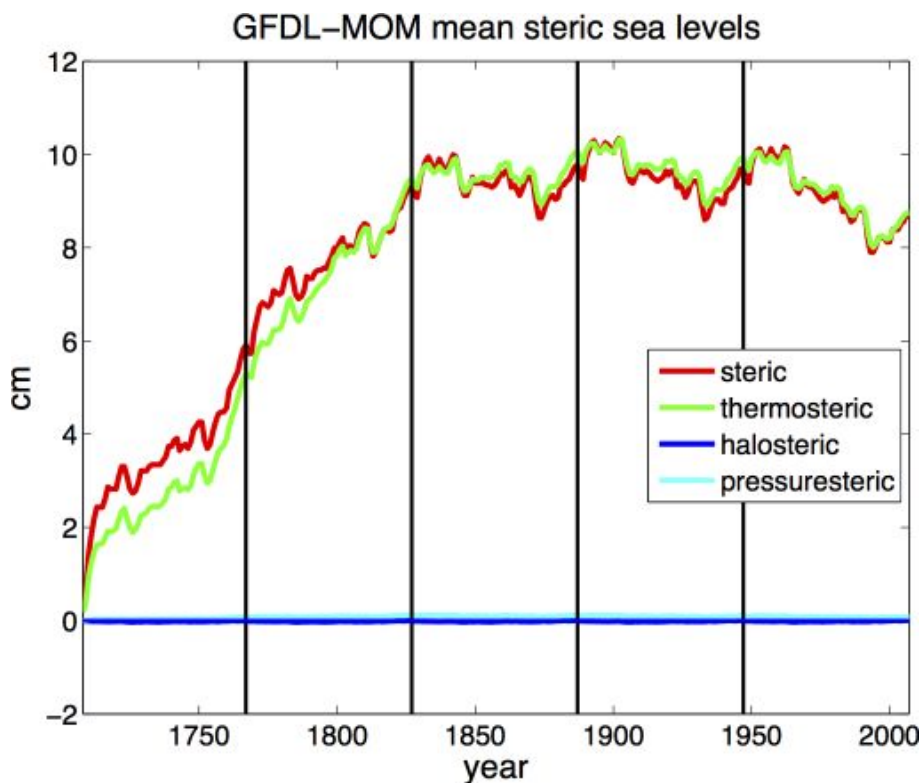


Figure 36: Time series for the global mean sea level from the GFDL-MOM simulation for the five cycles of the CORE-II simulations. We also exhibit the three contributions to this time series from the global mean potential temperature (with $\alpha_{\text{bulk}} = 1.9 \times 10^{-4} \text{ C}^{-1}$), global mean salinity (with $\beta_{\text{bulk}} = 7.5 \times 10^{-5} \text{ psu}^{-1}$), and global mean pressure (with $(\rho c^2)_{\text{bulk}} = 2.35 \times 10^9 \text{ kg m}^{-1} \text{ s}^{-2}$), according to equation (42). The bulk parameters were not formally optimized. As expected, the global mean sea level tracks quite closely to the global mean temperature, whereas salinity and pressure contributions are negligible. The vertical lines denote the start of a new 60 year cycle. We date the first cycle as starting at year 1708 to allow for a continuous time series over the five cycles completed at year 2007.

1629 The above considerations have proven to be quite useful for many purposes of global mean
 1630 sea level analyses, largely due to the good agreement seen in Figure 36 between the evolution
 1631 of global mean temperature and global mean sea level. However, there are disparities in Figure
 1632 36. It is thus useful to consider cases where equation (42) fails. One reason this equation fails in
 1633 principle is due to nonlinearities in the equation of state. To see how, consider a case in which

1634 global mean temperature, salinity, and pressure remain constant. According to equation (42),
 1635 global mean density should also remain constant. However, if ocean transport processes (i.e.,
 1636 advection and diffusion) redistribute temperature into regions of differing thermal expansion,
 1637 then global mean density will change. Global mean sea level will thus change through global
 1638 steric effects, yet without a global thermosteric effect. Apparently this counter-example to the
 1639 utility of equation (42) is not a leading order effect. However, it may be important locally.

1640 **Appendix B: Regional patterns of sea level**

1641 We discuss in this appendix rudiments of how dynamical processes are associated with re-
 1642 gional patterns of sea level. A full accounting of this topic requires a textbook on ocean dynam-
 1643 ics. Our aim is far more modest. Much of the material here borrows from the more thorough
 1644 discussions in Greatbatch (1994), Mellor and Ezer (1995), Huang and Jin (2002), and Lowe and
 1645 Gregory (2006). Furthermore, a summary of how wave phenomena (e.g., Rossby and Kelvin
 1646 waves), as well as currents and mesoscale eddies, reflect on sea level measured from altimeters
 1647 can be found in the review by Fu (2001).

1648 Throughout this appendix we make the dynamical assumption that the fluid maintains a
 1649 hydrostatic balance (as do all of the models in this study), so that pressure at a depth $z \leq \eta$ is
 1650 given by

$$p(z) = p_a + g \int_z^\eta \rho dz', \quad (45)$$

1651 where p_a is pressure applied at the ocean surface, presumably from atmosphere or sea ice load-
 1652 ing. This balance provides an expression for the pressure in terms of the weight per area of
 1653 seawater. The weight of fluid is a function of the amount of fluid, which is proportional to the
 1654 sea level. We may thus employ the hydrostatic balance to deduce relations between the sea level,
 1655 ocean density, and ocean mass.

1656 **B1. Temporal sea level fluctuations related to mass and density fluctuations**

1657 The hydrostatic balance (45) leads to the expression for bottom pressure

$$p_b = p_a + g \int_{-H}^\eta \rho dz. \quad (46)$$

1658 Taking the time derivative and rearranging leads to

$$\underbrace{\frac{\partial \eta}{\partial t}}_{\text{sea level tendency}} = \underbrace{\frac{1}{g \rho(\eta)} \left(\frac{\partial(p_b - p_a)}{\partial t} \right)}_{\text{mass tendency}} - \underbrace{\frac{1}{\rho(\eta)} \left(\int_{-H}^\eta \frac{\partial \rho}{\partial t} dz \right)}_{\text{local steric tendency}}. \quad (47)$$

1659 This decomposition of sea level tendency, first analyzed by Gill and Niiler (1973), relates tempo-
 1660 ral fluctuations in sea level to fluctuations in seawater mass per horizontal area within an ocean

1661 column (i.e., the difference between bottom pressure and applied surface pressure) and to fluctuations in density integrated over the column (i.e., the local steric effect). In simple terms, it
 1662 relates the changes in ocean volume to changes in ocean mass and changes in ocean density.
 1663 The mass tendency is associated with barotropic motions, and for a mass-conserving hydrostatic
 1664 fluid it takes the form
 1665

$$\frac{1}{g} \left(\frac{\partial(p_b - p_a)}{\partial t} \right) = -\nabla \cdot \mathbf{U}^\rho + Q_m, \quad (48)$$

1666 where $-\nabla \cdot \mathbf{U}^\rho$ is the convergence of the vertically integrated horizontal mass transport,

$$\mathbf{U}^\rho = \int_{-H}^{\eta} \rho \mathbf{u} \, dz, \quad (49)$$

1667 and Q_m is the mass flux crossing the ocean boundary. The density term in equation (47) arises
 1668 from changes in the density integrated over the depth of the water column.

1669 Landerer et al. (2007b), Landerer et al. (2007a), Yin et al. (2009), and Yin et al. (2010a)
 1670 made use of the balance (47) to help interpret simulated sea level patterns seen as the ocean
 1671 warms in climate model simulations. We conduct a similar analysis in Section 5. Namely, as
 1672 heating penetrates a water column, the amplitude of local steric sea level rise will be greater
 1673 for deeper columns because there is more water to absorb a greater quantity of heat. Hence,
 1674 there is an associated dynamic topography gradient next to continental shelf regions, with low
 1675 dynamic topography on the shelves and high dynamic topography in the deeper ocean. Dynamic
 1676 topography gradients lead, through dynamical adjustments, to modifications in ocean currents.
 1677 Without rotation, water will move onto the shelves, thus increasing mass and hence bottom
 1678 pressure on the shelves, and decreasing bottom pressure in the adjacent deeper ocean. Rotation
 1679 and hence geostrophic adjustment will modify this tendency to pile up mass on the shelves, as
 1680 will boundary friction associated with interactions with topography.

1681 Another way to present the above argument follows from noting that the relative change in
 1682 mass of a fluid column is given by the sum of the relative change in volume and the relative
 1683 change in density

$$\frac{\delta M}{M} = \frac{\delta V}{V} + \frac{\delta \rho}{\rho}. \quad (50)$$

1684 Now assume that the relative change in density is uniform throughout the seawater column. A
 1685 change in sea level, such as through uniform heating, will change volume, $\delta V > 0$. The relative
 1686 volume change, $\delta V/V$, will be larger in the shallow ocean where V is small. Correspondingly,
 1687 the relative change in mass for a seawater column is larger in the shallow ocean, such as on
 1688 continental shelves, than the deep ocean. Gregory et al. (2013) made use of this argument
 1689 when discussing the associated implications of the mass redistributions on the gravitational self-
 1690 attraction and loading.

1691 *B1.1. A note about certain linearized free surface methods*

1692 Many ocean models employ a linear free surface, such as in the papers from Killworth et al.
 1693 (1991) and Dukowicz and Smith (1994). In some implementations of these models, the free
 1694 surface is not felt by the budgets for tracer in the top model grid cell. Hence, the upper limit

1695 on the density integral in the hydrostatic balance (46) is set to $z = 0$ rather than $z = \eta$. A time
 1696 derivative of this approximate hydrostatic balance leads to a balance between column mass and
 1697 steric effects

$$\frac{\partial(p_b - p_a)}{\partial t} = g \int_{-H}^0 \frac{\partial \rho}{\partial t} dz \quad \text{some linear free surface models.} \quad (51)$$

1698 Note that the linear free surface from Roulet and Madec (2000) correctly includes the $\partial\eta/\partial t$
 1699 term as in equation (47), yet this term is omitted in models based on the Dukowicz and Smith
 1700 (1994) method. Models that maintain the balance (51) can diagnose terms appearing in the
 1701 physically correct balance (47) by including the extra contribution to the vertical integrals when
 1702 computing both the bottom pressure and the steric tendency.

1703 *B1.2. Local steric contributions to sea level changes*

1704 A question often asked in association with anthropogenic ocean warming is how trends in
 1705 water mass properties impact sea level (e.g., Lowe and Gregory, 2006; Landerer et al., 2007b;
 1706 Yin et al., 2010a). In general, sea level trends are impacted by changes in bottom pressure as well
 1707 as changes in *in situ* density, with equation (47) the fundamental relation for a hydrostatic fluid.
 1708 As a means to partially address the question, we may diagnose how temperature and salinity
 1709 changes alter the *in situ* density, and so focus just on the density tendency (the local steric term)
 1710 in equation (47).

1711 To introduce the algorithm for computing steric trends in sea level, we discretize the time
 1712 tendency of density according to

$$\Delta\tau \partial_t \rho \approx \rho(\tau + \Delta\tau) - \rho(\tau) \quad (52)$$

1713 where $\tau > 0$ is the time after the initial condition and $\Delta\tau$ is the time step. Expanding the right
 1714 hand side in a Taylor Series in terms of the density derivatives due to conservative/potential
 1715 temperature, salinity, and pressure, and truncating to the leading terms in the expansion, yields

$$\begin{aligned} \rho(\tau + \Delta\tau) - \rho(\tau) &\approx \frac{\partial \rho}{\partial \theta} [\theta(\tau + \Delta\tau) - \theta(\tau)] + \frac{\partial \rho}{\partial S} [S(\tau + \Delta\tau) - S(\tau)] + \frac{\partial \rho}{\partial p} [p(\tau + \Delta\tau) - p(\tau)] \\ &\approx \rho[\theta(\tau + \Delta\tau), S(\tau), p(\tau)] - \rho[\theta(\tau), S(\tau), p(\tau)] \\ &\quad + \rho[\theta(\tau), S(\tau + \Delta\tau), p(\tau)] - \rho[\theta(\tau), S(\tau), p(\tau)] \\ &\quad + \rho[\theta(\tau), S(\tau), p(\tau + \Delta\tau)] - \rho[\theta(\tau), S(\tau), p(\tau)]. \end{aligned} \quad (53)$$

1716 The steric sea level change over a single time step is then defined by the vertical integral

$$\eta^{\text{steric}}(\tau + \Delta\tau) = \eta(\tau) - \frac{1}{\rho_o} \sum dz \left(\rho[\theta(\tau + \Delta\tau), S(\tau + \Delta\tau), p(\tau + \Delta\tau)] - \rho[\theta(\tau), S(\tau), p(\tau)] \right). \quad (54)$$

1717 Iterating on this expression leads to the steric sea level at an arbitrary time step as a function of
 1718 the initial time, which defines a reference state

$$\eta^{\text{steric}}(\tau) = \eta(\tau^r) - \frac{1}{\rho_o} \sum dz [\rho(\theta, S, p) - \rho(\theta^r, S^r, p^r)], \quad (55)$$

1719 where the three dimensional conservative/potential temperature, salinity, and pressure (θ^r, S^r, p^r)
 1720 define the properties of the reference state. An analogous expression holds for the thermosteric
 1721 sea level, defined by

$$\eta^{\text{thermosteric}}(\tau) = \eta(\tau^r) - \frac{1}{\rho_o} \sum dz [\rho(\theta, S^r, p^r) - \rho(\theta^r, S^r, p^r)], \quad (56)$$

1722 the halosteric sea level, defined by

$$\eta^{\text{halosteric}}(\tau) = \eta(\tau^r) - \frac{1}{\rho_o} \sum dz [\rho(\theta^r, S, p^r) - \rho(\theta^r, S^r, p^r)], \quad (57)$$

1723 and the pressure-steric sea level, defined by

$$\eta^{\text{pressure-steric}}(\tau) = \eta(\tau^r) - \frac{1}{\rho_o} \sum dz [\rho(\theta^r, S^r, p) - \rho(\theta^r, S^r, p^r)]. \quad (58)$$

1724 Again, $\eta(\tau^r)$ is the sea level at the reference state, and ρ_o is a globally constant reference density.
 1725 We may alternatively choose the reference density to equal $\rho(\theta^r, S^r, p^r)$, in which case it is
 1726 brought inside the vertical integral. Although only leading to a trivial difference in the patterns,
 1727 we prefer to use ρ_o as it relates to the simplified version of equation (47) considered in Section
 1728 5 (see equation (13)). Either way, $\eta^{\text{thermosteric}}$ partitions the impact on sea level due to temperature
 1729 changes, $\eta^{\text{halosteric}}$ does so for salinity changes, $\eta^{\text{pressure-steric}}$ does so for pressure changes, and η^{steric}
 1730 includes all effects.

1731 Notably, the pressure-steric term $\eta^{\text{pressure-steric}}$ is largely sub-dominant, so that the steric changes
 1732 in equation (54) are largely described by the sum of $\eta^{\text{thermosteric}}$ and $\eta^{\text{halosteric}}$. Even so, in some cases
 1733 there is partial compensation (i.e., cancelation) between thermosteric and halosteric effects, such
 1734 as in the Atlantic where warm salty waters accumulate in the abyssal regions under global warm-
 1735 ing scenarios (see Section 5). Finally, we note that the truncation used to derive the expansion
 1736 (53) has been found to hold reasonably well for the CORE-II simulations analyzed in this pa-
 1737 per. That is, the steric sea level trends shown in Figure 19 are largely equal to the sum of the
 1738 thermosteric trends in Figure 22 and the halosteric trends in Figure 23.

1739 It may also be of interest to determine the depth range over which the dominant local steric
 1740 changes appear, such as in the study of Chang et al. (2010). Correspondingly, steric sea level
 1741 changes are best estimated from the observational record over just the upper 700 m of ocean,
 1742 and only for thermosteric effects. We thus may choose to consider the steric sea level as defined
 1743 above, but only for a portion of the ocean column. Figure 26 shows the patterns for 700 m
 1744 thermosteric changes and compares to various observation-based analyses. We may also wish
 1745 to determine the full depth dependence of the steric sea level changes, as averaged horizontally
 1746 over the globe, with Figures 5–7 showing the steric, thermosteric, and halosteric contributions
 1747 to global mean sea level as a function of depth and time.

1748 We based our diagnostic calculations of the steric sea level patterns shown in Section 5
 1749 on the annual mean conservative/potential temperature, salinity, and depth/pressure from the
 1750 simulations. The *in situ* density was computed using the same equation of state for all models
 1751 to evaluate the various density terms in equations (55)–(57). We performed this diagnostic
 1752 calculation using model temperature and salinity mapped to depth or pressure levels. We are
 1753 unaware of how to perform this decomposition using results on isopycnal layers.

1754 **B2. Sea level gradients related to mass and density gradients**

1755 We now apply a horizontal gradient to the bottom pressure equation (46), which leads to the
 1756 following expression for the horizontal gradient of sea level

$$\rho(\eta) \nabla \eta = g^{-1} \nabla (p_b - p_a) - \rho(-H) \nabla H - \int_{-H}^{\eta} \nabla \rho \, dz, \quad (59)$$

1757 where $\rho(-H) = \rho(x, y, z = -H(x, y), t)$ is seawater density at the ocean bottom. The horizontal
 1758 gradient of sea level is thus decomposed into a horizontal gradient of the mass in a fluid column,
 1759 the gradient of bottom topography, and the vertically integrated horizontal gradient of density.
 1760 To simplify this expression, approximate the surface and bottom density as a constant reference
 1761 density to write

$$\nabla \eta \approx \frac{1}{g \rho_o} \nabla (p_b - p_a) - \nabla H - \frac{1}{\rho_o} \int_{-H}^{\eta} \nabla \rho \, dz. \quad (60)$$

1762 Much of the horizontal variations in bottom pressure arise from changes in ocean bottom topog-
 1763 raphy. To remove this piece, consider bottom pressure variations relative to a static background
 1764 bottom pressure $\rho_o g H$. Writing

$$p_b = \rho_o g H + p'_b \quad (61)$$

1765 renders

$$\nabla \eta \approx \frac{1}{g \rho_o} \nabla (p'_b - p'_a) - \frac{1}{\rho_o} \int_{-H}^{\eta} \nabla \rho' \, dz, \quad (62)$$

1766 where $\rho = \rho' + \rho_o$, and $p_a = p'_a + \bar{p}_a$ introduce deviations of density and applied pressure from
 1767 a spatially uniform background. Equation (62) for the spatial structure of sea level takes the
 1768 same form mathematically as the temporal structure given by equation (47). Both expressions
 1769 partition sea level fluctuations (in time or space) into a contribution from fluctuations in the mass
 1770 within a fluid column, and fluctuations of density integrated over the column.

1771 To understand the spatial structure revealed by equation (62), consider the case where there
 1772 are no bottom pressure gradients; i.e., there is a level of no-motion beneath which the horizontal
 1773 gradients of pressure vanish (see Figure 37). Equation (62) then indicates that the sea level slope
 1774 is opposite to the slope of the vertically integrated density gradient. For example, consider a
 1775 warm anomaly in the upper ocean, in which case isopycnals depress downward. Sea level, in
 1776 turn, will expand upwards to render a local maximum (as in Figure 37).

1777 The overall magnitude of the sea level gradient associated with density gradients scales
 1778 according to

$$\nabla \eta \sim - \left(\frac{\delta \rho}{\rho_o} \frac{h}{L} \right), \quad (63)$$

1779 where $\delta \rho$ is the scale for the horizontal deviations in density. The depth h is the scale above the
 1780 level of no motion where density has a nontrivial horizontal gradient; it may also represent the
 1781 depth of the thermocline. Finally, L is the horizontal length scale over which horizontal density

1782 gradients are measured. For large-scale circulations, we are concerned with horizontal length
 1783 scales much larger than vertical, so that $L \gg h$. Additionally, horizontal deviations of density
 1784 are far smaller than the constant reference density, $\rho_o \gg \delta\rho$. Consequently, the sea level slope
 1785 is much smaller in magnitude than the pycnocline slope. In particular, Tomczak and Godfrey
 1786 (1994) (see Rule 1a on their page 33) notes that the sea level slope is roughly 100 to 300 times
 1787 shallower than the pycnocline slope.

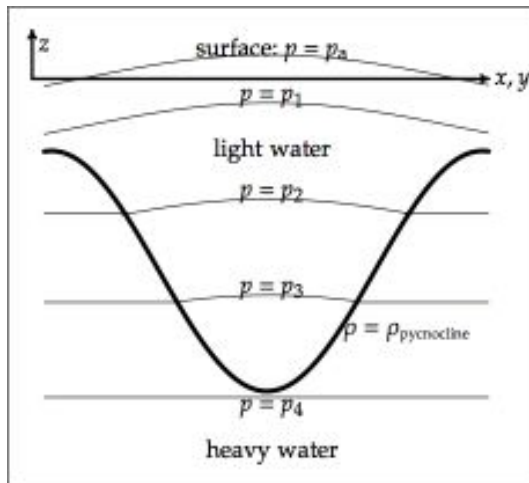


Figure 37: A vertical slice through a 1.5 layer ocean in hydrostatic balance, taken after Figure 3.3 from Tomczak and Godfrey (1994). Shown here is a plug of light water, as may occur in a warm core eddy, sitting on top of heavy water, where motion is assumed to vanish in the heavy water. The sea surface experiences an applied pressure $p = p_a$, assumed to be uniform for this idealized situation. Isolines of hydrostatic pressure are shown, with a slight upward bow to the isobars within the light water region, and flat isobars beneath, in the region of zero motion. Note how sea level is a maximum above the pycnocline minimum, which occurs due to baroclinic compensation. The slope of the pycnocline is about 100-300 times larger than the sea level (Rule 1a of Tomczak and Godfrey, 1994).

1788 B3. Balances between currents and sea level gradients

1789 The connection between sea level and currents is made by noting that the horizontal gradient
 1790 of hydrostatic pressure (equation (45)), which appears in the momentum equation, is given by

$$\nabla_z p = \nabla p_a + g \rho(\eta) \nabla \eta + g \int_z^\eta \nabla_z \rho \, dz. \quad (64)$$

1791 This expression exposes how sea level gradients impact the horizontal pressure gradient, which
 1792 in turn drives ocean currents.

1793 There are many cases where the sea level responds rapidly to atmospheric loading in estab-
 1794 lishing an inverse barometer structure (e.g., see Appendix C in Griffies and Greatbatch (2012)).
 1795 In this case, it is useful to absorb the applied pressure p_a into an effective sea level

$$\nabla \eta + \frac{\nabla p_a}{g \rho(\eta)} \approx \nabla \eta', \quad (65)$$

1796 where

$$\eta' = \eta + p_a/(\rho_o g), \quad (66)$$

1797 in which case the horizontal pressure gradient is given by

$$\nabla_z p \approx \nabla \eta' + g \int_z^\eta \nabla_z \rho \, dz. \quad (67)$$

1798 This approximate relation forms the basis for the analysis in this section.

1799 *B3.1. Surface ocean*

1800 Perhaps the simplest oceanographically relevant relation between sea level and ocean cur-
1801 rents occurs when the surface ocean flow is in geostrophic balance, in which case

$$g \nabla \eta' = -f \hat{\mathbf{z}} \wedge \mathbf{u}, \quad (68)$$

1802 where \mathbf{u} is the surface horizontal velocity. This equation forms the basis for how surface ocean
1803 currents are diagnosed from sea level observations (Wunsch and Stammer, 1998).

1804 If we include in the balance the turbulent momentum flux $\boldsymbol{\tau}^s$ through the ocean surface
1805 boundary, then the sea level gradient takes the form

$$g \nabla \eta' = -f \hat{\mathbf{z}} \wedge \mathbf{u} + \frac{\boldsymbol{\tau}^s}{\rho_o h_E}, \quad (69)$$

1806 where h_E is the Ekman depth over which the boundary stresses penetrate the upper ocean. As
1807 noted by Lowe and Gregory (2006), surface currents in balance with surface wind stresses tend
1808 to flow parallel to the sea level gradient, whereas geostrophically balanced surface currents are
1809 aligned with surfaces of constant sea level.

1810 *B3.2. Full ocean column*

1811 Vertically integrating the linearized form of the horizontal momentum budget in the absence
1812 of horizontal friction leads to the relation

$$(g \rho_o H) \nabla \eta' = \boldsymbol{\tau}^s + Q_m \mathbf{u}_m - \boldsymbol{\tau}^b - (\partial_t + f \hat{\mathbf{z}} \wedge) \mathbf{U}^o - \mathbf{B}. \quad (70)$$

1813 In this equation, $Q_m \mathbf{u}_m$ is the horizontal advective momentum flux associated with surface
1814 boundary fluxes of mass, with \mathbf{u}_m the horizontal momentum per mass of material crossing the
1815 ocean surface.⁴ Furthermore, $\boldsymbol{\tau}^b$ is the bottom momentum drag, and

$$\mathbf{B} = g \int_{-H}^\eta dz \int_z^\eta \nabla_z \rho \, dz' \quad (71)$$

⁴In ocean models, \mathbf{u}_m is generally taken as the surface ocean horizontal velocity.

1816 is a horizontal pressure gradient arising from horizontal density gradients throughout the ocean
 1817 column. In addition to the surface and bottom boundary terms, equation (70) reveals that the
 1818 sea level gradient is balanced by time tendencies and Coriolis force associated with the depth
 1819 integrated mass transport, and a horizontal pressure gradient arising from depth integrated baro-
 1820 clinic structure. Lowe and Gregory (2006) employed the steady state version of this balance
 1821 while ignoring boundary terms (see their equation (7)),

$$(g \rho_o H) \nabla \eta' \approx -f \hat{\mathbf{z}} \wedge \mathbf{U}^\rho - \mathbf{B} \quad (72)$$

1822 to help interpret the mechanisms for sea level changes in their coupled climate simulations.

1823 *B3.3. Barotropic geostrophic balance*

1824 As seen by equation (70), sea level gradients balance many terms, including surface fluxes,
 1825 internal pressure gradients, and vertically integrated transport. Dropping all terms except Cori-
 1826 olis leads to a geostrophic balance for the vertically integrated flow, whereby equation (70)
 1827 reduces to

$$(g \rho_o H) \nabla \eta' = f \hat{\mathbf{z}} \wedge \mathbf{U}^\rho, \quad (73)$$

1828 which is equivalent to

$$\mathbf{U}^\rho = - \left(\frac{g \rho_o H}{f} \right) \hat{\mathbf{z}} \wedge \nabla \eta'. \quad (74)$$

1829 That is, in this idealized flow situation, the sea level is, with a constant depth and Coriolis
 1830 parameter, the streamfunction for the vertically integrated flow.

1831 Following Wunsch and Stammer (1998), we consider the relation (73) for the purpose of
 1832 capturing a scaling to see how much vertically integrated transport is associated with a deviation
 1833 in the sea level. In particular, the meridional transport between two longitudes x_1 and x_2 is given
 1834 by

$$\int_{x_1}^{x_2} dx V^\rho = \frac{g \rho_o H}{f} [\eta(x_2) - \eta(x_1)], \quad (75)$$

1835 where we assumed the ocean bottom is flat. Note that the horizontal distance drops out from the
 1836 right hand side, so that the meridional geostrophic transport only depends on the difference in
 1837 sea level across the zonal section, and not on the length of the section. Following the example of
 1838 Wunsch and Stammer (1998), assume the ocean depth is $H = 4000$ m and set $f = 7.3 \times 10^{-5} \text{ s}^{-1}$,
 1839 as occurs at 30° latitude, which renders a transport of about $6 \times 10^9 \text{ kg s}^{-1}$, or six Sverdrups,⁵
 1840 for a sea level deviation of $\Delta\eta = 0.01$ m. This calculation, though subject to many assumptions,
 1841 provides a useful order of magnitude scaling to gauge the significance of a sea level deviation.

⁵A volume transport of $1 \text{ m}^3 \text{ s}^{-1}$ corresponds to roughly 10^3 kg s^{-1} mass transport of seawater, so that a volume Sverdrup of $10^6 \text{ m}^3 \text{ s}^{-1}$ corresponds to a mass Sverdrup of 10^9 kg s^{-1} .

1842 **B4. Evolution of ocean column thickness and dynamic topography**

1843 It is often assumed in physical oceanography that there is a pressure at which baroclinic
 1844 currents vanish (Pond and Pickard, 1983; Tomczak and Godfrey, 1994). This *level of no motion*
 1845 occurs if the barotropic pressure head associated with an undulation in the sea level is exactly
 1846 compensated by density structure within the ocean interior. Currents are static below the level
 1847 of no motion, and so this deeper region of the ocean is dynamically disconnected from changes
 1848 in sea level. Figure 37 illustrates this situation in the commonly considered 1.5 layer ocean.
 1849 The evolution of ocean column thickness between the surface and the level of no motion then
 1850 provides a useful proxy for the evolution of sea level.

1851 The above discussion motivates the following mathematical formulation, in which we con-
 1852 sider the thickness of fluid extending from the ocean free surface to a chosen pressure level in
 1853 the ocean interior, as given by

$$\mathcal{D}(\mathcal{P}) = \eta - z(\mathcal{P}). \quad (76)$$

1854 We may relate this expression to the vertical integral between two pressure surfaces of the spe-
 1855 cific volume ρ^{-1}

$$\mathcal{D}(\mathcal{P}) = \int_{z(\mathcal{P})}^{\eta} dz = g^{-1} \int_{p_a}^{\mathcal{P}} \frac{dp}{\rho}, \quad (77)$$

1856 where the second step used the hydrostatic balance $\partial_z p = -g\rho$. We refer to the thickness $\mathcal{D}(\mathcal{P})$
 1857 as the *dynamic topography* with respect to a reference pressure \mathcal{P} . Note that it is sometimes also
 1858 called the *steric sea level* with respect to pressure \mathcal{P} . Evolution of the dynamic topography \mathcal{D}
 1859 arises from changes in the applied pressure, and changes in the specific volume

$$g \frac{\partial \mathcal{D}(\mathcal{P})}{\partial t} = -\frac{1}{\rho(\eta)} \frac{\partial p_a}{\partial t} + \int_{p_a}^{\mathcal{P}} \frac{\partial \rho^{-1}}{\partial t} dp, \quad (78)$$

1860 where the time derivative acting on the specific volume is taken on surfaces of constant pressure.
 1861 If the depth $z(\mathcal{P})$ of the constant pressure surface is static, then the evolution of layer thickness
 1862 $\mathcal{D}(\mathcal{P})$ is identical to the sea level η . In general, there is no such static pressure level, thus making
 1863 the time tendencies differ, though certain situations may warrant this approximation.

1864 Analyses based on assuming a level of no motion were common in simulations with a
 1865 rigid lid ocean model, as in the studies of Delworth et al. (1993), Bryan (1996), Griffies and
 1866 Bryan (1997). Rigid lid models were the dominant algorithmic choice for ocean climate mod-
 1867 els through the early 2000s. As there is no tendency equation for the free surface in rigid lid
 1868 models, only indirect methods are available for obtaining information about the time variations
 1869 of the sea level. Gregory et al. (2001) provide an appendix in which they summarize commonly
 1870 used methods for analyzing sea level fluctuations within rigid lid ocean models. Amongst the
 1871 various methods, Gregory et al. (2001) note that the use of a level of no motion is inaccurate
 1872 in those regions where currents readily reach to the bottom. The Southern Ocean is one such
 1873 region, where the flow has a large barotropic component. Also, as noted by Danabasoglu and
 1874 McWilliams (2002), on intra-annual time scales, the tropical circulations on the depth/latitude
 1875 plane penetrate to the ocean bottom.

1876 Free surface ocean models compute dynamic sea level directly, in which case there is no
 1877 need to assume a level of no motion. Nor is it necessary to employ the approximate methods
 1878 detailed by Gregory et al. (2001) required to analyze simulated sea level variations in rigid lid
 1879 models. For this reason, and others such as the straightforward use of water fluxes rather than
 1880 virtual tracer fluxes (Griffies et al., 2001), rigid lid models are rarely used today for realistic
 1881 climate modelling, with preference given to models computing sea level or bottom pressure
 1882 prognostically. Nonetheless, given the records of observed hydrography, it remains useful to
 1883 consider dynamic topography as a proxy for dynamic sea level (e.g., Levitus, 1990).

1884 **Appendix C: Heat conservation properties of the CORE-II models**

1885 Given the importance of heat and salt conservation in ocean models used to study sea level,
 1886 we present in this Appendix a brief analysis of the heat conservation properties of the models
 1887 considered in this paper. We show that all but one of the models conserve heat.

1888 **C1. Quantitative statements about heat fluxes and global mean sea level**

1889 A global ocean mean boundary heat flux of $\overline{Q^{\text{heat}}} = 1 \text{ W m}^{-2}$ increases the global ocean
 1890 temperature by roughly⁶

$$\frac{\overline{Q^{\text{heat}}}}{\rho_o C_p^0 H} \approx 0.2^\circ\text{C century}^{-1}, \quad (79)$$

1891 $H \approx 4000 \text{ m}$ is the mean ocean depth. It is at this level, or slightly smaller, that estimates from
 1892 observations suggest the ocean has warmed during the second half of the 20th century, with an
 1893 increase in warming seen in the early years of the 21st century (Church et al., 2011). This same
 1894 heat flux gives rise to a global mean sea level rise of magnitude (see equation (44) in Appendix
 1895 A5)

$$\frac{\overline{Q^{\text{heat}}} \alpha_{\text{bulk}}}{\rho_o C_p} \approx 1 \text{ mm yr}^{-1} = 0.1 \text{ m century}^{-1} \quad (80)$$

1896 where we assumed the thermal expansion coefficient to be $\alpha_{\text{bulk}} \approx 1.7 \times 10^{-4} \text{ K}^{-1}$ (i.e., the
 1897 average over the upper 1000 m as shown in Figure 1).

1898 It is notable that there is a huge disparity between the magnitude of local values of ocean
 1899 surface heat fluxes, which can be $\pm 100 - 1000 \text{ W m}^{-2}$, and the relatively small residual global
 1900 mean ocean heat flux, which is on the order of 1 W m^{-2} . Local values of boundary heating drive
 1901 regional changes in thermosteric sea level, whereas the global mean heat flux drives the global
 1902 mean thermosteric sea level (Appendix A5). As described by Large and Yeager (2012) and

⁶The convention used in this paper for reporting heat fluxes (enthalpy per time per horizontal area) is to normalize by the ocean surface area. To compute the net enthalpy per time (in units of Watt) crossing the ocean surface requires multiplying by the ocean surface area. The alternative convention, often used in climate studies not specifically focused on the ocean, considers the enthalpy per time normalized by the total surface area of the earth. The two fluxes, measured as a Watt per square metre, differ by the area ratio which is roughly 0.7. Hence, a heat flux of 1 W m^{-2} computed with respect to the ocean surface area corresponds to 0.7 W m^{-2} with respect to the total earth surface area.

1903 Stephens et al. (2012), local uncertainties in the observed heat fluxes, which can be more than
1904 $\pm 10 \text{ W m}^{-2}$, make it difficult to detect trends in anthropogenic ocean warming through direct
1905 measures of boundary fluxes. Measures of global mean sea level provide an indirect means to
1906 determine the net ocean heating, with the ocean integrating the heat fluxes and so highlighting
1907 low frequency trends. This is the key reason that studies of global mean sea level are closely
1908 related to studies of ocean heat content.

1909 On interannual and longer time scales, the relatively large ocean heat capacity makes the
1910 ocean the dominant media (more than 90%) for heat storage in the climate system.⁷ Hence, one
1911 requirement for using ocean models to study global mean sea level is that the models properly
1912 represent the transfer of heat across the ocean boundaries, and impart that heat to the ocean
1913 fluid. That is, the models should conserve heat, so that the global mean ocean temperature
1914 changes only through the passage of fluxes across the ocean boundaries. Heat resulting from
1915 spurious sources or sinks is generally sequestered in the ocean and in turn impacts on global
1916 mean sea level. This is the key reason that heat conservation is essential for ocean models used
1917 to study global mean sea level. Salt conservation must also be respected for the same reasons.

1918 C2. A method to diagnose heat conservation

1919 Many models have online diagnostics to determine the degree to which the model conserves
1920 scalar fields, such as heat and salt. When available, we use these diagnostics to assess conser-
1921 vation. We also make use of another approach that integrates the budget for global mean ocean
1922 temperature, following the formulation in Appendix A4. Given the heat and mass fluxes cross-
1923 ing the liquid ocean boundaries, we time step equation (40) to provide an *offline* calculation of
1924 global mean ocean temperature. This offline global mean temperature is then compared to the
1925 *online* global mean temperature diagnosed directly from the associated model simulation. The
1926 two global mean ocean temperatures will not agree exactly, since we do not have access to the
1927 model restart files. So we must time step the offline equation (40) using annual mean boundary
1928 heat and mass fluxes, whereas the online mean temperature is accumulated using each model
1929 time step.

1930 To examine the conservation properties of the simulations, we compute the ratio of the global
1931 mean annual ocean temperature computed online to that computed offline. Unity signals perfect
1932 agreement, yet again, perfect agreement is not possible due to temporal sampling differences.
1933 Correspondingly, we expect a slight drift between the two calculations, since the offline calcu-
1934 lation accumulates the errors from temporal subsampling. We make the following observations
1935 based on this calculation.

- 1936 • ALL BUT ONE OF THE CORE-II SIMULATIONS CONSIDERED HERE CONSERVE OCEAN HEAT. As stated
1937 above, many of the conserving models possess online diagnostics that more rigorously

⁷As discussed on page 22 of Gill (1982), the atmosphere mass per horizontal area at the ocean surface is $\approx 10^4 \text{ kg m}^{-2}$. This is the mass per area of 10 m of liquid ocean. Furthermore, the specific heat capacity for the ocean, $C_p^0 \approx 3990 \text{ J }^\circ\text{C}^{-1} \text{ kg}^{-1}$, is about four times that of the atmosphere. Hence, 2.5 m of liquid ocean has the same heat capacity per horizontal area as the entire atmosphere.

1938 verify their conservation properties, thus supporting the conclusion that they are conser-
1939 vative.

1940 • **THE FSU-HYCOM CORE-II SIMULATION DOES NOT CONSERVE HEAT.** The online global mean
1941 ocean temperature from FSU-HYCOM is systematically warmer than the offline temper-
1942 ature computed from boundary heat fluxes. Both time series are reasonably linear (not
1943 shown), suggesting that the non-conservation is roughly constant in time. To test this
1944 hypothesis, we added 1 W m^{-2} to the surface heat flux for all time steps in the offline
1945 calculation. Doing so brings the temperature ratio in line to those from the conservative
1946 models (not shown). Megann et al. (2010) noted that when coupled to an atmosphere and
1947 land model, the HYCOM ocean temperature drifted in a way that suggested a spurious
1948 heat source on the order of 0.5 W m^{-2} . A non-conservative source of heat on the order of
1949 $0.5 - 1 \text{ W m}^{-2}$ thus appears to be associated with the HYCOM dynamical core used in the
1950 present study as well as Megann et al. (2010).

1951 The spurious heat source in FSU-HYCOM dominates the simulated global mean sea level
1952 throughout the CORE-II simulation. In particular, the net boundary heat flux into the
1953 FSU-HYCOM ocean during years 1993-2007 of the 5th CORE-II cycle is -0.75 W m^{-2}
1954 (Figures 10 and 11). For a conservative model, this negative heat flux would lead to a
1955 downward trend in global mean ocean temperature. However, global mean ocean temper-
1956 ature, as diagnosed within the prognostic model, is in fact rising during this same period
1957 (see Figure 4).

1958 **C3. Some lessons learned**

1959 Heat conservation, and in fact conservation of any scalar, should not be presumed of an
1960 ocean model until proven through analysis such as that considered here. Given the fundamental
1961 nature of scalar conservation, this basic analysis can be a powerful means of revealing limitations
1962 and/or bugs in a numerical ocean code. In fact, two earlier contributing models in this study
1963 were removed due to their egregious lack of heat conservation. Exposing problems with model
1964 conservation properties has resulted in the respective model developers re-examining their code
1965 with an aim to ensure that the numerical methods are fully conservative. The HYCOM code is a
1966 case in point, in which a version more recent than that used here has been written that conserves
1967 heat and salt (Rainer Bleck and Shan Sun, personal communication 2013). A suitable CORE-II
1968 simulation using this updated code was not available in time for inclusion in the present study.

REFERENCES

1969

- 1970 Antonov, J., Seidov, D., Boyer, T. P., Locarnini, R. A., Mishonov, A. V., Garcia, H. E., Baranova,
1971 O. K., Zweng, M. M., Johnson, D. R., 2010. World Ocean Atlas 2009, Volume 2: Salinity.
1972 NOAA Atlas NESDIS 69, NOAA/NESDIS, U.S. Dept. of Commerce, Washington, D.C.
- 1973 Bates, S., Fox-Kemper, B., Jayne, S. R., Large, W. G., Stevenson, S., Yeager, S. G., 2012. Mean
1974 biases, variability, and trends in air-sea fluxes and sea surface temperature in the CCSM4.
1975 *Journal of Climate* 25, 7781–7801.
- 1976 Becker, M., Meyssignac, B., Letetrel, C., Llovel, W., Cazenave, A., Delcroix, T., 2012. Sea level
1977 variations at tropical Pacific islands since 1950. *Global Planetary Change* 80-81, 85–98.
- 1978 Bouttes, N., Gregory, J. M., Lowe, J. A., 2013. The reversibility of sea level rise. *Journal of*
1979 *Climate* 26, 259–280.
- 1980 Boyer, T. P., Levitus, S., Antonov, J. I., Locarnini, R. A., Garcia, H. E., 2005. Linear
1981 trends in salinity for the World Ocean, 1955-1998. *Geophysical Research Letters* 32,L01604,
1982 doi:10.1029/2004GL021791.
- 1983 Brodeau, L., B.Barnier, Treguier, A., Penduff, T., Gulev, S., 2010. An ERA40-based atmospheric
1984 forcing for global ocean circulation models. *Ocean Modelling* 31, 88–104.
- 1985 Bromirski, P., Miller, A., Flick, R., Auad, G., 2011. Dynamical suppression of sea level rise
1986 along the Pacific coast of North America: Indications for imminent acceleration. *Journal of*
1987 *Geophysical Research* 116-C07005, doi:10.1029/2010JC006759.
- 1988 Bryan, F. O., 1997. The axial angular momentum balance of a global ocean general circulation
1989 model. *Dynamics of Atmospheres and Oceans* 25, 191–216.
- 1990 Bryan, K., 1996. The steric component of sea level rise associated with enhanced greenhouse
1991 warming: a model study. *Climate Dynamics* 12, 545–555.
- 1992 Capotondi, A., Alexander, M., Bond, N., Curchitser, E., Scott, J., 2012. Enhanced upper ocean
1993 stratification with climate change in the CMIP3 models. *Journal of Geophysical Research*
1994 117-C04031, doi:10.1029/2011JC007409.
- 1995 Chambers, D., Merrifield, M., Nerem, R., 2012. Is there a 60-year oscillation in global mean sea
1996 level? *Geophysical Research Letters* 39 (L18607), doi:10.1029/2012gl052885.
- 1997 Chang, Y.-S., Rosati, A., Vecchi, G., 2010. Basin patterns of global sea level changes for 2004-
1998 2007. *Journal of Marine Systems* 80, 115–124.
- 1999 Church, J., Roemmich, D., Domingues, C. M., Willis, J. K., White, N. J., Gilson, J. E., Stammer,
2000 D., Köhl, A., Chambers, D. P., Landerer, F. W., Marotzke, J., Gregory, J. M., Suzuki, T.,
2001 Cazenave, A., Traon, P.-Y. L., 2010. Ocean temperature and salinity contributions to global
2002 and regional sea-level change. In: Church, J. A., Woodworth, P. L., Aarup, T., Wilson, W. S.
2003 (Eds.), *Understanding Sea-Level Rise and Variability*. Blackwell Publishing, pp. 143–176.

- 2004 Church, J., White, N., Domingues, C., Monselesan, D., 2013. Sea-level change and ocean heat-
2005 content change. In: Siedler, G., Griffies, S. M., Gould, J., Church, J. (Eds.), *Ocean Circulation*
2006 *and Climate, 2nd Edition: A 21st Century Perspective*. Vol. 103 of *International Geophysics*
2007 *Series*. Academic Press.
- 2008 Church, J., White, N., Konikow, L., Domingues, C., Cogley, J., Rignot, E., Gregory, J.,
2009 van den Broeke, M., Monaghan, A., Velicogna, I., 2011. Revisiting the earth's sea-
2010 level and energy budgets from 1961 to 2008. *Geophysical Research Letters* 38, L18601,
2011 doi:10.1029/2011GL048794.
- 2012 Conkright, M., Antonov, J., Baranova, O., Boyer, T., Garcia, H., Gelfeld, F., Johnson, D., Lo-
2013 carnini, R., Murphy, P., O'Brien, T., Smolyar, I., Stephens, C., 2002. *World Ocean Database*
2014 2001, Volume 1: Introduction. NOAA Atlas NESDIS 42, U.S. Government Printing Office 13,
2015 NOAA, Washington, D.C., 167 pp.
- 2016 Dai, A., Qian, T., Trenberth, K., Milliman, J., 2009. Changes in continental freshwater discharge
2017 from 1948-2004. *Journal of Climate* 22, 2773–2791.
- 2018 Danabasoglu, G., 2004. A comparison of global ocean general circulation model solutions ob-
2019 tained with synchronous and accelerated integration methods. *Ocean Modelling* 7, 323–341.
- 2020 Danabasoglu, G., McWilliams, J., 2002. Eulerian and eddy-induced meridional overturning cir-
2021 culations in the tropics. *Journal of Physical Oceanography* 32, 2054–2071.
- 2022 Danabasoglu, G., Yeager, S. G., Bailey, D., Behrens, E., Bentsen, M., Bi, D., Biastoch, A.,
2023 Böning, C. W., Bozec, A., Canuto, V. M., Cassou, C., Chassignet, E., Coward, A. C., Danilov,
2024 S., Diansky, N., Drange, H., Farneti, R., Fernandez, E., Fogli, P. G., Forget, G., Fujii, Y.,
2025 Griffies, S. M., Gusev, A., Heimbach, P., Howard, A., Jung, T., Kelley, M., Large, W. G.,
2026 Leboissetier, A., Lu, J., Madec, G., Marsland, S. J., Masina, S., Navarra, A., Nurser, A. G.,
2027 Pirani, A., y Méliá, D. S., Samuels, B. L., Scheinert, M., Sidorenko, D., Treguier, A.-M.,
2028 Tsujino, H., Uotila, P., Valcke, S., Voldoire, A., Wang, Q., 2014. North Atlantic simulations
2029 in Coordinated Ocean-ice Reference Experiments phase II (CORE-II). Part I: Mean states.
2030 *Ocean Modelling* 73 (0), 76–107.
2031 URL <http://www.sciencedirect.com/science/article/pii/S1463500313001868>
- 2032 Delworth, T. L., Broccoli, A. J., Rosati, A., Stouffer, R. J., Balaji, V., Beesley, J. A., Cooke,
2033 W. F., Dixon, K. W., Dunne, J., Dunne, K. A., Durachta, J. W., Findell, K. L., Ginoux, P.,
2034 Gnanadesikan, A., Gordon, C., Griffies, S. M., Gudgel, R., Harrison, M. J., Held, I. M.,
2035 Hemler, R. S., Horowitz, L. W., Klein, S. A., Knutson, T. R., Kushner, P. J., Langenhorst,
2036 A. L., Lee, H.-C., Lin, S., Lu, L., Malyshev, S. L., Milly, P., Ramaswamy, V., Russell, J.,
2037 Schwarzkopf, M. D., Shevliakova, E., Sirutis, J., Spelman, M., Stern, W. F., Winton, M.,
2038 Wittenberg, A. T., Wyman, B., Zeng, F., Zhang, R., 2006. GFDL's CM2 global coupled
2039 climate models - Part 1: Formulation and simulation characteristics. *Journal of Climate* 19,
2040 643–674.
- 2041 Delworth, T. L., Manabe, S., Stouffer, R. J., 1993. Interdecadal variations of the thermohaline
2042 circulation in a coupled ocean-atmosphere model. *Journal of Climate* 6, 1993–2011.

- 2043 Domingues, C., Church, J., White, N., Gleckler, P., Wijffels, S., Barker, P., Dunn, J., 2008.
2044 Improved estimates of upper-ocean warming and multi-decadal sea-level rise. *Nature* 453,
2045 1090–1093.
- 2046 Doney, S. C., Yeager, S., Danabasoglu, G., Large, W., McWilliams, J., 2007. Mechanisms gov-
2047 erning interannual variability of upper-ocean temperature in a global ocean hindcast simula-
2048 tion. *Journal of Physical Oceanography* 37, 1918–1938.
- 2049 Ducet, N., Le Traon, P.-Y., Reverdin, G., 2000. Global high-resolution mapping of ocean cir-
2050 culation from TOPEX/Poseidon and ERS-1 and -2. *Journal of Geophysical Research* 105,
2051 19477–19498.
- 2052 Dukowicz, J. K., Smith, R. D., 1994. Implicit free-surface method for the Bryan-Cox-Semtner
2053 ocean model. *Journal of Geophysical Research* 99, 7991–8014.
- 2054 Durack, P., Wijffels, W., 2010. Fifty-year trends in global ocean salinities and their relationship
2055 to broad-scale warming. *Journal of Climate* 23, 4342–4362.
- 2056 Durack, P., Wijffels, W., Matear, R., 2012. Ocean salinities reveal strong global water cycle
2057 intensification during 1950 to 2000. *Science* 336, 455–458.
- 2058 Esselborn, S., Eden, C., 2001. Sea surface height changes in the North Atlantic Ocean related
2059 to the North Atlantic Oscillation. *Geophysical Research Letters* 28, 3473–3476.
- 2060 Ezer, T., Atkinson, L. P., Corlett, W., Blanco, J., 2013. Gulf Stream’s induced sea level rise
2061 and variability along the U.S. mid-Atlantic coast. *Journal of Geophysical Research* 118,
2062 doi:10.1002/jgrc.20091.
- 2063 Feng, M., McPhaden, M., Lee, T., 2010. Decadal variability of the Pacific subtropical cells
2064 and their influence on the Southeast Indian Ocean. *Geophysical Research Letters* 37, L09606,
2065 doi:10.1029/2010GL042796.
- 2066 Fox-Kemper, B., Lumpkin, R., Bryan, F., 2013. Lateral transport in the ocean interior. In:
2067 Siedler, G., Griffies, S. M., Gould, J., Church, J. (Eds.), *Ocean Circulation and Climate*, 2nd
2068 Edition: A 21st Century Perspective. Vol. 103 of International Geophysics Series. Academic
2069 Press, pp. 185–209.
- 2070 Fu, L.-L., 2001. Ocean circulation and variability from satellite altimetry. In: Seidler, G.,
2071 Church, J., Gould, J. (Eds.), *Ocean Circulation and Climate*. Vol. 77 of International Geo-
2072 physics Series. Academic Press, San Diego, pp. 141–172.
- 2073 Gates, W., 1993. AMIP: The Atmosphere Model Intercomparison Project. *Bulletin of the Amer-
2074 ican Meteorological Society* 73, 1962–1970.
- 2075 Gerdes, R., Hurlin, W., Griffies, S., 2006. Sensitivity of a global ocean model to increased run-off
2076 from Greenland. *Ocean Modelling* 12, 416–435.
- 2077 Gill, A., 1982. *Atmosphere-Ocean Dynamics*. Vol. 30 of International Geophysics Series. Aca-
2078 demic Press, London, 662 + xv pp.

- 2079 Gill, A. E., Niiler, P., 1973. The theory of the seasonal variability in the ocean. *Deep-Sea Re-*
2080 *search* 20 (9), 141–177.
- 2081 Gleckler, P., Santer, B., Domingues, C., Pierce, D., Barnett, T., Church, J., Taylor, K.,
2082 AchutaRao, K., Boyer, T., Ishii, M., Caldwell, P., 2012. Human-induced global ocean warm-
2083 ing on multidecadal timescales. *Nature Climate Change* 2, 524–529.
- 2084 Gower, J., 2010. Comment on “Response of the global ocean to Greenland and Antarctic ice
2085 melting”. *Journal of Geophysical Research* 115, doi:10.1029/2010JC006097.
- 2086 Greatbatch, R. J., 1994. A note on the representation of steric sea level in models that conserve
2087 volume rather than mass. *Journal of Geophysical Research* 99, 12767–12771.
- 2088 Gregory, J., Church, J., Boer, G., Dixon, K., Flato, G., Jackett, D., Lowe, J., O’Farrell, S.,
2089 Roeckner, E., Russell, G., Stouffer, R., Winton, M., 2001. Comparison of results from several
2090 AOGCMs for global and regional sea-level change 1900–2100. *Climate Dynamics* 18, 225–
2091 240.
- 2092 Gregory, J., White, N., Church, J., Bierkens, M., Box, J., van den Broeke, R., Cogley, J., Fet-
2093 tweis, X., Hanna, E., Huybrechts, P., Konikow, L., Leclercq, P., Marzeion, B., Orelemans,
2094 J., Tamisiea, M., Wada, Y., Wake, L., van den Wal, R., 2013. Twentieth-century global-mean
2095 sea-level rise: is the whole greater than the sum of the parts? *Journal of Climate* (26), 4476–
2096 4499.
- 2097 Griffies, S. M., Adcroft, A. J., Aiki, H., Balaji, V., Bentson, M., Bryan, F., Danabasoglu, G.,
2098 Denvil, S., Drange, H., England, M., Gregory, J., Hallberg, R., Legg, S., Martin, T., Mc-
2099 Dougall, T. J., Pirani, A., Schmidt, G., Stevens, D., Taylor, K., Tsujino, H., 2009a. Sampling
2100 physical ocean fields in WCRP CMIP5 simulations.
- 2101 Griffies, S. M., Biastoch, A., Böning, C. W., Bryan, F., Danabasoglu, G., Chassignet, E., Eng-
2102 land, M. H., Gerdes, R., Haak, H., Hallberg, R. W., Hazeleger, W., Jungclaus, J., Large, W. G.,
2103 Madec, G., Pirani, A., Samuels, B. L., Scheinert, M., Gupta, A. S., Severijns, C. A., Simmons,
2104 H. L., Treguier, A. M., Winton, M., Yeager, S., Yin, J., 2009b. Coordinated Ocean-ice Refer-
2105 ence Experiments (COREs). *Ocean Modelling* 26, 1–46.
- 2106 Griffies, S. M., Bryan, K., 1997. A predictability study of simulated North Atlantic multidecadal
2107 variability. *Climate Dynamics* 13, 459–487.
- 2108 Griffies, S. M., Greatbatch, R. J., 2012. Physical processes that impact the evolution of global
2109 mean sea level in ocean climate models. *Ocean Modelling* 51, 37–72.
- 2110 Griffies, S. M., Pacanowski, R., Schmidt, M., Balaji, V., 2001. Tracer conservation with an
2111 explicit free surface method for z -coordinate ocean models. *Monthly Weather Review* 129,
2112 1081–1098.
- 2113 Griffies, S. M., Pacanowski, R. C., Hallberg, R. W., 2000. Spurious diapycnal mixing associated
2114 with advection in a z -coordinate ocean model. *Monthly Weather Review* 128, 538–564.

- 2115 Häkkinen, S., 2000. Decadal air-sea interaction in the North Atlantic based on observations and
2116 modeling results. *Journal of Climate* 13, 1195–1219.
- 2117 Häkkinen, S., Rhines, P., 2004. Decline of subpolar North Atlantic circulation during the 1990s.
2118 *Science* 304, 555–559.
- 2119 Hallberg, R., Adcroft, A., Dunne, J., Krasting, J., Stouffer, R., 2013. Sensitivity of twenty-first-
2120 century global-mean steric sea level rise to ocean model formulation. *Journal of Climate* 26,
2121 2947–2956.
- 2122 Hanna, E., Navarro, F., Pattyn, F., Domingues, C., Fettweis, X., Ivins, E., Nicholls, R., Ritz, C.,
2123 Smith, B., Tulaczy, S., Whitehouse, P., Zwally, H., 2013. Ice-sheet mass balance and climate
2124 change. *Nature* 498, 51–59.
- 2125 Hosoda, S., Sugo, T., Shikama, N., Mizuno, K., 2009. Global surface layer salinity change de-
2126 tected by Argo and its implication for hydrological cycle intensification. *Journal of Oceanog-
2127 raphy* 65, 579–586.
- 2128 Hsieh, W., Bryan, K., 1996. Redistribution of sea level rise associated with enhanced greenhouse
2129 warming: a simple model study. *Climate Dynamics* 12, 535–544.
- 2130 Huang, R. X., 1993. Real freshwater flux as a natural boundary condition for the salinity bal-
2131 ance and thermohaline circulation forced by evaporation and precipitation. *Journal of Physical
2132 Oceanography* 23, 2428–2446.
- 2133 Huang, R. X., Jin, X., 2002. Sea surface elevation and bottom pressure anomalies due to ther-
2134 mohaline forcing: Part i: Isolated perturbations. *Journal of Physical Oceanography* 32, 2131–
2135 2150.
- 2136 Hurrell, J., Hack, J., Shea, D., Caron, J., Rosinski, J., 2008. A new sea surface temperature
2137 and sea ice boundary data set for the Community Atmosphere Model. *Journal of Climate* 21,
2138 5145–5153.
- 2139 IOC, SCOR, IAPSO, 2010. The international thermodynamic equation of seawater-2010: calcu-
2140 lation and use of thermodynamic properties. Intergovernmental Oceanographic Commission,
2141 Manuals and Guides No. 56, UNESCO, available from <http://www.TEOS-10.org>, 196pp.
- 2142 Ishii, M., Kimoto, M., 2009. Reevaluation of historical ocean heat content variations with time-
2143 varying XBT and MBT depth bias corrections. *Journal of Oceanography* 65, 287–299.
- 2144 Kalnay, E. M., Kanamitsu, M., Kistler, R., Collins, W., Deaven, D., Gandin, L., Iredell, M.,
2145 Saha, S., White, G., Woollen, J., Zhu, Y., Leetmaa, A., Reynolds, R., Chelliah, M., Ebisuzaki,
2146 W., W.Higgins, Janowiak, J., Mo, K. C., Ropelewski, C., Wang, J., Jenne, R., Joseph, D.,
2147 1996. The NMC/NCAR 40-year reanalysis project. *Bulletin of the American Meteorological
2148 Society* 77, 437–471.

- 2149 Kennedy, J., Rayner, N., Smith, R., Parker, D., Saunby, M., 2011. Reassessing biases and
2150 other uncertainties in sea surface temperature observations measured in situ since 1850: 1.
2151 Measurement and sampling uncertainties. *Geophysical Research Letters* 116, D14103, DOI:
2152 10.1029/2010JD015218.
- 2153 Killworth, P. D., Stainforth, D., Webb, D. J., Paterson, S. M., 1991. The development of a free-
2154 surface Bryan-Cox-Semtner ocean model. *Journal of Physical Oceanography* 21, 1333–1348.
- 2155 Köhl, A., Stammer, D., 2008. Decadal sea level changes in the 50-year GECCO ocean synthesis.
2156 *Journal of Climate* 21, 1876–1890.
- 2157 Kopp, R. E., 2013. Does the mid-Atlantic United States sea-level acceleration hot spot reflect
2158 ocean dynamic variability? *Geophysical Research Letters*, doi:10.1002/grl.50781.
- 2159 Kopp, R. E., Mitrovica, J. X., Griffies, S. M., Yin, J., Hay, C. C., Stouffer, R. J., 2010. The
2160 impact of Greenland melt on regional sea level: a preliminary comparison of dynamic and
2161 static equilibrium effects. *Climatic Change Letters* 103, 619–625.
- 2162 Kuhlbrodt, T., Gregory, J. M., 2012. Ocean heat uptake and its consequences for the mag-
2163 nitude of sea level and climate change. *Geophysical Research Letters* 38, L18608, doi:
2164 10.1029/2012GL052952.
- 2165 Lambeck, K., Esat, T., Potter, E., 2002. Links between climate and sea levels for the past three
2166 million years. *Nature* 419, 199–206.
- 2167 Landerer, F., Jungclaus, J., Marotzke, J., 2007a. Ocean bottom pressure changes lead to a de-
2168 creasing length-of-day in a warming climate. *Geophysical Research Letters* 34-L06307, doi:
2169 10.1029/2006GL029106.
- 2170 Landerer, F., Jungclaus, J., Marotzke, J., 2007b. Regional dynamic and steric sea level change
2171 in response to the IPCC-A1B Scenario. *Journal of Physical Oceanography* 37, 296–312.
- 2172 Large, W. G., Yeager, S., 2009. The global climatology of an interannually varying air-sea flux
2173 data set. *Climate Dynamics* 33, 341–364.
- 2174 Large, W. G., Yeager, S., 2012. On the observed trends and changes in global sea surface tem-
2175 perature and air-sea heat fluxes (1984-2006). *Journal of Climate* 25, 6123–6135.
- 2176 Laxon, S., Giles, K. A., Ridout, A. L., Wingham, D. J., Willatt, R., Cullen, R., Kwok, R.,
2177 Schweiger, A., Zhang, J., Haas, C., Hendricks, S., Krisheld, R., Kurtz, N., Farrell, S., David-
2178 son, M., 2013. CryoSat-2 estimates of Arctic sea ice thickness and volume. *Geophysical Re-
2179 search Letters* 40, doi:10.1002/grl.50193.
- 2180 Le Traon, P.-Y., Nadal, F., Ducet, N., 1998. An improved mapping method of multi-satellite
2181 altimeter data. *Journal of Atmospheric and Oceanic Technology* 15, 522–534.
- 2182 Leuliette, E., Willis, J., 2011. Balancing the sea level budget. *Oceanography* 24, 122–129.

- 2183 Levitus, S., 1990. Multipentadal variability of steric sea level and geopotential thickness of the
2184 north atlantic ocean, 19701974 versus 19551959. *Journal of Geophysical Research* 95, 5233–
2185 5238.
- 2186 Levitus, S., Antonov, J., Boyer, T., 2005. Warming of the world ocean, 19552003. *Geophysical*
2187 *Research Letters* 32 (2), 10.1029/2004GL021592.
2188 URL <http://dx.doi.org/10.1029/2004GL021592>
- 2189 Levitus, S., Antonov, J., Boyer, T., Baranova, O., Garcia, H., Locarnini, R., Mishonov, A.,
2190 Reagan, J., Seidov, D., Yarosh, E., Zweng, M. M., 2012. World ocean heat content and ther-
2191 mosteric sea level change (0-2000 m), 1955-2010. *Geophysical Research Letters* 39, L10603,
2192 doi:10.1029/2012GL051106.
- 2193 Locarnini, R., Mishonov, A. V., Antonov, J. I., Boyer, T. P., Garcia, H. E., Baranova, O. K.,
2194 Zweng, M. M., Johnson, D. R., 2010. *World Ocean Atlas 2009, Volume 1: Temperature*.
2195 NOAA Atlas NESDIS 68, NOAA/NESDIS, U.S. Dept. of Commerce, Washington, D.C.
- 2196 Lohmann, K., Drange, H., Bentsen, M., 2009. A possible mechanism for the strong weakening
2197 of the north atlantic subpolar gyre in the mid-1990s. *Geophysical Research Letters* 36 (15),
2198 10.1029/2009GL039166.
2199 URL <http://dx.doi.org/10.1029/2009GL039166>
- 2200 Lombard, A., Garric, G., Penduff, T., 2009. Regional patterns of observed sea level change:
2201 insights from a 1/4° global ocean/sea-ice hindcast. *Ocean Dynamics* 59, 433–449.
- 2202 Lorbacher, K., Dengg, J., Böning, C., Biastoch, A., 2010. Regional patterns of sea level change
2203 related to interannual variability and multidecadal trends in the atlantic meridional overturning
2204 circulation. *Journal of Physical Oceanography* 23, 4243–4254.
- 2205 Lorbacher, K., Marsland, S. J., Church, J. A., Griffies, S. M., Stammer, D., 2012. Rapid
2206 barotropic sea-level rise from ice-sheet melting scenarios. *Journal of Geophysical Research*
2207 117, C06003.
- 2208 Losch, M., Adcroft, A., Campin, J.-M., 2004. How sensitive are coarse general circulation mod-
2209 els to fundamental approximations in the equations of motion? *Journal of Physical Oceanog-*
2210 *raphy* 34, 306–319.
- 2211 Lowe, J. A., Gregory, J. M., 2006. Understanding projections of sea level rise in a Hadley Centre
2212 coupled climate model. *Journal of Geophysical Research*, C11014.
- 2213 MacKinnon, J., Louis St. Laurent, Garabato, A. N., 2013. Diapycnal mixing processes in the
2214 ocean interior. In: Siedler, G., Griffies, S. M., Gould, J., Church, J. (Eds.), *Ocean Circulation*
2215 *and Climate, 2nd Edition: A 21st century perspective*. Vol. 103 of *International Geophysics*
2216 *Series*. Academic Press.
- 2217 McCarthy, G., Frajka-Williams, E., Johns, W., Baringer, M., Meinen, C., Bryden, H., Rayner,
2218 D., Duche, A., Roberts, C., Cunningham, S. A., 2012. Observed interannual variability

- 2219 of the Atlantic meridional overturning circulation at 26.5°N. *Geophysical Research Letters*,
2220 doi:10.1029/2012GL052933.
- 2221 McDougall, T. J., 2003. Potential enthalpy: a conservative oceanic variable for evaluating heat
2222 content and heat fluxes. *Journal of Physical Oceanography* 33, 945–963.
- 2223 McGregor, S., Sen Gupta, A., England, M., 2012. Constraining wind stress products with sea sur-
2224 face height observations and implications for Pacific ocean sea level trend attribution. *Journal*
2225 *of Climate* 25, 8164–8176.
- 2226 Meehl, G., Covey, C., Delworth, T., Latif, M., McAvaney, B., Mitchell, J., Stouffer, R., Taylor,
2227 K., 2007. The WCRP CMIP3 multimodel dataset: A new era in climate change research.
2228 *Bulletin of the American Meteorological Society* 88, 1383–1394.
- 2229 Meehl, G., Hi, A., Santer, B., 2009. The mid-1970s climate shift in the Pacific and the relative
2230 roles of forced versus inherent decadal variability. *Journal of Climate* 22, 780–792.
- 2231 Megann, A., New, A., Blaker, A., Sinha, B., 2010. The sensitivity of a coupled climate model to
2232 its ocean component. *Journal of Climate* 23, 5126–5150.
- 2233 Mellor, G. L., Ezer, T., 1995. Sea level variations induced by heating and cooling: an evaluation
2234 of the Boussinesq approximation in ocean models. *Journal of Geophysical Research* 100,
2235 20565–20577.
- 2236 Merrifield, M., 2011. A shift in western tropical Pacific sea level trends during the 1990s. *Journal*
2237 *of Climate* 24, 4126–4138.
- 2238 Merrifield, M., Maltrud, M., 2011. Regional sea level trends due to a Pacific trade wind intensi-
2239 fication. *Geophysical Research Letters* 38-L21605, doi:10.1029/2011GL049576.
- 2240 Merrifield, M., Thompson, P. R., Lander, M., 2012. Multidecadal sea level anomalies and trends
2241 in the western tropical Pacific. *Geophysical Research Letters* 39, L13602.
- 2242 Meyssignac, B., Salas y Melia, D., Becker, M., Llovel, W., Cazenave, A., 2012. Tropic Pacific
2243 spatial trend patterns in observed sea level: internal variability and/or anthropogenic signa-
2244 ture? *Climate of the Past* 8, 787–802.
- 2245 Mitrovica, J. X., Tamisiea, M. E., Davis, J. L., Milne, G. A., 2001. Recent mass balance of polar
2246 ice sheets inferred from patterns of global sea-level change. *Nature* 409, 1026–1029.
- 2247 Palter, J. B., Griffies, S. M., Galbraith, E. D., Gnanadesikan, A., Samuels, B. L., Klocker, A.,
2248 2014. The deep ocean buoyancy budget and its temporal variability. *Journal of Climate* 27,
2249 551–573.
- 2250 Pardaens, A., Gregory, J., Lowe, J., 2011a. A model study of factors influencing pro-
2251 jected changes in regional sea level over the twenty-first century. *Climate Dynamics*,
2252 10.1029/2011GL047678.

- 2253 Pardaens, A. K., Lowe, J. A., Brown, S., Nicholls, R. J., de Gusmão, D., 2011b. Sea-level rise
2254 and impacts projections under a future scenario with large greenhouse gas emission reduc-
2255 tions. *Geophysical Research Letters* 38 (12), 10.1029/2011GL047678.
2256 URL <http://dx.doi.org/10.1029/2011GL047678>
- 2257 Peterson, B., Holmes, R., McClelland, J., Vörösmarty, C., Lammers, R., Shiklomanov, A., Shik-
2258 lomanov, I., Rahmstorf, S., 2002. Increasing river discharge to the Arctic Ocean. *Science* 298,
2259 2171–21738044.
- 2260 Pond, S., Pickard, G. L., 1983. *Introductory Dynamical Oceanography*, 2nd Edition. Pergamon
2261 Press, Oxford.
- 2262 Purkey, S., Johnson, G., 2010. Warming of global abyssal and deep Southern Ocean waters
2263 between the 1990s and 2000s: contributions to global heat and sea level rise budgets. *Journal*
2264 *of Climate* 23, 6336–6351.
- 2265 Rabe, B., Karcher, M., Schauer, U., Toole, J. M., Krishfield, R. A., Pisarev, S., Kauker, F.,
2266 Gerdes, R., Kikuchi, T., 2011. An assessment of Arctic Ocean freshwater content changes
2267 from the 1990s to the 2006-2008 period. *Deep Sea Research Part I: Oceanographic Research*
2268 *Papers* 58 (2), 173 – 185.
2269 URL <http://www.sciencedirect.com/science/article/pii/S0967063710002414>
- 2270 Reynolds, R. W., Rayner, N., Smith, T. M., Stokes, D., Wang, W., 2002. An improved *in situ*
2271 and satellite SST analysis for climate. *Journal of Climate* 15, 1609–1625.
- 2272 Robson, J., Sutton, R., Lohmann, K., Smith, D., Palmer, M. D., 2012. Causes of the rapid
2273 warming of the North Atlantic Ocean in the mid-1990s. *Journal of Climate* 25, 4116–4134.
- 2274 Roemmich, D., Gilson, J., 2011. The global ocean imprint of enso. *Geophysical Research Letters*
2275 38 (13), 10.1029/2011GL047992.
2276 URL <http://dx.doi.org/10.1029/2011GL047992>
- 2277 Roemmich, D., Gilson, J., Davis, R., Sutton, P., Wijffels, W., Riser, S., 2007. Decadal spinup of
2278 the South Pacific subtropical gyre. *Journal of Physical Oceanography* 37, 162–173.
- 2279 Rohling, E., Grant, K., Bolshaw, M., Roberts, A. P., Siddall, M., Hemleben, C., Kucera, M.,
2280 2009. Antarctic temperature and global sea level closely coupled over the past five glacial
2281 cycles. *Nature Geosciences* 2, 500–504.
- 2282 Roulet, G., Madec, G., 2000. Salt conservation, free surface, and varying volume. a new formu-
2283 lation for ogcms. *JGR* 105, 23927–23947.
- 2284 Sallée, J.-B., Speer, K., Morrow, R., 2008. Ocean fronts and their variability to climate modes.
2285 *Journal of Climate* 21, 3020–3039.
- 2286 Sallenger, A. H., Doran, K. S., Howd, P. A., 2012. Hotspot of accelerated sea-level rise on the
2287 Atlantic coast of North America. *Nature Geosciences*.

- 2288 Schiller, A., Lee, T., Masuda, S., 2013. Methods and applications of ocean synthesis in climate
2289 research. In: Siedler, G., Griffies, S. M., Gould, J., Church, J. (Eds.), *Ocean Circulation*
2290 *and Climate, 2nd Edition: A 21st Century Perspective*. Vol. 103 of *International Geophysics*
2291 *Series*. Academic Press, pp. 581–608.
- 2292 Schwarzkopf, F. U., Böning, C. W., 2011. Contribution of Pacific wind stress to multi-decadal
2293 variations in upper-ocean heat content and sea level in the tropical south Indian Ocean. *Geo-*
2294 *physical Research Letters* 38, doi: 10.1029/2011GL047651.
- 2295 Shepherd, A., Wingham, D., Wallis, D., Giles, K., Laxon, S., Sundal, A. V., 2010. Recent loss of
2296 floating ice and the consequent sea level contribution. *Geophysical Research Letters* 37 (13),
2297 10.1029/2010GL042496.
2298 URL <http://dx.doi.org/10.1029/2010GL042496>
- 2299 Slangen, A., Katsman, C., van de Wal, R., Vermeersen, L., Riva, R., 2012. Towards regional
2300 projections of twenty-first century sea-level change based on IPCC SRES scenarios. *Climate*
2301 *Dynamics*, 10.1007/s00382-011-1057-6.
- 2302 Stammer, D., 2008. Response of the global ocean to Greenland and Antarctic ice melting. *Jour-*
2303 *nal of Geophysical Research* 113, doi:10.1029/2006JC004079.
- 2304 Steele, M., Morfley, R., Ermold, W., 2001. PHC: A global ocean hydrography with a high-
2305 quality Arctic Ocean. *Journal of Climate* 14, 2079–2087.
- 2306 Stephens, G., Ward, M., Jr., P. S., L'Ecuyer, T., Vato, S., Hendersen, D., 2012. The global
2307 character of the flux of downward longwave radiation. *Journal of Climate* 25, 2329–2340.
- 2308 Stouffer, R. J., 2004. Time scales of climate response. *Journal of Climate* 17, 209–217.
- 2309 Taylor, K., Stouffer, R., Meehl, G., 2012. An overview of CMIP5 and the experiment design.
2310 *Bulletin of the American Meteorological Society* 93, 485–498.
- 2311 Timmermann, A., McGregor, S., Jin, F.-F., 2010. Wind effects on past and future regional sea
2312 level trends in the Southern Indo-Pacific. *Journal of Climate* 23, 4429–4437.
- 2313 Tomczak, M., Godfrey, J. S., 1994. *Regional Oceanography: An Introduction*. Pergamon Press,
2314 Oxford, England, 422 + vii pp.
- 2315 Trenberth, K. E., Hurrell, J., 1994. Decadal atmosphere-ocean variations in the Pacific. *Climate*
2316 *Dynamics* 9, 303–319.
- 2317 Weijer, W., Maltrud, M., Hecht, M., Dijkstra, H., Kliphuis, M., 2012. Response of the atlantic
2318 ocean circulation to greenland ice sheet melting in a strongly-eddying ocean model. *Geophys-*
2319 *ical Research Letters* 39-L09606, doi:10.1029/2012GL051611.
- 2320 Wijffels, S. E., Willis, J., Domingues, C. M., Barker, P., White, N. J., Gronell, A., Ridgway, K.,
2321 Church, J. A., 2008. Changing expendable bathythermograph fall rates and their impact on
2322 estimates of thermosteric sea level rise. *Journal of Climate* 21, 5657–5672.

- 2323 Wunsch, C., Heimbach, P., 2013. Dynamically and kinematically consistent global ocean cir-
2324 culation and ice state estimates. In: Siedler, G., Griffies, S. M., Gould, J., Church, J. (Eds.),
2325 Ocean Circulation and Climate, 2nd Edition: A 21st Century Perspective. Vol. 103 of Inter-
2326 national Geophysics Series. Academic Press, pp. 553–579.
- 2327 Wunsch, C., Ponte, R., Heimbach, P., 2007. Decadal trends in sea level patterns: 1992–2004.
2328 Journal of Climate 20, 5889–5911.
- 2329 Wunsch, C., Stammer, D., 1998. Satellite altimetry, the marine geoid, and the oceanic general
2330 circulation. Annual Reviews of Earth Planetary Science 26, 219–253.
- 2331 Yeager, S. G., Karspeck, A., Danabasoglu, G., Tribbia, J., Teng, H., 2012. A decadal prediction
2332 case study: late twentieth-century North Atlantic ocean heat content. Journal of Climate 25,
2333 5173–5189.
- 2334 Yin, J., 2005. A consistent poleward shift of the storm tracks in simulations of 21st century
2335 climate. Geophysical Research Letters 32-L18701, doi:10.1029/2005GL023684.
- 2336 Yin, J., 2012. Century to multi-century sea level rise projections from cmip5 models. Geophys-
2337 ical Research Letters 39 (17), 10.1029/2012GL052947.
2338 URL <http://dx.doi.org/10.1029/2012GL052947>
- 2339 Yin, J., Goddard, P., 2013. Oceanic control of sea level rise patterns along the east coast of the
2340 united states. Geophysical Research Letters in revision.
- 2341 Yin, J., Griffies, S. M., Stouffer, R., 2010a. Spatial variability of sea-level rise in 21st century
2342 projections. Journal of Climate 23, 4585–4607.
- 2343 Yin, J., Overpeck, J., Griffies, S., Hu, A., Russell, J., Stouffer, R., 2011. Different magnitudes of
2344 projected subsurface ocean warming around Greenland and Antarctica. Nature Geosciences.
- 2345 Yin, J., Schlesinger, M., Stouffer, R., 2009. Model projections of rapid sea-level rise on the
2346 northeast coast of the United States. Nature Geosciences 2, 262–266.
- 2347 Yin, J., Stouffer, R., Spelman, M. J., Griffies, S. M., 2010b. Evaluating the uncertainty induced
2348 by the virtual salt flux assumption in climate simulations and future projections. Journal of
2349 Climate 23, 80–96.
- 2350 Zhang, R., 2008. Coherent surface-subsurface fingerprint of the Atlantic meridional overturning
2351 circulation. Geophysical Research Letters 35, doi: 10.1029/2008gl035463.
- 2352 Zhang, X., Church, J. A., 2012. Sea level trends, interannual and decadal variability in the pacific
2353 ocean. Geophysical Research Letters 39 (21), 10.1029/2012GL053240.
2354 URL <http://dx.doi.org/10.1029/2012GL053240>